Università degli Studi di Roma
"Tor Vergata"

Facoltà di Scienze Matematiche
Fisiche e Naturali
Dipartimento di Fisica

Large mass dimuon detection in the LHCb experiment

Doctoral Thesis in Physics

Stefano de Capua

Tutor
Prof. Giovanni Carboni

Coordinator
Prof. Piergiorgio Picozza

Roma, 2005

Acknowledgements

First of all, I would like to thank Prof. Giovanni Carboni for giving me the opportunity to work in his group and to considerably improve my knowledges in the experimental physics.

Special thanks to Roberto Messi and Emanuele Santovetti for the support and all the fruitful discussions.

I would also like to thank the LHCb Muon group for the collaborative effort and in particular Vincenzo Vagnoni for the important suggestions to this thesis.

Furthermore, I would like to express my gratitude to Prof. Torbjörn Sjöstrand for his willingness to answer my many questions about PYTHIA.

Abstract

The LHCb experiment will take place at the future LHC accelerator at CERN and will start in 2007. It is a single arm spectrometer dedicated to study CP violation and rare phenomena in b hadron decays. LHCb is designed with a robust and high-performance trigger, optimised to exploit the large number of b hadrons produced at LHC. This will allow to pursue an extensive program on B-physics, overconstraining the Standard Model predictions about CP violation, and discovering any possible inconsistency ("New Physics"). The LHCb experiment has finished its R&D at the end of 2003, when the reoptimised design of the detector has been carried out. At the time of this thesis, the LHCb detector is under construction and it is expected to be complete for the first data taking in the second half of 2007. The LHCb Muon System will play a fundamental role in the experiment. Muon triggering and offline muon identification are in fact fundamental requirements of the LHCb experiment: muons are present in the final states of many CP-sensitive B decays and also in some rare B decays which may reveal new physics beyond the Standard Model. The muon detector will be equipped with 1368 multiwire proportional chamber produced in six different sites; thus, a stringent procedure for the quality control test during and after the chambers construction has been adopted. The commissioning of the Muon System is expected at the beginning of 2007.

The structure of this thesis consists of two main parts: in the first part (Detector studies), the work is focused on the performances of the Multiwire Proportional Chambers, adopted for the detection of muons in LHCb, while in the second part (Physics studies) it is focused on the study of the LHCb potentialities to improve the knowledges of the proton Parton Distribution Functions with the physical channel $Z^0 \rightarrow \mu^+\mu^-$.

The work described in the first part is concentrated on the cosmic rays test station developed in Rome2 in order to carry out the study of the detectors performances. In particular, the cosmic rays stand allows to perform a detailed study of the detector tracking capabilities and to obtain precise measurements of the efficiency and gas gain uniformity of the produced chambers.

In the second part of the thesis is reported a study of the process $pp \rightarrow \mathrm{Z}^0 \rightarrow \mu^+\mu^-$. The aim of the study is to demonstrate that, in spite of the limited angular acceptance and the optimization for a different kind of physics, the number of Z^0 detected at LHCb is sufficient to make profitable physics. Moreover, the foward design of the spectrometer allows to study the proton structure in a kinematic region not probed by the present experiments. A particular focus has been put on the effect of the LHCb geometrical acceptance on the cross section sensitivity to the various set of partons, simulating the process with two event generators, PYTHIA and MC@NLO.

Contents

Part I

Detector studies

Chapter 1

The LHCb experiment at LHC

1.1 The Large Hadron Collider

The Large Hadron Collider (LHC) is a 27 km circumference high luminosity proton-proton collider with a center-of-mass energy of $\sqrt{s}=14$ TeV.

The LHC is being built in the existing LEP tunnel, buried around 50 to 150 m underground. Two counter rotating proton beams are accelerated in a linear accelerator (Linac) up to 50 MeV and then injected in two circular accelerators where they are boosted to 1 GeV (Booster) and 26 GeV (PS). Then the beams enter the Super Proton Synchrotron (SPS) where they reach the energy of 450 GeV and finally, via two new tunnels, they are injected in the LHC and accelerated up to 7 TeV (see Figure 1.1).

The beam moves around the LHC ring inside a continuous vacuum chambers which pass through a large number of magnets: 1232 superconducting dipole magnets (8.34 T) bend the high momentum beam around the 27 km ring. A huge cryogenics system is required to produce the liquid helium at the temperature of 1.9 °K, needed to keep the magnets cold. The beams will be stored at high energy for 10 to 20 hours. In 10 hours the particles will make about four hundred million revolutions around the machine, producing several collisions inside the five LHC experiments.

The four main experiments at the LHC are located at each of the four interaction points, where the beams cross over to the other beam pipe and collide under a small angle. Two consecutive bunch crossings are separated in time by 25 ns, which sets the basic clock frequency for the detector electronics to 40 MHz. The machine luminosity is a fundamental parameter for the collider performance because it determines the number of pp collisions at each crossing point. It includes the compactness of the beams, the magnets cability to focus the beams at the interaction point, the number of particles in the bunches and the bunch crossings rate (see Ref. [1]).

Figure 1.1 also shows the location of the four experiments along the LHC ring.

The ATLAS [2] and CMS [3] experiments are located in new caverns built at

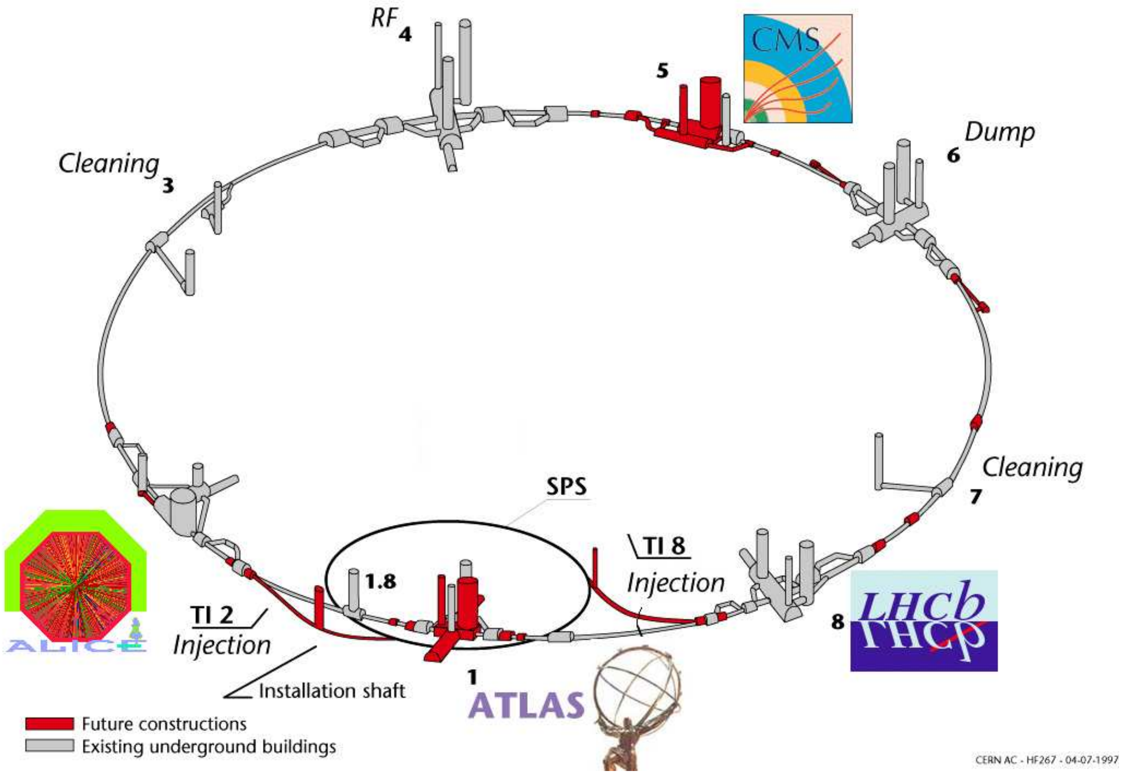

Figure 1.1: The LHC complex.

the interaction points IP1 and IP5 and are general-purpose central detectors. Their main physics goals are the search for the Higgs boson and for SUSY particles.

In the same interaction point of CMS, the TOTEM [4] experiment will be installed: its main goal will be to study very forward QCD processes and to measure the total cross section at LHC, which is very important for the other experiments (*e.g.* for absolute luminosity measurements).

The ALICE [5] experiment, located at IP2, will focus on studying the quark-gluon plasma in dedicated runs for heavy ions collisions (Pb-Pb, Ca-Ca).

Finally the LHCb [6] experiment at IP8 is dedicated to b-quark physics and will be described in detail in Section 1.2.

The relevant cross sections at LHC are given in Table 1.1. The inelastic cross section σ_{inel} is extrapolated basing on UA1, CDF and D∅ data [7], but with large uncertainties. The total inelastic cross section defines the average number of interactions per bunch crossing:

$$N_{pp} = \frac{\mathcal{L}\sigma_{inel}}{f_{bx}}$$

where f_{bx} is the bunch crossing frequency (40 MHz).

Table 1.1: cross sections at LHC

Total	σ_{tot}	100 mb
Inelastic	σ_{inel}	55 mb
$c\bar{c}$	$\sigma_{c\bar{c}}$	3.5 mb
$b\bar{b}$	$\sigma_{b\bar{b}}$	500 μb

Because of the displaced interaction point of LHCb (see Section 1.2), only the 74.3% of bunches will collide [1]. The average bunch crossing rate, therefore, will be 30 MHz. Figure 1.2 show the probabilities to have n=0,..,4 pp interactions per bunch crossing as a function of the machine luminosity, where the inelastic pp cross section is assumed to be 80 mb. Compared to events with one pp interaction, those with multiple pp interactions are more difficult to reconstruct due to the increased particle density. Therefore, the rejection of pile-up events is essential in order to maximize the number of triggered $b\bar{b}$ events. Other important factors influencing the choice of the running luminosity are the radiation damage that may result, and the occupancy of the detectors.

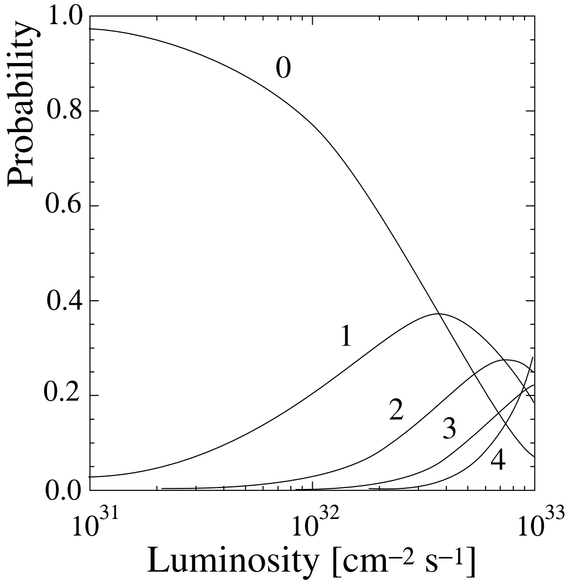

Figure 1.2: Probability for n inelastic collisions per bunch crossing as a function of luminosity.

Taking all these points into account, the average running luminosity of the LHCb experiment has been chosen to be $\mathcal{L} = 2 \times 10^{32}$ cm^{-2} s^{-1}. At this luminosity there are interactions in 30% of the bunch crossings and the effective bunch crossing rate, with only one pp interaction, is thus about 10 MHz.

The cross section $\sigma_{b\bar{b}}$ will be between 175 and 950 μb [8] depending on the value of badly known parameters. The value of 500 μb is a mean assumed as a reference by all LHC experiments. It will be known more precisely after the start of LHC. The dominant $b\bar{b}$ production mechanism in pp collisions is the fusion of two or more gluons radiated from the constituent quarks of the protons. This leads to an approximately flat distribution in rapidity and hence an angular distribution peaked at low polar angles. The directions of the two b hadrons are very correlated, as shown in Figure 1.3. The two peaks correspond to $b\bar{b}$ pairs flying in either directions of the beam axis. Consequently a dedicated b-physics experiment should cover low polar angles.

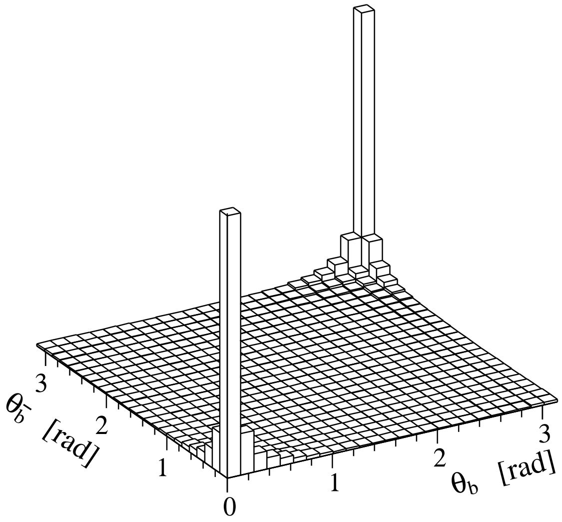

Figure 1.3: Polar angle θ of b and $\bar{b}$ hadron directions.

1.2 The LHCb detector

The LHCb detector [6] is a single-arm forward spectrometer dedicated to the study of CP violation and other rare phenomena in the decays of Beauty particles. It is housed in the underground pit located at one of the interaction points (IP8) along the LHC ring. The experimental setup is shown in Fig.1.4.

To accomodate the spectrometer in the present cavern, without the need for substantial civil engineering work, the beam crossing point has been displaced from the center of the cavern by about 11 m, constraining the total length of the detector to 20 m; the overall dimensions are about $6{\times}5{\times}20$ m^3. Thus, the acceptance of the detector, defined by the aperture of the magnet, is 300 mrad in the horizontal plane (i.e., the bending plane of the magnet), and 250 mrad in the vertical plane (non-bending plane).

A right-handed coordinate system is defined centred on the interaction point, with z along the beam axis and y pointing upwards.

The detector design has gone through a number of optimisation phases. These changes are referred to as the *reoptimisation* [9]. Figure 1.4 shows the reoptimised design of the LHCb detector geometry; one can see, from left to right:

- the vertex locator (VELO)
- the upstream Ring-Imaging Cherenkov detector (RICH1)
- the trigger tracking (TT)
- the magnet
- the tracking system (T1,T2,T3)
- the downstream Ring-Imaging Cherenkov detector (RICH2)
- the preshower (SPD/PS)
- the electromagnetic calorimeter (ECAL)
- the hadronic calorimeter (HCAL)
- the muon system

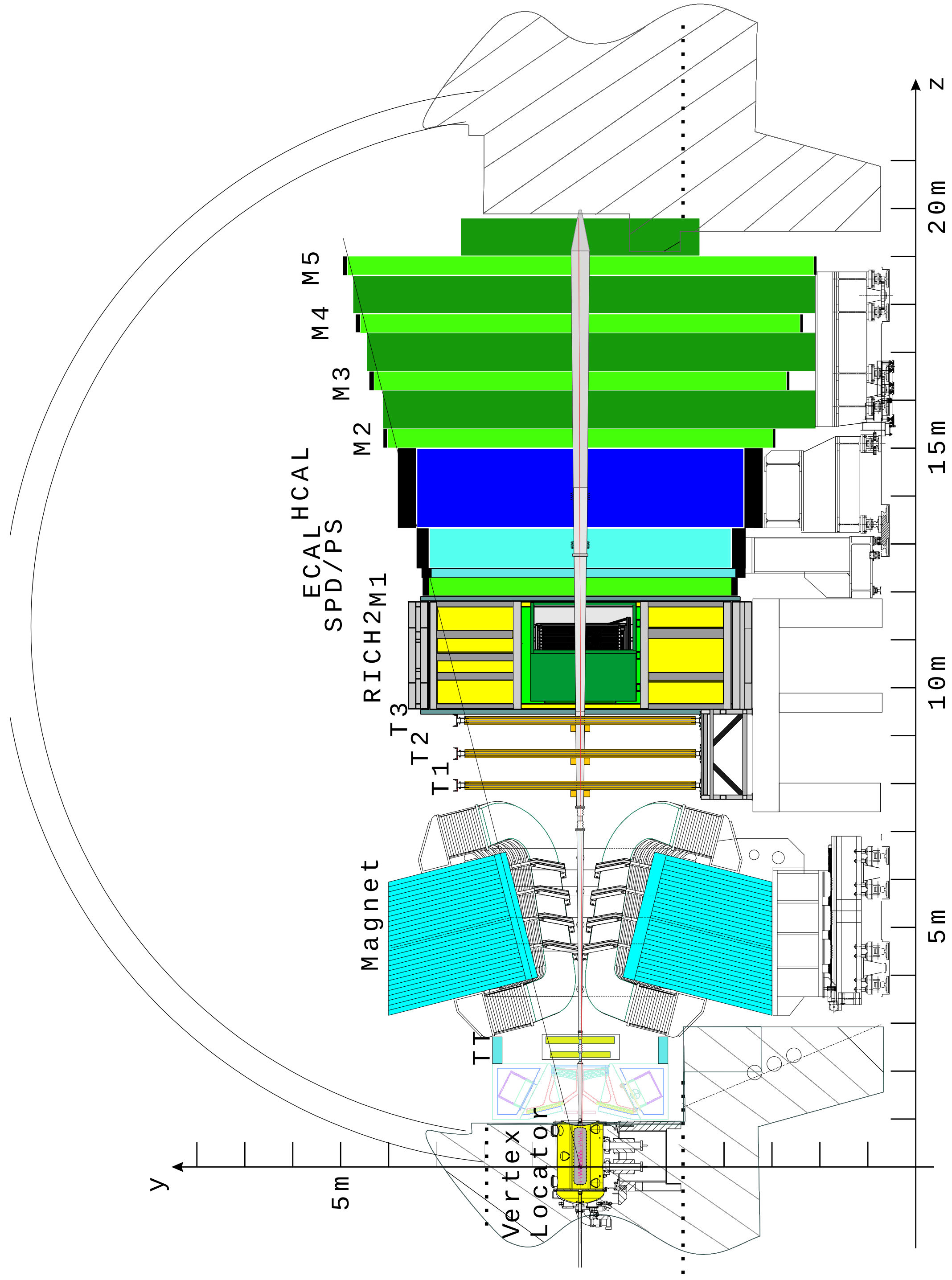

Figure 1.4: The LHCb spectrometer seen from above (cut in the bending plane).

1.2.1 The Vertex Locator (VELO)

Vertex reconstruction is a fundamental requirement for the LHCb experiment. Displaced secondary vertices are a distinctive feature of b-hadron decays. The **VE**rtex **LO**cator (VELO) [10] has to provide precise measurements of track coordinates close to the interaction region. These are used to reconstruct production and decay vertices of beauty and charm-hadrons, to provide an accurate measurement of their decay lifetimes, and to measure the impact parameter of particles used to tag their flavor. The VELO measurements are also a vital input to the second level trigger (L1), which enriches the b-decay content of the data.

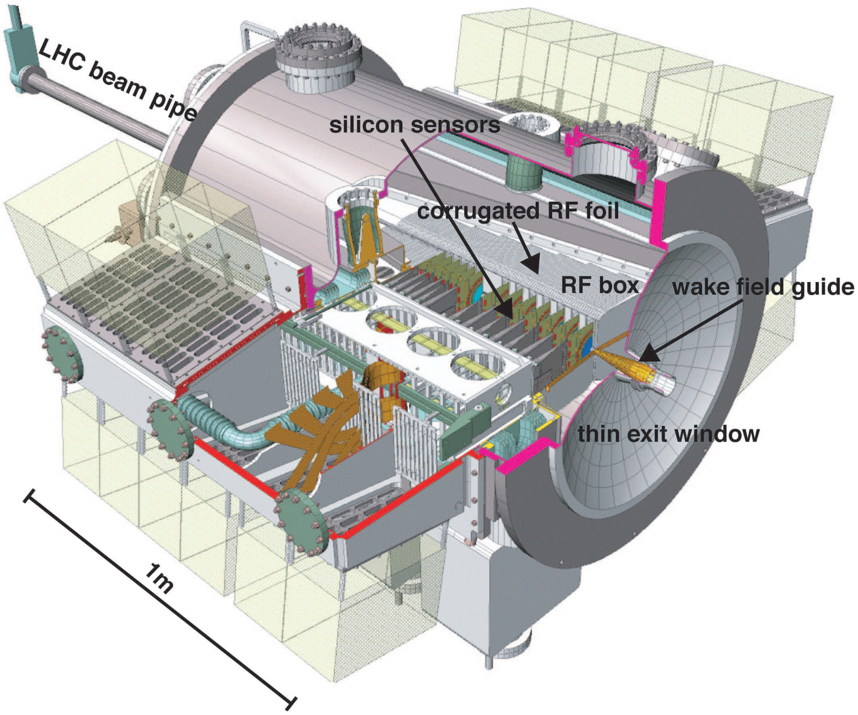

Figure 1.5: A cross section of the VELO tank.

The VELO features a series (25) of disk-shaped silicon stations placed along the beam direction, with a $r-\phi$ segmentation geometry.

The position resolution of the primary vertex is dominated by the number of tracks produced in a pp collision. For an average event, the resolution in the z-direction is 42 μm and 10 μm perpendicular to the beam (xy-direction). For secondary vertices, it varies from 150 and 300 μm, and this corresponds to less than 50 fs resolution on the B proper time of flight.

1.2.2 The Beam Pipe

After the exit wall of the VELO, the LHC beam is protected by a beam pipe [6] made of two conical sections. The first section is 1.3 m long with a 25 mrad opening angle, while the second one is 16 m long with a 10 mrad opening angle.

The beam pipe is designed to minimise the creation of secondary particles, while resisting the air pressure from outside. The first part of the beam pipe is made out of the light-weighted materials beryllium (1.8 m long) and beryllium-aluminium alloy (10 m long). After z = 13 m, where the amount of material is not critical anymore, the beam pipe is constructed from stainless steel. The minimal radius is 2.5 cm (limited by LHC injection requirements) and the final radius of the second section is 13 cm.

1.2.3 The RICH

Particle identification is a fundamental requirement of the LHCb experiment. The ability to distinguish between pions and kaons in a variety of final states is essential for the physics that the experiment is designed to study: meaningful CP-violation measurements are only possible in many important channels if hadron identification is available. The particle identification is achieved using two Ring-Imaging Cherenkov (RICH) [11] detectors.

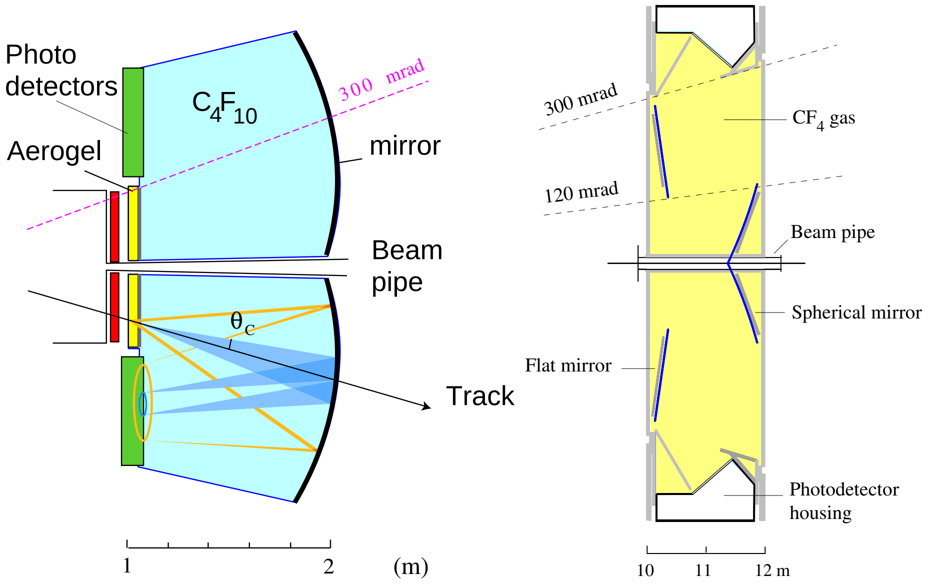

Figure 1.6: A schematic view of the RICH1 (on the left) and RICH2 (on the right).

An example of the importance of the RICH system is the measurement of the CP asymmetry of $B_d^0 \to \pi^+\pi^-$ decays. This requires the rejection of two-body backgrounds with the same topology: $B_d^0 \to K^+\pi^-$, $B_s^0 \to K^-\pi^+$ and $B_s^0 \to K^+K^-$.

Identifying kaons from the accompanying b hadron decay in the event also provides a valuable flavour tag, and ensures that all events accepted by the LHCb trigger are potentially useful in the CP violation measurements. The flavour tag is achieved by identifying kaons from the $b \to c \to s$ cascade decay, where the charge of the kaon depends on the charge of the initial b quark.

The RICH detects ring images formed by Cherenkov photons around the track of the particle traversing various radiators. To cover the full momentum range (1-

150 GeV), three different radiators are required, with different refractive indices: silica aerogel, C_4F_{10} and CF_4. The photons are detected by cylindrical pixelated Hybrid photodiode (HPD) tubes. These detectors are sensitive to magnetic fields, which imposes that RICH is located outside of the bending area. Moreover, there is a strong correlation of the momentum and the polar angle of the track ($\theta \simeq 1/P$). Therefore, the RICH system is divided in two sectors:

- the upstream RICH (RICH1), located before the magnet, uses silica aerogel (refractive index n=1.03) and C_4F_{10} (n=1.0014) as radiators. It is designed for low momentum (1-70 GeV) and high angle (30-300 mrad) tracks. The light is reflected by spherical mirrors onto the photo-detector.

- the downstream RICH (RICH2), located after the magnet, uses CF_4 (n=1.0005) as radiator. It covers high momentum (12-150 GeV) and low angle tracks (15-120 mrad).

1.2.4 The Trigger Tracker

The Trigger Tracker (TT) [9] is located downstream of RICH1 and just in front of the magnet. It consists of two stations separated by a distance of 27 cm. As the name indicates, data from the TT is used to make the trigger decision. The presence of a low integrated magnetic field of 0.15 Tm between the VELO and the TT is sufficient to assign a rough momentum estimate with a resolution of 20%-40% to the tracks.

Apart from its use in the trigger, the TT also serves to reconstruct long-living neutral particles which may decay outside the acceptance of the VELO. Furthermore, it provides a momentum estimate for slow particles that are bent out of the LHCb acceptance before reaching the T stations, and it improves the momentum estimate for particles that do reach the T stations.

The active area of the trigger tracker is entirely covered by silicon microstrip detectors with a strip pitch of 198 μm and strip lengths of up to 33 cm.

1.2.5 The Magnet

The spectrometer dipole [12] is placed close to the interaction region, in order to keep its size small, and after the iron shielding wall which protect the VELO and RICH1 from the magnetic field. The field is oriented vertically which makes the tracks to bend in the horizontal $x - z$ plane. The bending power of the magnet is represented by the total integrated field, which is $\int Bdl$= 4 Tm.

The free aperture is 4.3 m horizontally and 3.6 m vertically. The magnet is made of 50 tons of aluminum conducting wires (9 km in total) and of a 120 kt steel plate yoke. It dissipates 4.2 MW. The polarity of the field can be changed to reduce systematic errors in the CP-violation measurements that could result from a possible left-right asymmetries in the detector. This requirement and a detailed cost analysis have lead to the choice of a warm magnet rather than a superconducting magnet.

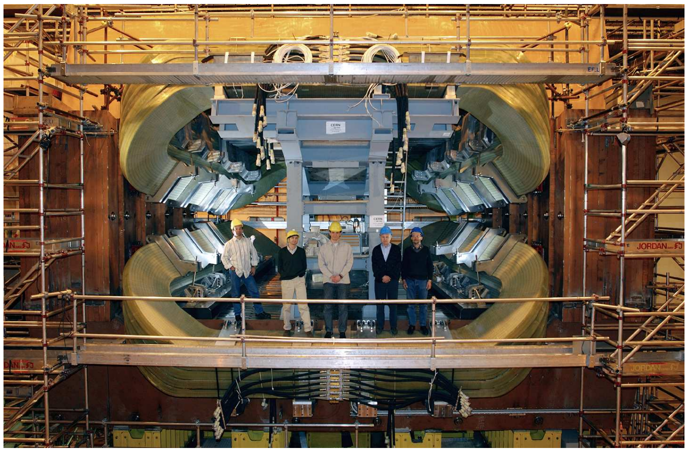

Figure 1.7: The LHCb magnet.

1.2.6 The Tracking System

The principal task of the tracking system [13, 14] is to provide efficient reconstruction of charged particle tracks and precise measurements of their momenta: for example, a mass resolution of 10 MeV in the decay $B_s \to D_s K$ translates into a requirement on momentum resolution of $\delta p/p$=0.4%. It also provides a link between the measurements in the vertex locator and the measurements in the calorimeter and muon system.

The tracker consists of three stations perpendicular to the beam axis. Each tracking station measures the bending plane coordinate (x) and 2 *stereo* coordinates at $x \pm 5$, to have also some information about y and to resolve ambiguities. As the track density at fixed z approximately follows $1/r^2$, the tracking system is segmented in an inner tracker located close to the beam pipe and an outer tracker covering the remaining 98% of te area.

The Inner Tracker

The Inner Tracker (IT) covers the innermost region of the T1...T3 stations, which receives the highest flux of charged particles. It consists of four cross-shaped station equipped with silicon sensors, placed around the beam. The silicon foils are 300 μm thick and have a 230 μm strip pitch, resulting in a resolution of approximately 70 μm. The same readout scheme as for the VELO is foreseen, except for the interface to the Level-1 trigger which is not needed by the IT.

The Outer Tracker

In the T stations, the Outer Tracker (OT) covers the large region outside the acceptance of the Inner Tracker. Charged particles are detected in the OT with gas-filled straw tubes serving as drift cells. These have a 5 mm diameter and 75 μm thick walls. To reach an average resolution on the momentum of $\delta p/p$=0.4% the tracking precision has to be optimal in the $x-z$ magnet bending plane. Therefore most stations have two planes with wires in the vertical direction and two stereo planes with wires in the horizontal direction.

The choice of the drift gas is driven by the requirement that it should provide a fast signal collection: the constraint is collect the signal within the time of two LHC bunch crossings. The selected drift gas is the mixture Ar(75)/CF_4(15)/CO_2(10), which has a maximum drift time of 32.5 ns. Including a propagation time of the electrical signal of about 10 ns, this results in a total signal collection time slightly below 50 ns, that is the delay between two LHC bunch crossings. Thus, it can happen that two events are piled-up in the outer tracker.

1.2.7 The Calorimeter System

The main purpose of the LHCb calorimeter system [15] is to identify electrons and hadrons and to provide measurements of their energy and position, which are used as input to the Level-0 trigger. Thus the detector structure is a compromise between a small number of readout channels and a low occupancy with a reasonable energy and position resolution. Fast binary readout has been chosen to cope with the Level-0 trigger requirements. As for the VELO, the design is motivated by fast triggering requirements.

The structure chosen consists of three elements: a single-layer Preshower (SPD-PS) detector followed by a Shashlik electromagnetic calorimeter (ECAL) and a scintillating tile hadron calorimeter (HCAL).

The Electromagnetic Calorimeter and the Preshower

The ECAL detectes electrons and photons via the electromagnetic showers of e^+e^- pairs and photons. Its total radiation length is $25X_0$. In addition, two separate detection layers are located in front of the ECAL: a scintillator pad detector (SPD) and a preshower detector (PS). The SPD and PS provide valuable information by the different shapes of the electromagnetic showers induced in the ECAL. Both the SPD and the PS detectors consist of 15mm thick scintillator pads, and they are separated by 12 mm of lead.

The electromagnetic calorimeter employs the Shashlik technology of a sampling scintillator/lead structure read out by plastic WLS fibres. It is segmented in three resolution zones in order to optimize the π^0 reconstruction. The energy resolution is:

$$\frac{\sigma(E)}{E} = \frac{10\%}{\sqrt{E}} \oplus 1.5\%$$

where E is expressed in GeV and $\oplus$ means addition in quadrature.

The Hadronic Calorimeter

The hadronic calorimeter (HCAL) identifes hadrons via inelastic interactions with the detector material. The products of the interaction are mainly π, which are detected in the scintillator. The HCAL is made of 16 mm thick iron and 4 mm thick scintillating tiles, parallel to the beam. The light is collected at the end of the tile by wavelength shifting fibers (WLS). The energy resolution is:

$$\frac{\sigma(E)}{E} = \frac{80\%}{\sqrt{E}} \oplus 10\%$$

where again E is expressed in GeV and $\oplus$ means addition in quadrature.

1.2.8 The Muon System

The muon detector [16] consists of a muon shield (composed of the ECAL, the HCAL and three layers of iron) and of 5 stations (M1...M5). The first station is placed in front of the calorimeters and is important for the transverse momentum measurements of the muon track, while the remaining four stations are placed behind the calorimeters and interleaved with the muon shield. The muon detector is used both in the Level-0 trigger to select muons with a high transverse momentum (high p_{T} muons are mainly produced in B decays) and in the muon identification which is a basic ingredient of the search for rare semileptonic decays. More detail about the Muon System will be given in Chapter 2.

1.3 The LHCb Trigger

The trigger system [17] is one of the biggest challenges of the LHCb experiment. It is designed to distinguish inelastic pp interactions (called minimum-bias events) from events containing B mesons through the presence of particles with a large transverse momentum (p_{T}) and the existence of secondary vertices.

At the LHCb luminosity ($\mathcal{L} = 2 \times 10^{32}$ cm^{-2} s^{-1}), an inelastic pp interaction happens at an average rate of 16 MHz. The ratio of the $b\bar{b}$ and minimum-bias cross section is $\sigma_{b\bar{b}}/\sigma_{inel} \simeq$0.01, and the $b\bar{b}$ production rate is therefore about 150 kHz. However, in only about 15% of the events will at least one B meson have all its decay products contained in the acceptance of the spectrometer. Furthermore, the branching ratios of B mesons used to study CP violation are typically less than 10^{-3}. These considerations leads to expect about 10^6 background events every B event of interest.

The offline selections exploit the relatively large b mass and lifetime to select those b-hadrons, and stringent cuts have to be applied to enhance signal over background and thus increase the CP sensitivity of the analysis. Hence the requirement for the trigger is to achieve the highest efficiency for these offline selected events and to be able to achieve high efficiency for a large variety of final states.

This reduction is achieved in three trigger levels: Level-0 (L0), Level-1 (L1) and the High Level Trigger (HLT). These levels are described below and summarized in Table 1.3.

Table 1.2: Summary of the trigger scheme.

Level	Selects	Input rate	Reduction	Latency
Pile-up system	Single events	13 MHz	1.3	
Level-0	High p_{T} tracks	10 MHz	10	4 μs
Level-1	Secondary vertices	1 MHz	25	$\approx$ 1.6 ms
HLT	Reconstructed B events	40 kHz	200	
Events are written on tape		200 Hz		

1.3.1 The Level-0 trigger

Due to their large mass, b-hadrons decay to give a large E_{T} lepton, hadron or photon, hence Level-0 reconstructs:

- the highest E_{T} hadron, electron and photon clusters in the Calorimeter.
- the two highest p_{T} muons in the Muon Chambers.

which information is collected by the Level-0 Decision Unit to select events.

Events can be rejected based on global event variables such as charged track multiplicities and the number of interactions, as reconstructed by the Pile-Up system, to assure that the selection is based on b-signatures rather than large combinatorics, and that these events will not occupy a disproportional fraction of the data-flow bandwidth or available processing power in subsequent trigger levels.

The Level-0 trigger is fully synchronous, i.e. its latency does not depend upon occupancy and it has a fixed latency of 4μs. Its electronics is implemented in full custom board. The rate at the L0 output is reduced to 1 MHz. Efficiencies of approximately 90%, 70% and 50% are achieved for events with muons, hadrons and photons respectively.

The relative weight of each trigger can be tuned by changing the single cuts, depending on the type of physics one wants to favor. The optimization of the cuts for the precise measurements of CP-violating parameters leads to a bandwidth of 60% for the hadron trigger, 10% for the electron trigger, 10% for the photon trigger and 20% for the muon trigger.

1.3.2 The Level-1 trigger

At the 1 MHz output rate of Level-0 the remaining analogue data is digitized and all data is stored for the time needed to process the Level-1 algorithm. The L1 algorithm will be implemented on a commodity processors farm, which is shared between Level-1, HLT and offline reconstruction algorithms. The available time at L1 is on average $\sim$ 1 ms, with a maximum latency of 52.4 ms given by the L1 buffer size.

The Level-1 algorithm uses the information from Level-0, the VELO and TT stations. The algorithm reconstructs tracks in the VELO, and matches these tracks to Level-0 muons or Calorimeter clusters to identify them and measure their momenta. The fringe field of the magnet between the VELO and TT is used to determine the momenta of particles with a resolution of 20-40%. Events are selected based on tracks with a large p_T and significant impact parameter to the primary vertex. Using two high impact parameter tracks with the highest p_T , efficiencies between 50% and 70% are achieved.

1.3.3 The High Level Trigger

The HLT and Level-0 algorithms run concurrently on the same CPU nodes, with the L1 taking priority due to its limited latency budget. The HLT algorithm starts with reconstructing the VELO tracks and the primary vertex, rather than having this information transmitted from Level-1. A fast pattern recognition program links the VELO tracks to the tracking stations T1-T3. The final selection of interesting events is a combination of confirming the L1 decision with better resolution, and selection cuts dedicated to specific final states. While the maximum output rates of the first two trigger levels are dictated by the implementations of the FE hardware, the output rate of the HLT is kept more flexible.

Considering the channels currently under study one could envisage output rates of a few Hz. However, the RICH information is not currently used by the HLT, and selection cuts have to be relaxed compared to the final selection to study the sensitivity of the selections and profit from refinements to the calibration constants. These considerations lead to an output rate of 200 Hz of events accepted by the HLT.

1.4 The LHCb simulation software

The software programs used for the performance studies of the LHCb experiment execute the following tasks:

- generation of the event.
- tracking of particles through the detector.
- simulation of the detector response.
- simulation of the trigger decision.
- reconstruction of the event, including track finding and particle identification.
- offline selection of specific B meson final states.

The software applications of LHCb are based on an object oriented (OO) C++ framework called Gaudi [18]. The simulation package GAUSS [19] is based on GEANT 4 [20] for the detector description and on PYTHIA [21] and QQ [22] for the physics event generation. The package BOOLE [23] is used for the digitization of the event, BRUNEL [24] for the reconstruction, and finally the package DAVINCI [25] is used for the analysis.

1.5 The LHCb physics performance

Compared to other accelerators that are in operation, the LHC will be by far the most copious source of B mesons, due to the high $b\bar{b}$ cross section and high luminosity. The LHCb detector is designed to exploit the large number of b-hadrons produced at the LHC in order to make precision studies of CP asymmetries and of rare decays in the B-meson systems. For example, the current B-factories $(\mathrm{e}^+\mathrm{e}^-)$ have measured CP violation in the B-system with very high accuracy [26, 27], sin2$\beta = 0.731 \pm 0.055$, and in excellent agreement with the indirect measurement of $|V_{ub}|/|V_{cb}|$ and Δm_d from semi-leptonic B^0-decays and B^0-$\bar{\mathrm{B}}^0$ oscillations [28], sin2$\beta = 0.695 \pm 0.055$; after one year of nominal operation of LHC, the data sample collected by LHCb will be sufficient to determine β with similar accuracy.

Another important purpose of the LHCb experiment is the direct measurement of γ: the Standard Model analysis predicts a value of the CKM angle γ=$64.5^{\mathrm{o}} \pm 7^{\mathrm{o}}$; in one year of data taking we expect to achieve a precision of 0.07-0.31. Expected precision on the angles of the unitarity triangles obtained by the LHCb experiment in one year of data taking are summarised in Table 1.3, together with the sensitivity to the B^0_s-$\overline{\mathrm{B}}^0_\mathrm{s}$ oscillations (x_s).

Table 1.3: Expected precision on the angles of the unitarity triangles obtained by the LHCb experiment in one year of data taking.

Parameter	Decay Mode	σ [1 year]
$\beta + \gamma$ $(= \pi - \alpha)$	B^0_d and $\overline{\mathrm{B}}^0_\mathrm{d} \to \pi^+\pi^-$; no penguin with penguin/tree= 0.20 ± 0.02	0.03 0.03–0.16
β	B^0_d and $\overline{\mathrm{B}}^0_\mathrm{d} \to \mathrm{J}/\psi \mathrm{K_S}$	0.01
$\gamma - 2\delta\gamma$	B^0_s and $\overline{\mathrm{B}}^0_\mathrm{s} \to \mathrm{D}^\pm_\mathrm{s}\mathrm{K}^\mp$	0.05–0.28
γ	$\mathrm{B}^0_\mathrm{d} \to \overline{\mathrm{D}}{}^0\mathrm{K}^{*0}, \mathrm{D}^0\mathrm{K}^{*0}, \mathrm{D}_1\mathrm{K}^{*0}$ and $\overline{\mathrm{B}}^0_\mathrm{d} \to \overline{\mathrm{D}}{}^0\overline{\mathrm{K}}{}^{*0}, \mathrm{D}^0\overline{\mathrm{K}}{}^{*0}, \mathrm{D}_1\overline{\mathrm{K}}{}^{*0}$	0.07–0.31
$\delta\gamma$	B^0_s and $\overline{\mathrm{B}}^0_\mathrm{s} \to \mathrm{J}/\psi\phi$	0.01
x_s	B^0_s and $\overline{\mathrm{B}}^0_\mathrm{s} \to \mathrm{D}^\pm_\mathrm{s}\pi^\mp$	up to 90 (95% CL)

In addition to investigating CP violation in B-meson decays, the physics programme of the LHCb experiment will include studies of rare B (such as $\mathrm{B}^0 \to \mathrm{K}^{*0}\gamma$, or the experimentally very clean decays containing muons, $\mathrm{B}^0 \to \mu^+\mu^-\mathrm{K}^{*0}$, $\mathrm{B}^0_\mathrm{s} \to \mu^+\mu^-$ and $\mathrm{B}^0 \to \mu^+\mu^-$), D-$\overline{\mathrm{D}}$ oscillations and $\mathrm{B_c}$-meson decays.

Chapter 2

The Muon System

2.1 Introduction

Muon triggering and off-line muon identification are fundamental requirements of the LHCb experiment. Muons are present in the final states of many CP sensitive B decays, in particular the two *gold-plated* decays,

$$\begin{array}{rcl} B_d^0 & \to & J/\psi(\mu^+\mu^-)K_S^0 \\ B_s^0 & \to & J/\psi(\mu^+\mu^-)\phi \end{array}$$

In many CP violation and flavour oscillations studies at LHCb, the $\mathcal{A}_{\mathrm{CP}}$ asymmetry between the numbers of B^0 and $\bar{\mathrm{B}}^0$ decaying to a final state f has to be measured:

$$\mathcal{A}_{\mathrm{CP}}(t) = \frac{N_{\bar{\mathrm{B}}^0 \to f}(t) - N_{\mathrm{B}^0 \to f}(t)}{N_{\bar{\mathrm{B}}^0 \to f}(t) + N_{\mathrm{B}^0 \to f}(t)}$$

This implies that the identification of the initial flavour of reconstructed B_d^0 and B_s^0 mesons (flavour tagging) is necessary in order to study decays involving CP asymmetries and flavour oscillations as well. The statistical uncertainty on the measured CP asymmetries is directly related to the effective efficiency ϵ_{eff}, which is defined as:

$$\epsilon_{\mathrm{eff}} = \epsilon_{\mathrm{tag}} \left(1 - 2w\right)^2$$

where ϵ_{tag} is the tagging efficiency and w is the wrong tag fraction. The tagging performances for the channel $\mathrm{B}_d^0 \to \mathrm{J}/\psi(\mu\mu)\mathrm{K}_s^0$ are reported in table 2.1 for each tag indipendently, as well as for the combined tagging decision.

Table 2.1: Tagging performances for $B_d^0 \rightarrow J/\psi(\mu\mu)K_s^0$ signal events. Uncertainties are statistical.

Tag	ϵ_{tag} (%)	w (%)	ϵ_{eff} (%)
Muons	7.92±0.32	36.1±2.0	0.61±0.18
Electrons	3.33±0.22	37.1±3.2	0.22±0.11
Opp. side kaons	24.34±0.51	35.1±1.2	2.15±0.34
Same side π/K	28.26±0.54	43.9±1.1	0.42±0.15
Vertex charge	22.38±0.50	41.5±1.2	0.64±0.19
Combined	58.18±0.59	36.95±0.77	3.96±0.64

In addition, the study of rare B decays such as the Flavor Changing Neutral Current decay,

$$B_s^0 \rightarrow \mu^+\mu^-$$

may reveal new physics beyond the Standard Model.

2.2 Physics requirements

The main requirement for the muon detector is to provide a high p_{T} muon trigger at the earliest trigger level (Level-0). The effective LHCb Level-0 input rate, at $\mathcal{L} = 2 \times 10^{32}$ cm^{-2} s^{-1}, is about 15 MHz on average assuming a non-diffractive pp interaction cross-section of 55 mb. This input rate must be reduced to 1 MHz within a latency of 4.0 μs , while retaining good efficiency for events containing interesting B decays. The muon trigger provides between 10% and 30% of this trigger rate. In addition, the muon trigger must unambiguously identify the parent bunch crossing, requiring a time resolution better than 25 ns.

The muon detector consists of five muon tracking stations placed along the beam axis and interspersed with a shield to attenuate hadrons, electrons and photons. The muon trigger is based on a stand-alone muon track reconstruction and p_{T} measurement with a resolution of about 20%. To trigger, a muon must hit all five muon stations, giving a lower momentum threshold for efficient muon triggering of about 5 GeV/c. Hits in the first two stations are used to calculate the p_{T} of the candidate muon.

Since the polar angle and the momentum of the particles are correlated, high momentum tracks tend to be closer to the beam axis. Multiple scattering in the absorber therefore increases with the distance from the beam axis, limiting the spatial resolution of the detector. The granularity of the detector varies such that its contribution to the p_{T} resolution is approximately equal to the multiple-scattering contribution. The various contributions to the p_{T} resolution for muons from semileptonic b decay are shown in Figure 2.1.

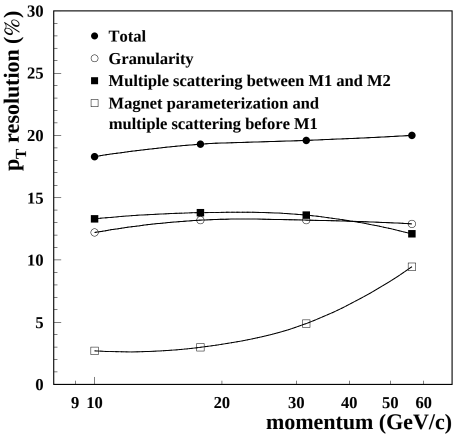

Figure 2.1: Contributions to the transverse momentum resolution of the muon system as a function of the muon momentum averaged over the full acceptance.

The muon system must also provide off-line muon identification. Muons reconstructed in the high precision tracking detectors with momenta down to 3 GeV/c must be correctly identified with an efficiency of about 95% while keeping the hadron misidentification rate below 1%. Efficient muon identification with low contamination is required both for tagging and the clean reconstruction of muonic final state B decays.

The high particle fluxes expected in the Muon System impose stringent requirements on the detector. These requirements include the rate capability of the chambers, the ageing characteristics and the redundancy of the trigger instrumentation. Spurious hits could also affect the muon transverse momentum resolution due to incorrect hit association. The main background to the $\mathrm{B} \rightarrow \mu\mathrm{X}$ detection is formed by muons decaying from the large number of π/K mesons produced in the pp collisions and therefore a p_{T} cut of 1 GeV/c will be used. Also relevant are the electromagnetic showers generated by photons from π^0 decays, the low-energy neutrons produced in hadronic cascades in the calorimeters and the beam halo muons.

Background caused by real muons traversing the detector is well simulated with the available Monte Carlo packages [29, 30]. An estimate for the rate in the various regions of the muon system has been obtained from a detailed study [31, 32, 33]. The nominal rates are calculated for a luminosity of $\mathcal{L} = 5 \times 10^{32}$ cm^{-2} s^{-1}, at which the LHCb experiment should be able to operate for short periods. The maximal rates are then obtained applying a safety factor of 5 in the stations M2-M5 and a safety factor of 2 in the station M1, which is positioned in front of the calorimeters and therefore is less affected by the uncertainties in the showering processes in the absorber material. The rate rises from a few hundred Hz/cm^2 in the outer regions of stations M4 and M5 to a few hundred kHz/cm^2 in the innermost part of station M1.

The combination of physics goals and background conditions determines the choice of detector technologies for the various stations and regions. The following parameters are particularly relevant:

1. *Rate capability:* the selected technologies must provide single layer efficiencies of more than 95% at the expected rates.

2. *Ageing:* the detectors should have good ageing properties, allowing 10 years of operations. The detector should tolerate the total integrated charge accumulated in that period.

3. *Time resolution:* the muon system must provide unambiguous bunch crossing identification with high efficiency. The requirement is at least 95% efficiency within a 20 ns window for each of the two layers in the station.

4. *Spatial resolution:* the spatial resolution must allow the determination of the p_{T} of triggering muons with a resolution of 20%, considering the multiple scattering effect already mentioned. This requires a granularity varying from few mm in the innermost region of stations M1 and M2, to few tens of cm in station M5. To minimize the deterioration of the intrinsic detector resolution, cross talk between readout channels should be limited below 10%.

Based on the above considerations, two different detector technologies have been adopted to cover the 435 m^2 of the Muon System, which will be described in details in the next section.

2.3 Detector layout

A side view of the Muon System in the $y - z$ plane can be seen in Figure 2.2.

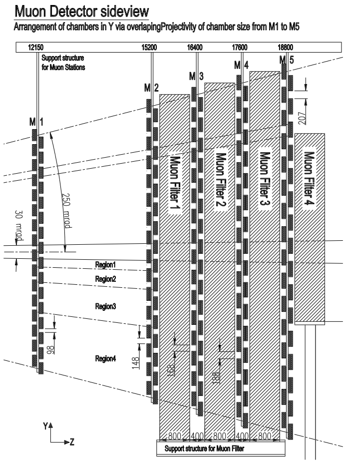

Figure 2.2: Side view of the muon system in the y-z plane.

The first station (M1) is placed in front of the calorimeter preshower, at 12.1 m from the interaction point; since it is important for the transverse-momentum measurement of the muon candidate track used in the Level-0 muon trigger, it has been placed in front of the calorimeters in order to reduce the multiple scattering. The remaining four stations are interleaved within the muon shield at mean positions of 15.3 m (M2), 16.5 m (M3), 17.6 m (M4) and 18.9 m (M5). The shield consists of the electromagnetic and hadronic calorimeters and three iron filters. The total weight of the muon shield is about 2100 tons and it has a total absorption-length of 20 nuclear interaction-lengths (see Figure 2.3).

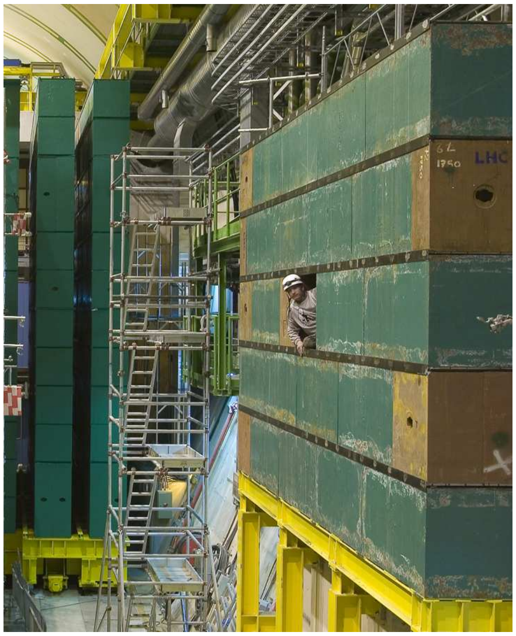

Figure 2.3: The last Muon iron shield.

The chambers within the filter are allocated about 40 cm of space along z and are separated by three shields of 80 cm thickness. The inner and outer angular acceptances of the muon system are 20 (16) mrad and 306 (258) mrad in the bending (non-bending) plane, similar to that of the tracking system. This provides a geometrical acceptance of about 20% for muons from b decays relative to the full solid angle [34]. The total detector area is about 435 m^2 .

Multiwire Proportional Chambers (MWPC), which represent a well known and robust technology, have been adopted as the baseline detector, in all the regions where the expected particles rates are between 1 kHz/cm^2 and 200 kHz/cm^2 . In the innermost region of the first muon station, mostly due to the need of a 10 years radiation hardness detector, the Gas Electron Multiplier (GEM) detector [35] has been adopted [36].

Because of the projectivity of the LHCb detector to the interaction point, the MWPC dimensions depend on the required x-y granularity inside each station and region of the muon system. Moreover, the LHCb MWPC chambers are readout differently, depending on their position in the muon system. In region R4 of stations M1-M3 the chambers have anode-wire readout (through decoupling capacitors). In region R3 of stations M1-M3 and regions R1 and R2 of stations M4 and M5 cathode pads are readout. In regions R1 and R2 of stations M2 and M3 a combined readout of wire and cathode pads is used as a consequence of the required granularity. Anode wires are grouped into vertical strips to measure x whereas the y coordinates are provided by the coarser granularity of the horizontal cathode pads. Wires are grouped in pads (*wire pads*) of 4 to 42 to match the required granularity. A complete summary is reported in table 2.2 and a produced chamber is illustrated in Figure 2.4.

Table 2.2: Muon System summary. M: muon station, R: region. Sensitive area, wire pads width and cathode pads size are given per chamber. Number of chambers and physical channels are given per region.

M	**R**	**# cham.**	**Sensitive area (mm^2)**	**Wire pads width (mm)**	**Cathode pads size (mm^2)**	**# Phys. ch.**
M1	R1	24	240×200		10×25	4608
	R2	24	484×200		20×25	9216
	R3	48	968×200		20×100	9216
	R4	192	968×200	40		9216
M2	R1	12	308×253	6.3	37.5×31.3	2688
	R2	24	612×253	12.5	75×31.3	5376
	R3	48	1224×253		25×125	9216
	R4	192	1224×253	50		9216
M3	R1	12	332×273	40.5	40.5×33.7	2112
	R2	24	660×273	13.5	162×33.7	5376
	R3	48	1320×273		27×135	9216
	R4	192	1320×273	54		9216
M4	R1	12	356×293		29×36	2304
	R2	24	708×293		58×72	2304
	R3	48	1416×293		58×145	4608
	R4	192	1416×293	58		9216
M5	R1	12	380×313		31×39	2304
	R2	24	756×313		62×77	2304
	R3	48	1512×313		62×155	4608
	R4	192	1512×313	62		9216

In the previous table, the chamber element readout by one front-end channel is referred to as physical channel. The total number of physical channels in the system is 121,536. In order to reduce the number of channels to be handled by the off-chamber electronics and the trigger processor, the physical channels are

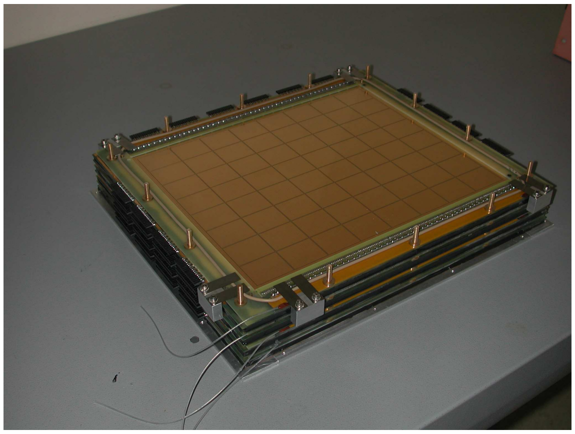

Figure 2.4: A photograph of a produced chamber.

mapped to logical channels [37], whose size is defined by the trigger requirements. In Figure 2.5, an example of the channel mapping is reported: in M2R3 the number of logical channels per chamber is 28, i.e. 1344 logical channels in the whole region. The total number of logical channels in the Muon System is 25,920.

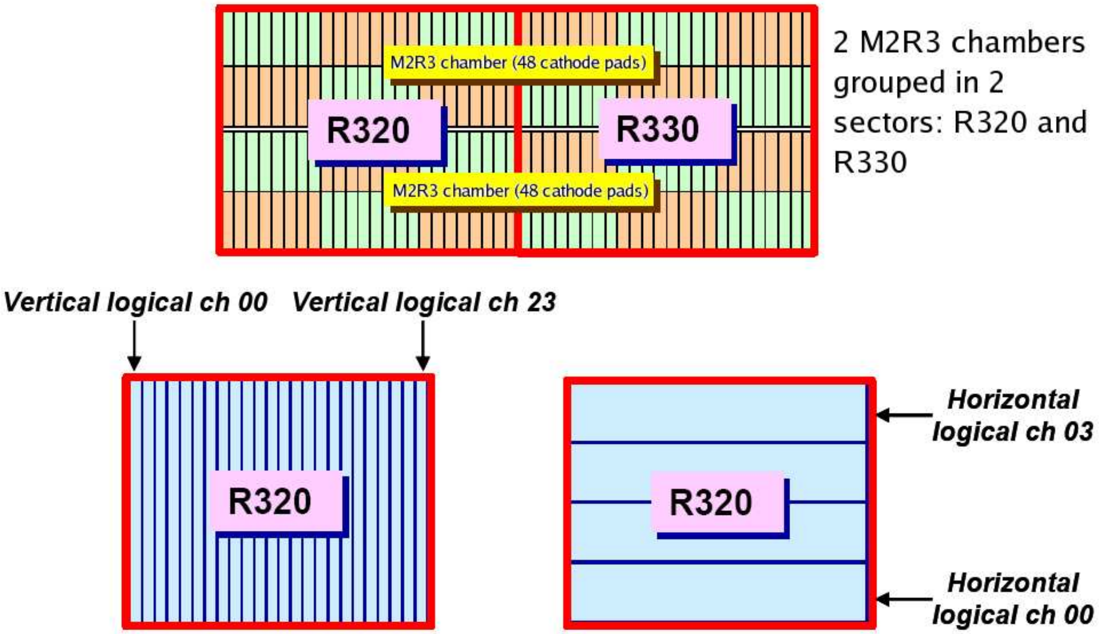

Figure 2.5: Mapping of the physical channels to logical channels in M2R3: two chambers (48 cathode pads each, along x) are grouped to form two sectors, respectively composed by 28 logical channels.

The spatial resolution is given by the dimension of a logical pad, whose structure across the detector represents the logical layout. Each logical pad is obtained from the crossing of one or more horizontal and vertical logical channels, whose dimensions are limited by occupancy and capacitance considerations, according to the detector technology. The logical layout describes the x and y granularity in each region of each muon station, as seen by the muon trigger and the off-line reconstruction. Given the different granularity requirements and the large variation in particle flux in passing from the central part, close to the beam axis, to the detector border, logical pads have different dimensions in each region (Figure 2.6).

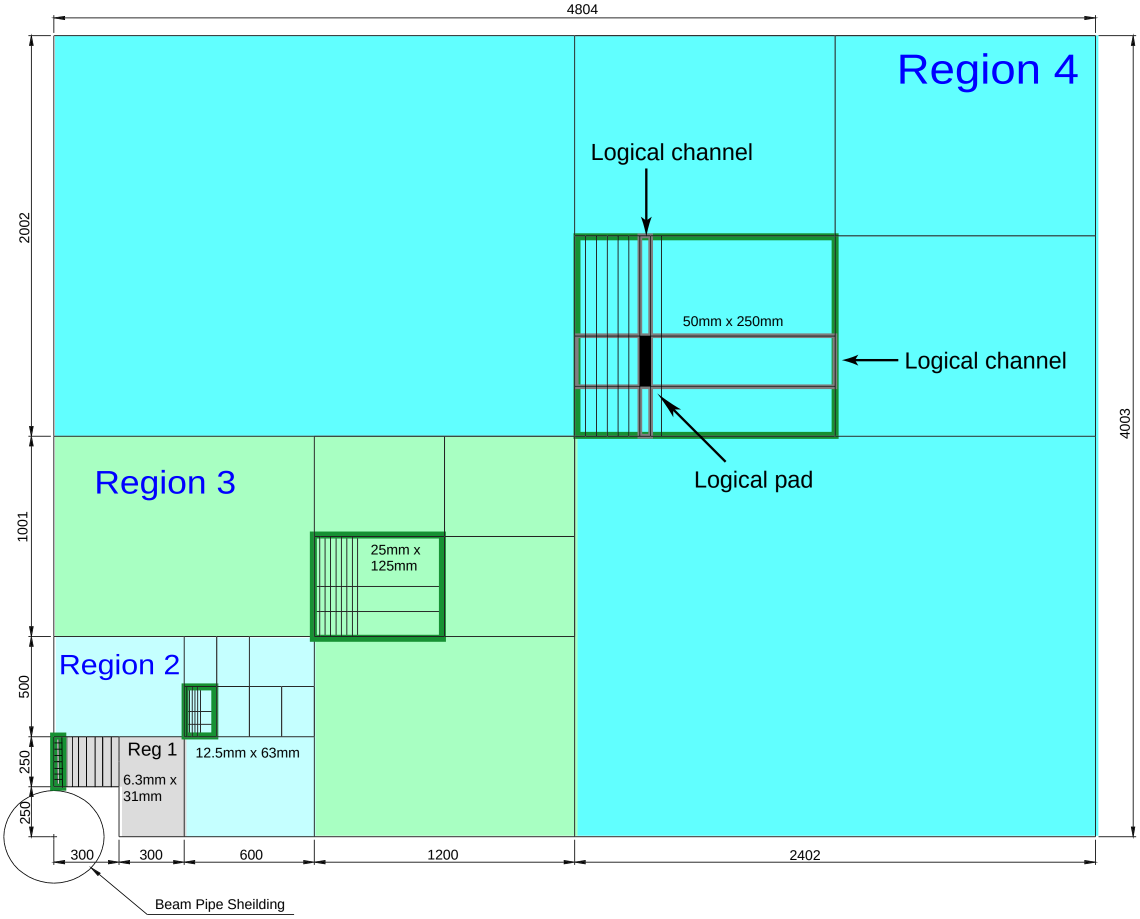

Figure 2.6: Front view of one quadrant of muon station 2, showing the dimensions of the regions. Inside each region is shown a sector, defined by the size of the horizontal and vertical strips. The intersections of the horizontal and vertical strips, corresponding to the logical channels, are logical pads. The region and channel dimensions scale by a factor two from one region to the next.

Region and pad sizes scale by a factor two from one region to the next. The logical layouts in the five muon stations are projective in y to the interaction point. The x dimensions of the logical pads are determined primarily by the precision required to obtain good muon p_{T} resolution for the Level-0 trigger. The y dimension of the logical pads are determined by the required rejection of background triggers which do not point to the interaction region. The resulting y/x ratios are 2.5 in station M1 and 5 for stations M2 and M3. Stations M4 and M5, which are used to confirm the presence of penetrating muons, have ratios of 1.25.

2.4 Level-0 muon trigger

The LHCb muon detector uses the penetrating power of muons to provide a robust muon trigger. It searches for hits defining a straight line through the five muon stations and pointing towards the interaction point (Figure 2.7). The position of a track in the first two stations allows determination of p_{T} .

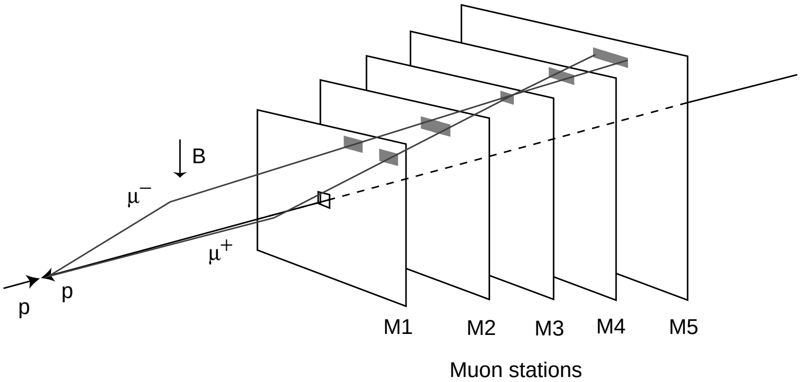

Figure 2.7: Track finding by the muon trigger.

The L0 muon trigger is implemented with the four quadrants of the muon system (Figure 2.6) treated independently. Track finding in each region of a quadrant is performed by 12 processing units, arranged on processing boards in groups of four for regions R1, R3 and R4, and in pairs for region R2. A processing unit collects data from the five muon stations for pads and strips forming a tower pointing towards the interaction point, and also receives information from neighbouring towers.

For each logical pad hit in M3 (track seed), the straight line passing through the hit and the interaction point is extrapolated to M2, M4 and M5. Hits are looked for in these stations in search windows, termed *fields of interest* (FOI), approximately centred on the straight-line extrapolation. The size of the field of interest is dependent on the station considered, the distance from the beam axis, the level of background, and the minimum-bias retention required. When at least one hit is found inside the field of interest for each of the stations M2, M4 and M5, a muon track is flagged and the pad hit in M2 closest to the extrapolation from M3 is selected for subsequent use.

The track position in station M1 is determined by making a straight-line extrapolation from M3 and M2, and identifying in the M1 field of interest the pad hit closest to the extrapolation point. Once track finding is completed, an evaluation of p_{T} is performed for a maximum of 2 muon tracks per processing unit. The two muon tracks of highest p_{T} are selected for each quadrant of the muon system.

The heavy flavor content of triggered events is enhanced by requiring the candidate muons to have high transverse momentum, p_{T} . The Muon System performance is quantified by evaluating the trigger efficiency for selecting muons from b-hadron decays as a function of the Minimum-Bias (MB) retention level. The performance of the L0 muon trigger for the nominal background is illustrated in Figure 2.8.

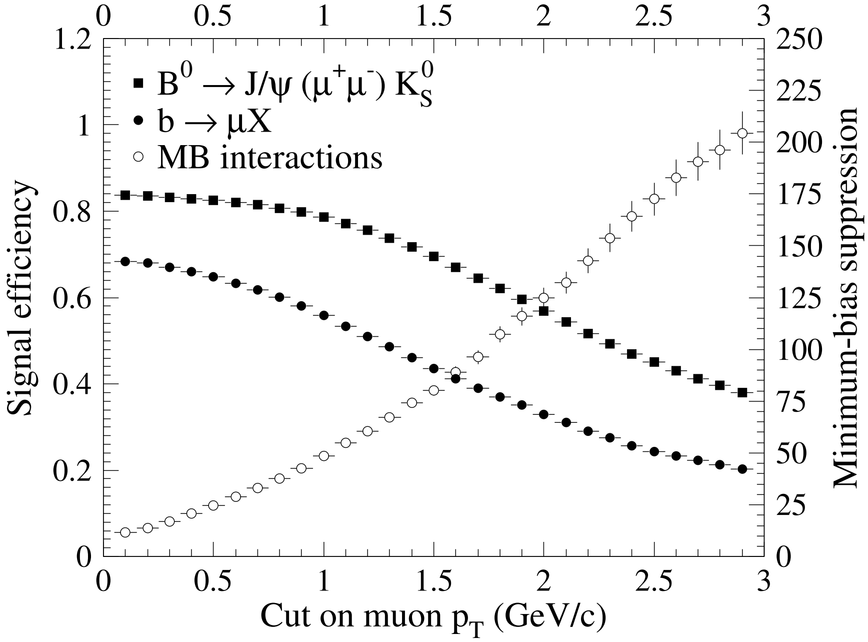

Figure 2.8: Minimum-bias suppression and trigger efficiency.

2.5 The Multiwire Proportional Chambers

As seen in Section 2.2, the physics requirement of the LHCb Muon system is to identify and trigger muons produced in the decay of b hadrons. The trigger logic is designed in such a way that information from all five muon stations is required. Thus, the muon trigger efficiency depends on the single station efficiency ϵ via the relation $\epsilon_{\mathrm{MuTrig}} = \epsilon^5$. In practice, since we work at fixed Minimum Bias rate, the dependence on ϵ is less steep, $\epsilon_{\mathrm{MuTrig}} \simeq \epsilon^{3.5}$. Therefore, in order to achieve a muon triger efficiency of at least 95%, the single-station efficiency has to be higher than 99%. This is ensured by having two detector layers with indipendent readout per station.

As illustrated in table 2.2, the muon system will be equipped, except in the region R1 of the station M1, with the Multiwire Proportional Chambers (MWPC). Since the Charpak's invention in 1968, a massive development of different types of wire chambers started and is still going on nowadays. Today practically every experiment in particle physics uses some type of track detector that has been developed from Charpak's original invention. A schematic diagram of a LHCb MWPC is shown in Figure 2.9 and its principal parameters are summarised in table 2.3.

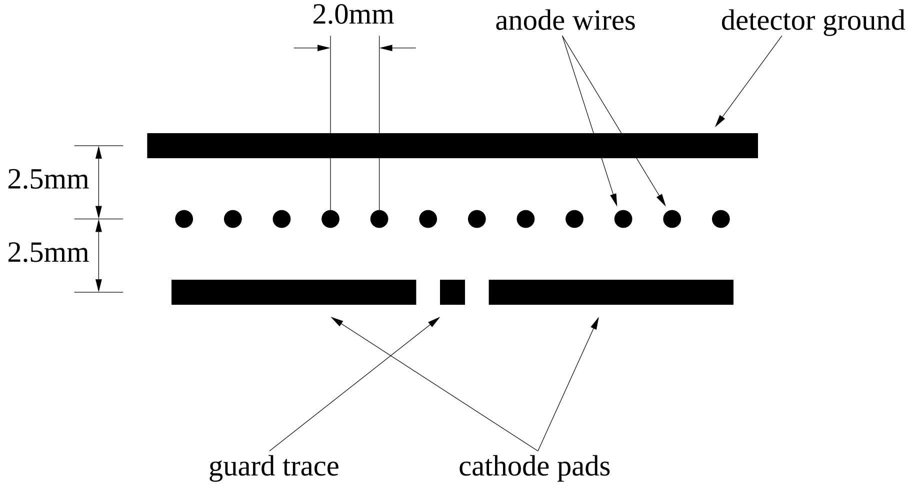

Figure 2.9: Schematic diagram of one sensitive gap in a MWPC.

Table 2.3: Main MWPC parameters.

Parameter	**Value**
Number of MWPC	1368
No. of gaps	4 in M2-M5 and 2 in M1
Gas gap width	5 mm
Wire type	Gold-plated Tungsten
Wire diameter	30 μm
Wire spacing	2 mm
Wire length	250-310 mm
Wire mechanical tension	70 g
Total number of wires	$\sim$3 Million
Gas mixture	$\mathrm{Ar} / \mathrm{CO_2} / \mathrm{CF_4}$ (40:55:5)
Gas Gain	$\simeq 10^5$
Charge / 5 mm track	$\simeq$ 0.8 pC @ 2.7 kV
Av. charge in 10 ns (double gap)	40 fC for wire readout 20 fC for cathode readout
Field on wires	262 kV/cm
Field on cathode	6.2 kV/cm
Max. Operating voltage	3.0 kV

A good time resolution is needed in order to have an efficiency higher than 95% in 20 ns time window. The final MWPC design consists in a chamber containing four sensitive gaps[1] which are connected as two double gaps to two front-end channels, providing high efficiency and fast response. A typical time distribution of a four-gaps chamber is shown in Figure 2.10, which proves an intrinsic time resolution lower than 4 ns r.m.s.

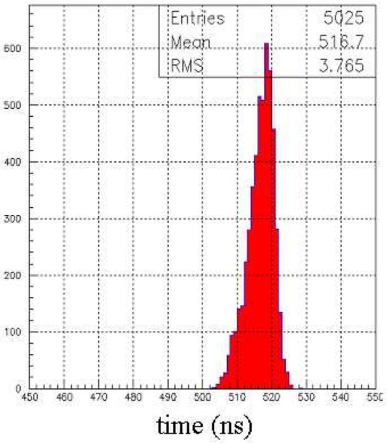

Figure 2.10: Typical time-spectrum of a four-gaps MWPC chamber with the gas mixture $\mathrm{Ar/CO_2/CF_4}$ (40:55:5). The r.m.s is lower than 4 ns. Time increases toward the left.

In Figure 2.11, an example of the efficiency and cluster size with respect to the high voltage for the cathode readout is shown.

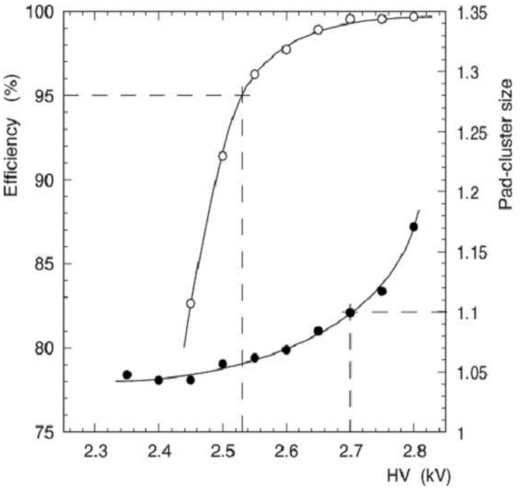

Figure 2.11: Efficiency and cluster size with respect to the high voltage for the cathode readout.

---

[1] Except in station M1, where each chamber contains two sensistive gaps in order to reduce the radiation length X_0.

Due to the different granularities required in each region of the Muon System (see §2.3), 20 different chamber typologies has been designed. The responsabilities for the construction of the 1368 multiwire proportional chambers needed involves six different production sites: one in CERN, three in Italy (Ferrara,Firenze and LNF) and two in Russia (PNPI I & II). The sharing of the chamber production is listed in table 2.4.

Table 2.4: Sharing of chamber production.

Production site	**MWPC type**	**Quantity**	**Spares**
PNPI I	M2R4	152	4
	M3R4	192	8
PNPI II	M2R4	40	4
	M4R4	192	8
LNF	M1R3	48	4
	M1R4	37	3
	M3R3	48	4
	M5R3	48	3
	M5R4	46	4
Ferrara	M1R4	87	3
	M2R3	48	4
	M4R2	24	2
	M4R3	48	4
	M5R2	24	2
Firenze	M1R4	68	2
	M5R4	146	4
CERN	M1R2	24	2
	M2R1	12	2
	M2R2	24	2
	M3R1	12	2
	M3R2	24	2
	M4R1	12	2
	M5R1	12	2

The Rome2 LHCb group has the responsability of performing two final quality tests of two different types of multiwire proportional chamber, one from the Ferrara production site built to equip the region 3 of the station 2 of the muon system (M2R3) and one from the Firenze production site built to equip the region 4 of the station 5 (M5R4). These chambers and final quality test are the object of the study described in the next chapter.

The M2R3 detectors are four-gap chambers with a sensitive area of 1224×253 mm^2. The readout system of each gap consists in a cathode plane composed by 48×2 cathode pads (total 96 pads) 25 mm wide and 125 mm high as shown in

Figure 2.12. Guard traces of 0.5 mm width between the cathode pads are foreseen to minimize the cross talk.

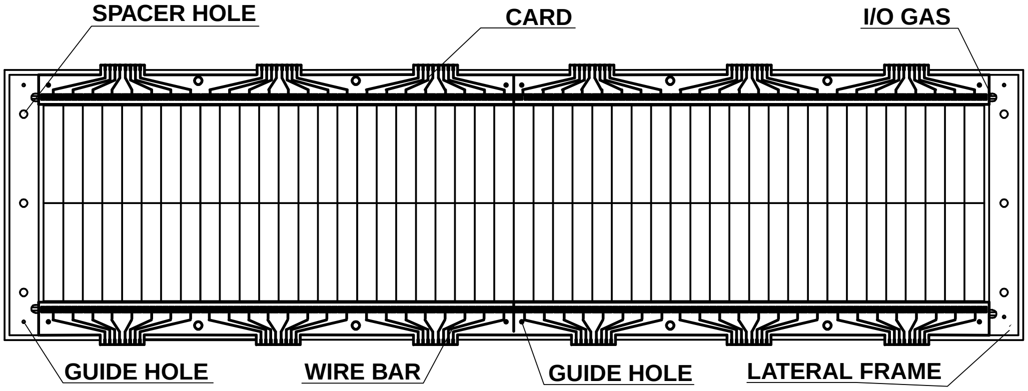

Figure 2.12: Schematic layout of an M2R3 cathode plane.

The panels are the basis of the chamber mechanical structure. A panel consists of two copper clad FR4 (fire-resistant fibreglass epoxy) laminates, interleaved with a core. For the M1 panels, the core is composed by Nomex honeycomb, while for all the other panles the core consists in polyurethanic foam.

On the long sides of the wire panels, wire fixation bars are glued. They have been made according to standard printed circuit board (PCB) technology and are interconnected in groups of 12 wires. A guard wire of 100 μm diameter will be used as last wire to avoid very high fields on the wires at the chamber border.

The High Voltage connection is realized by interface cards which carry the loading resistors and the decoupling capacitors. The HV is distribuited via an HV-bar connected to each group of wires. The same side (long side) cathode pads of the upper and lower two gaps are OR-ed in order to have two double-gap with 96 channels each one (192 FE channels in the full chamber).

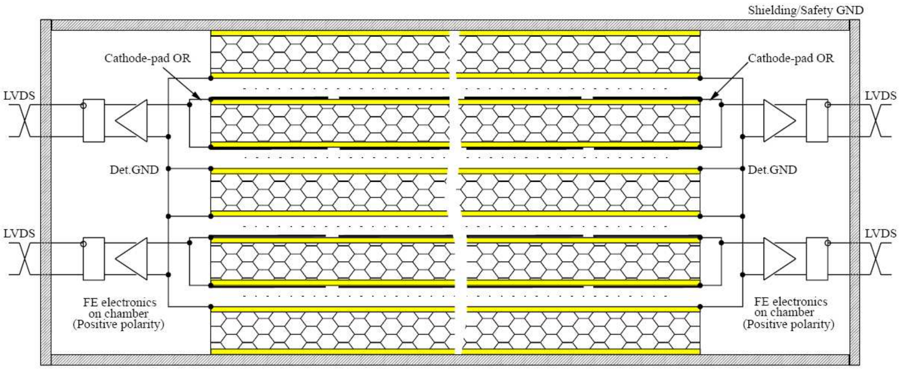

Figure 2.13: A schematic view of the cathode pad readout chain. The figure shows a horizontal section of the chamber with the wires perpendicular to the page.

The front-end electronics has been implemented in two stages; the first stage as a spark protection board (SPB) and the second as the Amplifier Shaper Discriminator (ASD) chip board. The chip board is mounted parallel to and immediately above the SPB. This design allows to minimize the distance the signals must propogate from the chamber. Each board receives the signals from 8 cathode-pads readout channels from each double gap, thus in total 24 ASD chip boards are needed to readout all the 192 FE channels of a full chamber. The SPB will be a 50×70 mm^2 two layers board that contains a system of resistors and diodes for each channel designed to limit the voltage in the event of a spark or discharge. This design fully protects the readout channels up to 3.6 kV applied to the chamber. The chip board is a 50×70 mm^2 four layers PCB containing two ASD chips.

The M5R4 detectors are four-gap chambers with a sensitive area of 1512×313 mm^2. In this case, the readout system of each gap is realised reading directly the signal on the wires: the anode plane is composed by 24 wire pads 62 mm wide as shown in Figure 2.14 and 2.15. The grouping of wires is determined by the required granularity in the x-coordinate.

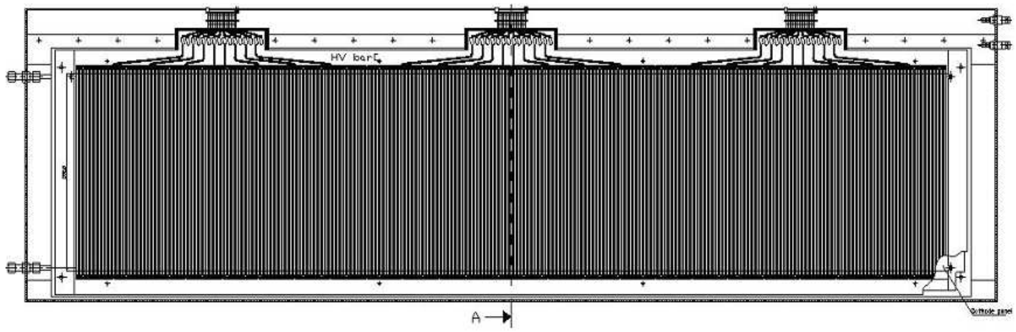

Figure 2.14: Schematic layout of an M5R4 anode plane.

The same side (long side) anode wire pads of the upper and lower two gaps are OR-ed in order to have two double-gap with 24 channels each one (48 FE channels in the full chamber).

The front-end electronics has been disegned with the same scheme of the M2R3 chambers, with the chip boards mounted parallel to and immediately above the SPBs. In the M5R4 chambers each ASD chip board receives the signals from 8 wire-pads readout channels from each double gap, therefore in total 6 ASD chip boards are needed to readout all the 48 FE channels of a full chamber.

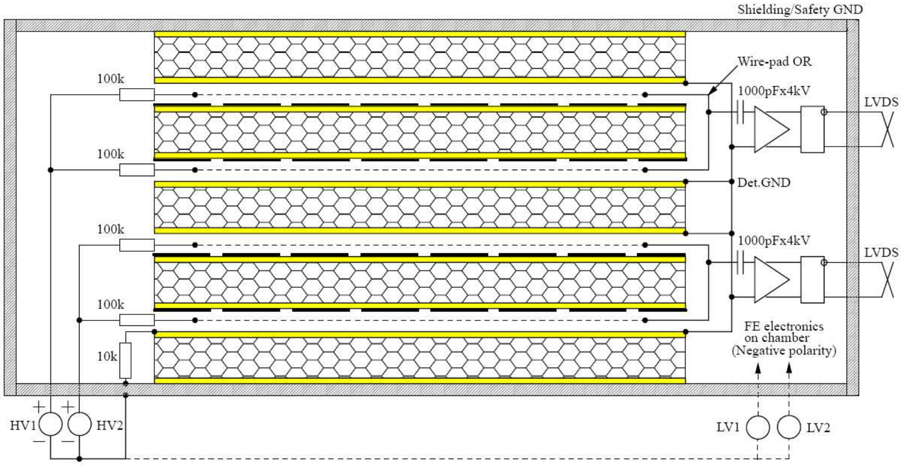

Figure 2.15: A schematic view of the wire pad readout chain. The HV is also shown. The figure shows a vertical section of the chamber with the wires running parallel to the page.

2.5.1 Choice of gas mixture

In Figure 2.16, the behaviour of the efficiency curve and the time resolution of a double gap with respect to the high voltage is shown for four different gas mixtures.

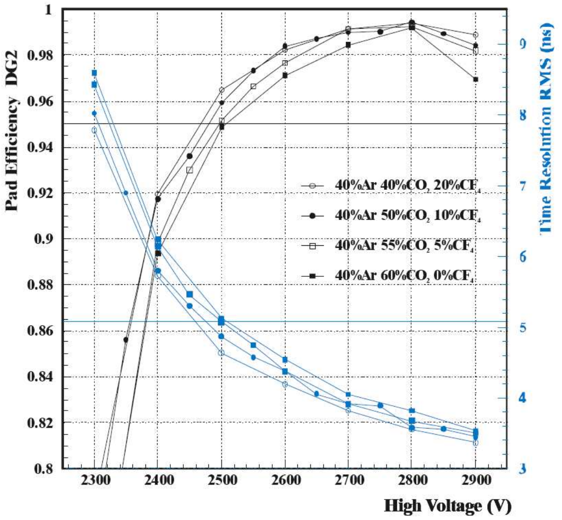

Figure 2.16: Efficiency (black) and time resolution (blue) with respect to the high voltage for four gas mixtures.

The effect of decreasing the CF$_4$ content in the gas mixture is a slightly broader time resolution distribution and a sligth instablility at high voltage. On the other hand, a high content of CF$_4$ is a potential factor of ageing because of the possible etching of the chamber panels (FR4 surfaces). Thus, the MWPC gas mixture has been chosen to be $\mathrm{Ar/CO_2/CF_4}$ (40:55:5).

2.5.2 Choice of wire spacing

The basic geometry of the MWPCs, as described in the TDR [16], leads to an electric field of 8 kV/cm on the cathodes at the operating point. As a consequence, the tolerances for detector construction are very tight, and the large electric field on the cathode might cause additional problems in the long term operation. It is well known that the cathode field can be reduced by increasing the wire spacing (*pitch*), which causes on the other hand a reduced time resolution and in turn a reduced efficiency within a 20 ns time window. Simulation studies [38] showed that the time resolution has an intrinsic limit and cannot be improved in reducing the wire spacing below 1.5 mm. This value has been therefore assumed optimal and used for the prototype studies at the time of the TDR, accepting the drawbacks caused by the large cathode field.

In a recent beam test a detailed performance comparison of double-gap chambers with 1.5 mm and 2 mm wire spacing has been carried out [39]. An important result has been that a time resolution of about 4 ns at the operating point can also be obtained with 2 mm wire spacing, leading to 95% double-gap efficiency within a 20 ns time window, fully satisfying our requirements. Figure 2.17 compares the results for both wire and cathode readout obtained with the two different wire pitches. It was therefore decided to adopt the larger wire pitch for all chambers.

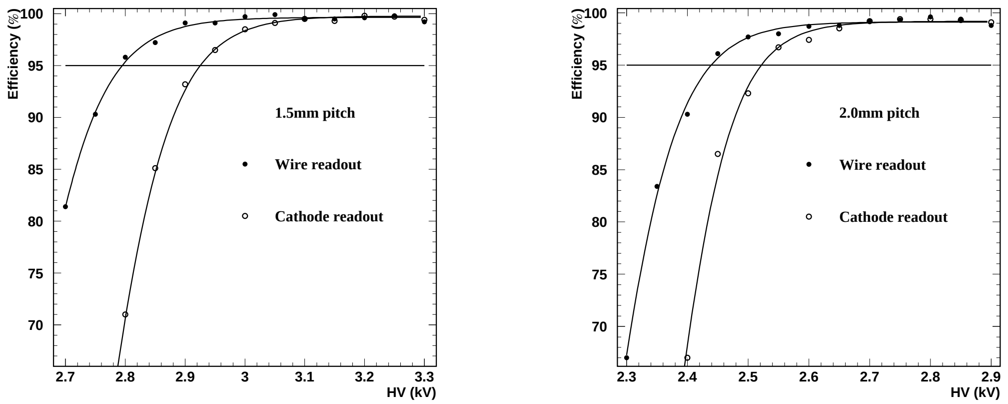

Figure 2.17: Double-gap MWPC efficiency for wire and cathode readout in a 20 ns window with 1.5 mm pitch (left) and 2.0 mm pitch (right).

2.5.3 Tolerances on mechanical parameters

A muon crossing the 5 mm MWPC gas gap will leave an average 50 electrons that drift to the wires in the electric field. The electrons and ions moving in the avalanche close to the wire induce a negative signal on the wire and a positive signal with the same shape and about half the magnitude on each of the cathodes. Since the drift velocity has a weak dependence on the electric field in the gas gap, the choice of the physics and performance parameters of the detector was mainly driven by the need of keeping uniform the gas gain across the chamber.

If G_0 is the nominal gas gain, the requirement is that the gas gain remains in the range (0.8-1.25)G_0 in 95% of the area of a single gap. This gas gain range corresponds to a variation in the high voltage of ±34 V: it is important to remain within this voltage range in order to not leave the efficiency plateau.

In order to keep the gas gain in that range, a detailed study of the wire mechanical tension, wire diameter, gas gap width and all the other physics and performance parameters has been done [38]. In table 2.5, the result of these studies has been summarised together with the tolerances of some parameter in the 95% and in the 5% of the area of a single gap.

Table 2.5: Main MWPC physics and geometrical parameters with the acceptable tolerances.

Parameter	Value	Tolerances
Voltage working point	2620 V	±34 V (95%) ±62 V (5%)
Panel thickness	10.2 mm	±200 μm
Panel flatness		±50 μm
Gas gap width	5 mm	±90 μm (95%) ±180 μm (5%)
Wire tension	70 g	±20 g
Wire spacing	2.0 mm	±50 μm (95%) ±100 μm (5%)
Wire diameter	30 μm	
Wire plane offset		±100 μm (95%) ±200 μm (5%)

2.5.4 Ageing

As previously seen, the performance of the chambers after intense irradiation is a major concern the experiment. In order to prove that the performances of this detector are not deteriorated by the large radiation dose expected in the experiment, an ageing test [40] on two MWPC prototypes of the LHCb muon system was carried out with a ^{60}Co source, the Calliope γ facility at ENEA-Casaccia Research Center, in Rome. The emitted radiation consists of two photons of 1.17 MeV and 1.33 MeV. The source activity at the time of the test was $\sim 8 \times 10^{14}$ Bq.

Over a test duration of 30 days, a charge of 440 mC/cm of wire has been integrated, equivalent to 4.6 LHC year in the region of highest intensity for which MWPC have been considered (M1R2), ~8 LHC years in region M2R1 and more than 10 years in all the other regions, without any appreciable deterioration of the detector.

2.6 Quality control tests

As explained in Section 2.5, the Muon System will be equipped with 1368 multi-wire proportional chambers built in six different production sites. Thus, in order to guarantee the quality of all the chambers produced, the LHCb collaboration has adopted a stringent procedure for the control quality test.

The requirement on the flatness of the panels of $\pm 50\ \mu$m is of critical importance for gas gain uniformity and consequently for the width of the operational plateau. A facility for testing the quality of the produced panels has been developed by our group: a fully automated system provides the measurement of the panel width and flatness by means of two paired optoelectronic displacement measurement sensors (CCD + linear laser) moved along the panel surface. A quality score from 0 up to 10 is assigned to each panel and it must be higher than 6 for acceptance. A distribution of the scores assigned to the panels produced at the time of this thesis is shown in Figure 2.18.

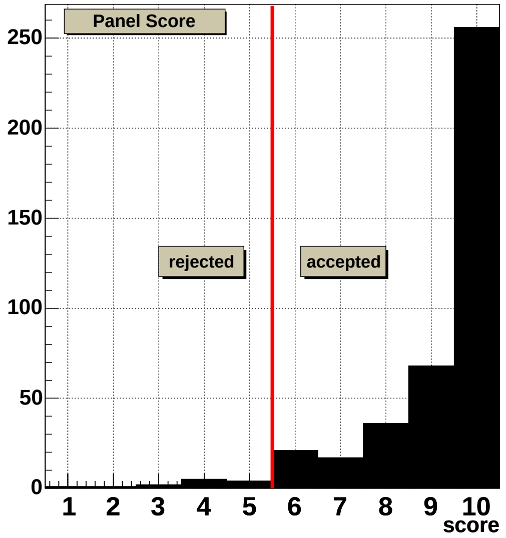

Figure 2.18: Score distribution for 417 panels produced. 95% of them are within the tolerances and have been accepted.

The wire mechanical tension of the produced chambers must be in the range 50-90 g in oder to provide a good electrostatic stability. Various methods have been developed by the production sites to measure the wire tension. Our group has developed an automated system in collaboration with the Ferrara and Firenze sites: wire oscillations are induced by a mechanical excitation and a laser beam, reflected by the oscillating wire, is recorded by a photodiode. The output signal is acquired by a common PC soundcard and from a simple (and automatic) Fourier analysis the resonance frequency is found. The method allows to fully measure one chamber in $\sim$45 minutes. Figure 2.19 shows a typical result of the LHCb wire tension measurement performed with an M3R3 panel.

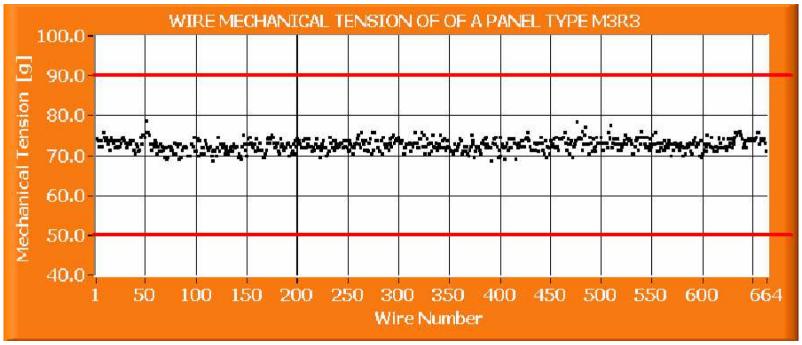

Figure 2.19: Wire tension measurement result for an M3R3 panel. The red lines show the range of acceptable tolerance.

Other relevant quality control tests, not described here, are the wire spacing measurements, the gas leakage measurements and the dark current measurements.

2.7 The muon electronics

The muon system front-end electronics (FEE) has to prepare the information required by the Level-0 muon trigger as quickly as possible and must conform to the overall LHCb readout specifications [41]. Before being sent to the trigger system, signals generated on chambers are processed by the FEE in order to be amplified and digitalized. This operation is done on the chambers themselves by the front-end boards. Because of the fact that the muon system will be equipped with chambers very different in dimensions and readout system, the front-end electronics must match with a wide range of detector capacitance and must accept positive signals and negative signals as well. Moreover, in the highest rate region (i.e. the inner part of M1) the maximal total dose expected is about 1 MRad in 10 LHC years of data taking, which requires the use of radiation hard technology.

The boards are mainly divided in two kind of custom VLSI chips: the *CARIOCA* chip and the *DIALOG* chip.

2.7.1 The CARIOCA chip

The CARIOCA (CERN And RIO Current-mode Amplifier) chip is a radiation hard ASDB chip (Amplifier Shaper Discriminator Baseline restorer) developed by the CERN and Rio de Janeiro group of LHCb using IBM 0.25 μm CMOS technology [42]. It is composed by 8 identical channels. Figure 2.20 shows the scheme of one channel. This is a widely used topology for readout electronics of particle detectors.

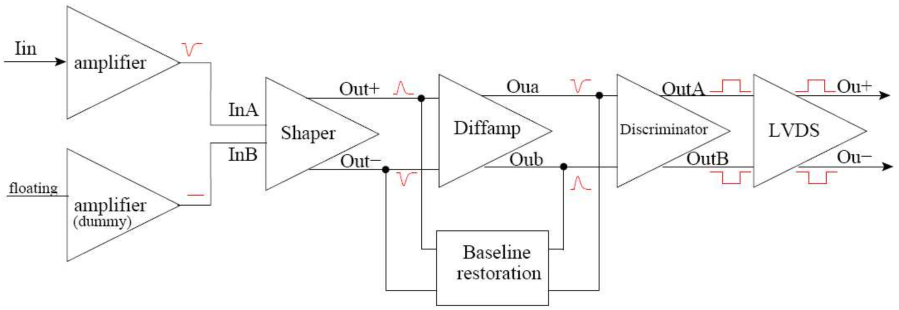

Figure 2.20: Block diagram of a CARIOCA channel.

The main novelty of CARIOCA chip lies in the amplifier, developed following the current-mode approach, which makes the response of the circuit faster, and in an adjustable gain allowing different detector applications. The main task of this electronics is to amplify the chamber signal, before discrimination. Amplified signals go through unipolar shaping and through a non-linear baseline restoration circuit that reduces the baseline fluctuations produced by the long tail of the input signal. This signal is then presented to a discriminator circuit that, depending on threshold level set externally, produces a pulse at the output when the input charge exceeds the threshold. The discriminator output is sent to a LVDS cell and is converted to external low level signals. Each CARIOCA channel consumes about 43.3 mW (46.6 mW) for the positive (negative) amplifier. The signal peaking time in front of the discriminator is 10-15 ns, depending on the detector capacitance that varies from 20 pF to 220 pF. The input resistance of the chip is lower than 50 Ω. The avarage pulse width is within 50 ns. The chip noise is lower than 2 fC up to a detector capacitance of 200 pF. The sensitivity is 16 mV/fC for the positive amplifier and 14.7 mV/fC for the negative one, measured at a detector capacitance of 0 pF. For a capacitance of 220 pF there is a factor 2 less. The sensitivity variations are less than 5% of R.M.S. overall and less than 2.5% of R.M.S. for chip.

2.7.2 The DIALOG chip

On-chamber formation of logical channels from physical channels discriminated by the CARIOCA chip is achieved using a custom integrated circuit for DIagnostics, time Alignment and LOGics, the DIALOG chip [16]. The DIALOG chip is an integrated circuit developed in the IBM 0.25 μm CMOS radiation tolerant technology. The DIALOG chip also allows programming of a delay for each single input channel, and contains features useful for system set-up, monitoring and debugging. Following the data path, we can identify the following blocks: 16 physical channels inputs, a multiplexer selecting either the input signals or a pattern stored on the chip registers, delayers and digital shapers, the physical channels masking box and finally the logical channel generation unit. The DIALOG chip also allows to switch between the AND and the OR feature of the input logical channels, giving therefore the possibility to treat the chamber as a double layer or a single layer.

2.7.3 The CARDIAC board

The front-end board where the CARIOCA and DIALOG chips are connected is the CARDIAC board [43] (CARioca-DIAlog Card). This board deals with 16 physical channels and consists of two ASD chips and one DIALOG chip. Each board can generate a maximum of eight logcal channels and, depending on the local topology, eight, four or two outputs of the card are used. The digital outputs of variable pulse width can also exit the CARDIACs for special tests of the chambers and of the CARDIACs themselves. It is not foreseen to use this feature during normal data taking. A total of 7536 CARDIACs are foreseen in the system.

The CARDIAC, shown in Figure 2.21, is a 6 layer PCB: 2 plane layers (power and ground) and 4 connection layers. On the top layer, that lies on the outer side of the chamber, one DIALOG chip, the power, the I^2C interface and the output connectors are mounted, while on the bottom layer (inner side of the chamber), two CARIOCA chips, the input connectors and the LVDS terminations (outputs of the two CARIOCAs) are mounted.

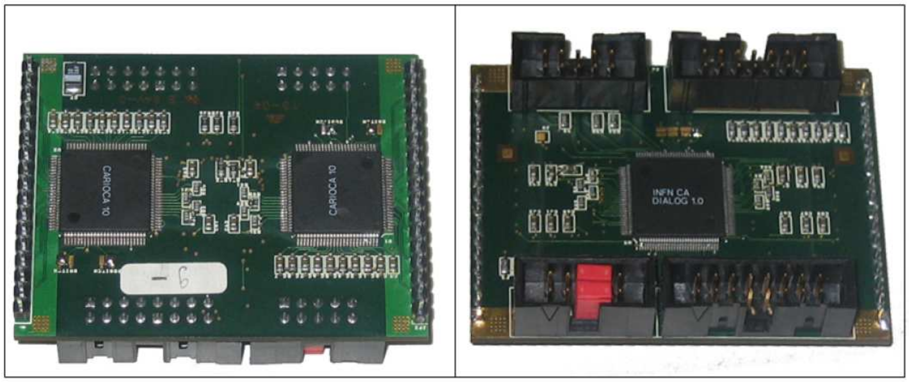

Figure 2.21: The CARDIAC bottom layer with two CARIOCAs (left) and top layer with one DIALOG (right).

2.7.4 The ASDQ++ board

Since at the time of this thesis the final front-end electronics (CARIOCA, DIALOG and CARDIAC) were yet not ready, all the chambers tested were equipped with the 16 channels Amplifier Chip Board (ACB) based on the ASDQ++ chip [44]. The chip is designed to readout both the wire pads and the cathode pads. A simple scheme of the chip is shown in Figure 2.22.

A threshold calibration of the ASDQ++ chip has been performed in order to obtain a relationship between the minimum allowed voltage height of the signal and its content in charge. In Figure 2.23 we report the calibration plot of the sensitivity (fC/mV) of an ASDQ++ positive chip. The result is a sensitivity of (24.8±78.6) fC/mV when the threshold is measured on the ASDQ controller and (24.5±56.4) fC/mV when the threshold is measured directly on the ASDQ board.

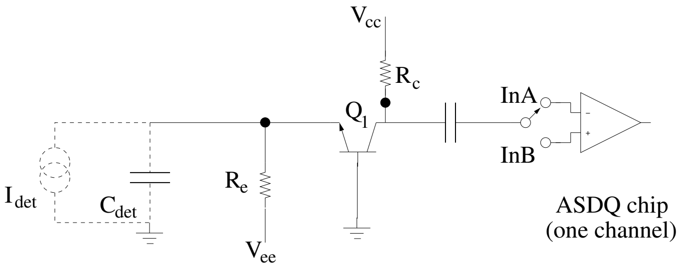

Figure 2.22: The ASDQ++ chip schematics.

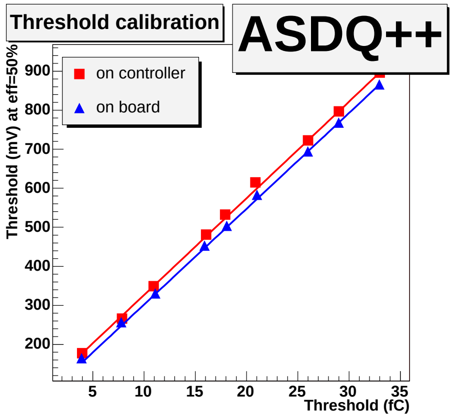

Figure 2.23: The threshold calibration plot for a positive ASDQ++ chip.

2.7.5 The off-detector electronics

The amplified and digitalized signals coming from the FEE are sent to the off-detector electronics in order to complete the logical channels generation and to be tagged with their own bunch crossing identifier. Two kind of boards have been developed to execute these functions: the Intermediate Boards (IB) and the Off-Detector Electronics Boards (ODE).

Since, in regions R3 and R4 of stations M2 to M5 and region R2 of stations M4 and M5, physical channels from different front-end boards and chambers must be combined, the logical channel formation requires a further step of logical operations, performed by the Intermediate Boards. The 152 IB boards needed to instrument the muon detector will be located outside the chamber, on the racks near the LHCb apparatus. Because of the radiation level near the detector (~ 2 kRad) radiation tolerant device have been used to implement the logic.

Once generated, the logical channels are sent to the Off-Detector Electronics, where they are assigned the corresponding bunch crossing identifier and dispatched to the L0 trigger. The ODE contains also the L0 pipelines, the L1 buffers and the DAQ interface. The 148 ODE boards nedeed will be located on the left and right side of the muon detector.

In addition to the electronic system described previously, it is important to cite another system: the Experiment Control System (ECS). The ECS is a distributed system based on CAN bus and it performs basic control and monitoring of the ODE boards; it also controls the FEBs through specially designed Service Boards (SB). The architecture of this system is based on ELMB (Embedded Local Monitor Box [45]) a special CAN node board designed by the ATLAS collaboration to operate in a moderate rate environment. The ELMB is a general-purpose small plug-on module, comprising two commercial 8-bit micro-controllers and one CAN-Controller chip. There are two ECS subsystems, one servicing the front-end boards through the SBs and comprising 24 CAN branches, the other servicing the ODE boards via 10 CAN branches. The CAN branches are controlled by six PCs placed in the counting room.

The Service Boards (SBs) (see Figure 2.24) are 9U size VME boards. Each SB houses four ELMB CAN nodes. Each ELMB CAN node can handle two I^2C buses. These buses are extended up to 10 m (long distance branches) using an LVDS driver. At the end of the long distance branch a LVDS receiver placed on a chamber will drive ten DIALOG chips on the FEBs with the standard LVTTL I^2C bus. At start-up, a remote CAN command will trigger a local process in the ELMB that will write the registers inside the DIALOG chip. There are two ways to access and control the registers of the DIALOG chip: the first requires the use of special tasks running inside the ELMB, which performs all the operations, the second involves running from the control PC, using I^2C instructions. The use of the ELMB local intelligence reduces the load of the PC processors and of network communications.

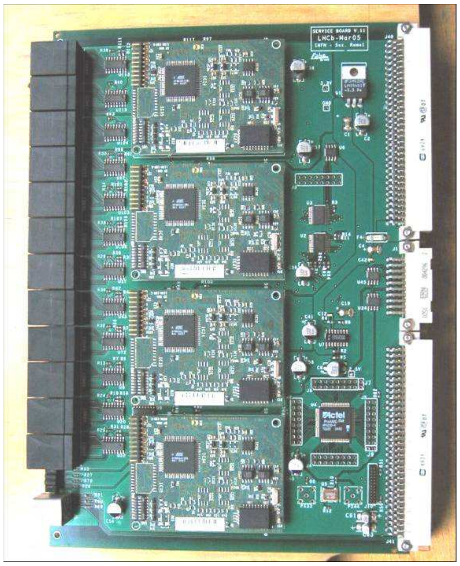

Figure 2.24: The Service Board.

Another function of the SBs is to provide the power supply generation circuitry for the FEBs. The appropriate voltage levels are generated on the service boards and transmitted to the FEBs. As the distance between the SBs and the FEBs is 10 to 15 m, a voltage regulation facility is envisaged for the FEBs.

The SBs are also used to send and receive signals useful for front-end calibration and to monitor the correct operating conditions of the chambers and front-end electronics (e.g. temperature). A system to pulse the front-end channels for test and diagnostics is also envisaged.

The SBs are placed to either side of the detector, in the racks housing both the intermediate boards and the ODE boards. In total 144 SBs are foreseen.

Chapter 3

Studies on Multiwire Proportional Chambers

3.1 Introduction

Before to be definitely accepted and shipped to CERN for the installation in the muon detector, the produced chambers must undergo two final quality tests. First of all the chamber must be inspected for uniformity in its response with respect to the others chambers. In addition, a sample of chambers has to be tested with cosmic rays to determine the efficiency plateau and time resolution.

In this chapter, the work is focused on the gas gain uniformity test and on efficiency measurements with cosmic rays. In particular, the Rome2 group has developed a cosmic rays test station which has been used to study the tracking, to measure the efficiency and to perform the gas gain uniformity measurements.

3.2 Gas gain uniformity test

The gas gain uniformity of each double-gap is evaluated on the strenght of the following criteria (need to be valid in the 95% of the total area):

$$\begin{array}{lll} \text{class A} & \text{if} & \dfrac{<G>}{\sqrt{2}} \leq G(x,y) \leq \sqrt{2}\ <G> \\ \text{class B} & \text{if} & \dfrac{<G>}{\sqrt{3}} \leq G(x,y) \leq \sqrt{3}\ <G> \\ \text{class C} & \text{if} & \text{all the other cases} \end{array} \qquad (3.1)$$

where $G(x,y)$ is the gas gain of a gap in the (x,y) position and $< G >$ is the average gas gain over all the gaps of the same type. The requirement is that the full chamber is classed as AA or AB (*good*). The range of the above criteria corresponds to a voltage range equal to ΔV=±53 V (class A) and ΔV=±84 V (class B). The requirement ensures that all the chambers exhibit a similar gain response and therefore will be operated well inside the region of full efficiency, allowing to foresee an HV scheme with several gaps chained in parallel.

Since the gas gain is proportional to the current drawn by the gap, the gas gain uniformity is normally measured making use of a radioactive source and monitoring the current drawn by the chamber. Some production sites (LNF, PNPI) have chosen intense γ-sources, in order to induce in the chamber a resonable current (200-300 nA per gap at 2750 V). The current drawn by each gap is monitored while the lead case containing the source is moved along the surface of the chamber. These measurements allow to check the gain uniformity within each gap and to compare different chambers among them. Various fully automated system has been developed by each production site. The Rome2 LHCb group has developed a system for the Ferrara production site, shown in Figure 3.1; due to safety reasons, a less intense β-source has been preferred (20-30 nA per gap at 2750 V). A similar system is also adopted in Firenze.

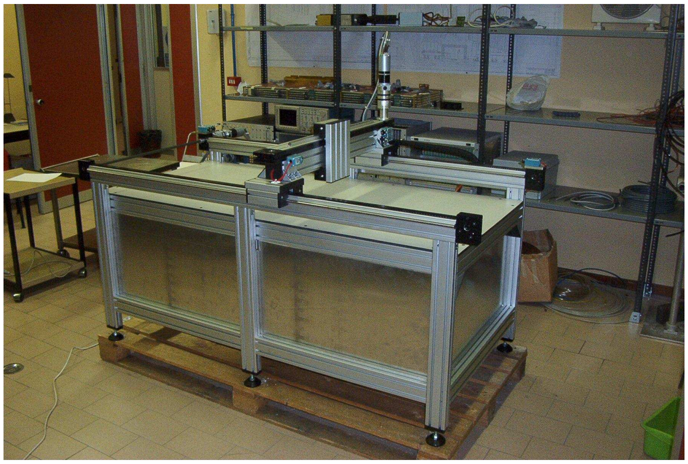

Figure 3.1: A photograph of the Rome2 system for gas gain measurements.

The system consists in a table for the housing of the chamber above which two motors[1] move the lead case containing the source along the x and the y direction.

A custom LabView^{TM} software controls the x-y motion via a serial cable, positioning the source over many different points across the chamber surface. The same LabView^{TM} software controls an ammeter connected to the four chamber gaps and records the current drawn by each gap. Three measurements are performed for each cathode (wire) pad, equally distributed along the long side of the pad. A typical result of the measurement is shown in Figure 3.2 for a M2R3 chamber. The measurement was performed monitoring the current in the first two gaps simultaneously and then, reversing the chamber, monitoring the current in the remaining two gaps. Because of the electrons absorption in the panels of the upper gap, the currents drawn by gaps 2 and 3 are much more lower. The current

---

[1] Technosoft^{TM} IM232-MA Intelligent Brushless motors.

map $I(x, y)$ gives the gas gain uniformity of the gap itself. Note that the current drops corresponding to the gap edges is due to a geometrical effect.

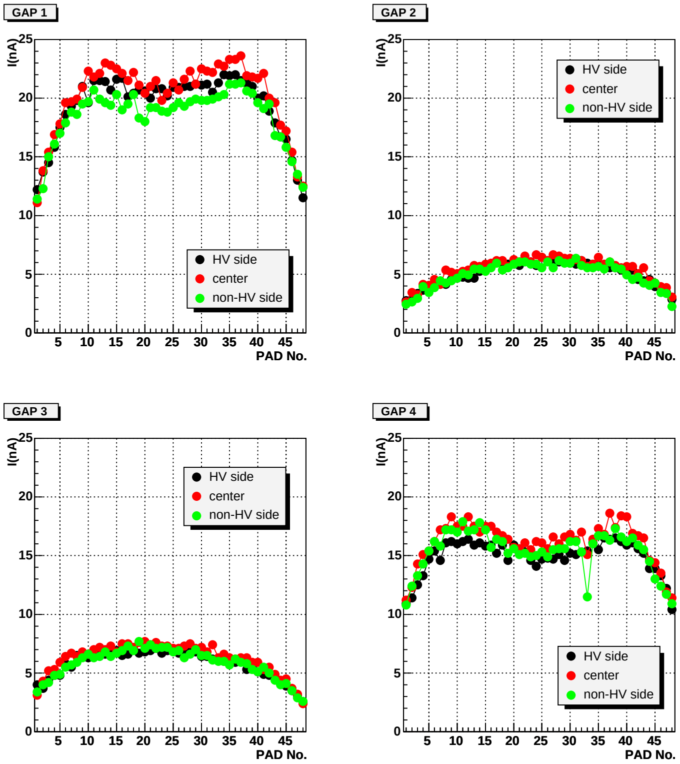

Figure 3.2: A typical result of current measurements performed with the Rome2 system.

In order to class each double-gap on the strenght of the criteria reported in Eq. 3.1, the current of each double-gap is integrated along the y position (short side) and the mean, the minimum and the maximum current values with respect to the x position are taken. An example of the classification plot for the M5R3 chambers is shown in Figure 3.3. The mean, minimum and maximum current values have been normalised with the $< I >$, $< I_{\rm min} >$ and $< I_{\rm max} >$ values rispectively, where the average is computed over all the chambers tested.

Our group has also developed an alternative method to measure the gas gain uniformity of the multiwire proportional chambers by means of the cosmic rays. This method, which does not make use of a radioactive source, is therefore much more reliable from the point of view of the safety rules. The method will be described in details in §3.6.

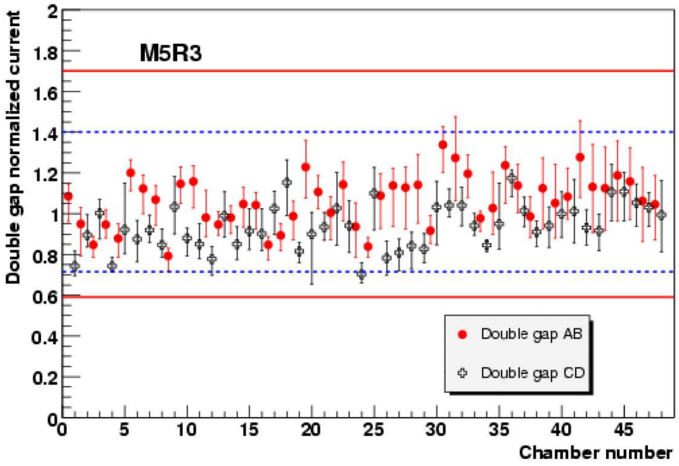

Figure 3.3: An example of a classification plot for M5R3 chambers.

3.3 The cosmic rays test station

The use of a cosmic ray stand allows to measure the efficiency and time performances of the chambers produced. The requirements are that the efficiency of each double-gap is higher than 95% (in 20 ns time window).

For this goal, the Rome2 LHCb group has designed and developed a cosmic rays test station. The test station allows to perform precise chamber efficiency measurement (each pad) and also to study the tracking capabilities of the multiwire proportional chambers. This section will be focused on the characteristics of our cosmic rays stand and on the results we obtained.

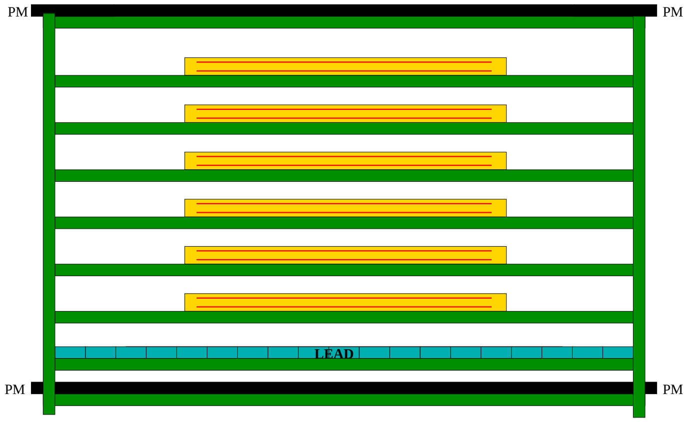

Figure 3.4: Schematic diagram of the cosmic rays test station.

The cosmic rays test station developed by the Rome2 LHCb group is a 240 cm × 190 cm × 80 cm test stand, designed to house and to test up to six chambers contemporaneously (see Figure 3.4). The trigger is provided by two scintillators plane 240 cm × 60 cm, while a lead plane (2.5 cm thick) between them allow to cut the soft component of the cosmic rays. In Figure 3.5, it is shown a frontal view of the cosmic rays stand during a test on four Ferrara (M2R3) chambers.

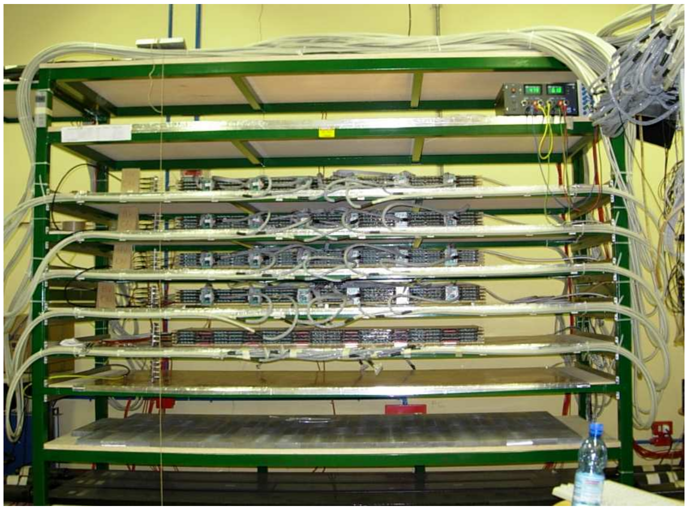

Figure 3.5: A frontal view of the cosmic rays test station.

3.3.1 Trigger logic

Each trigger plane is composed by three scintillator bars 240 cm × 20 cm (thickness 3.5 cm), readout on both sides by two photomultipliers. The three outputs of the left and right side photomultipliers of the top and bottom scintillator plane are logically OR-ed (Figure 3.6).

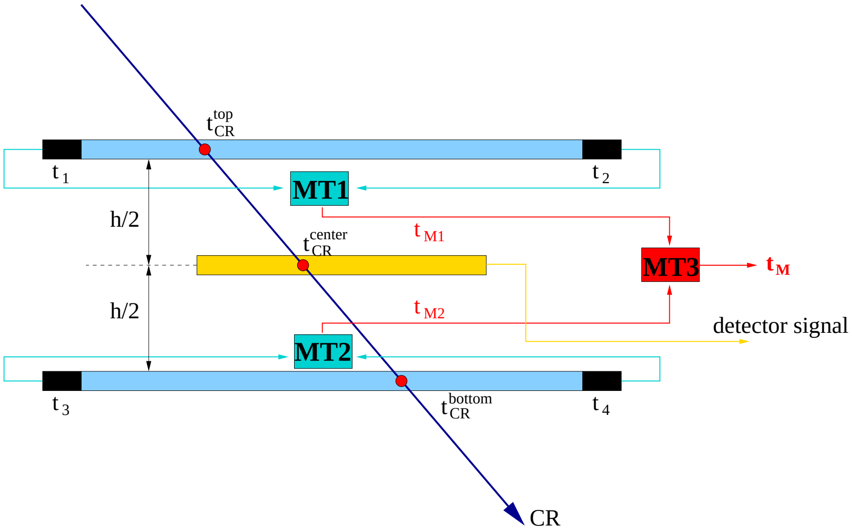

Figure 3.6: A schematic diagram of the trigger logic.

When a cosmic ray crosses the test station, two signals come from the top scintillator plane characterized by the time:

$$t_1 = t_{CR}^{top} + \frac{s_1}{v} \quad , \quad t_2 = t_{CR}^{top} + \frac{s_2}{v}$$

where t_{CR}^{top} is the impact time of the cosmic ray on the top scintillators plane and $s_{1(2)}$ is the distance between the impact point and the left (right) photomultiplier.

This two signals are sent to a meantimer module[2] (MT1) where they are discriminated (the module is a constant fraction discriminator) and the mean time is computed (t_{M1}):

$$t_{M1} = \frac{t_1 + t_2}{2} = t_{CR}^{top} + \frac{s_1 + s_2}{2v}$$

where v is the light propagation velocity inside the scintillator bar.

Similarly, the two signals characterized by the time t_3 and t_4 coming out from the bottom photomultipliers plane are sent to a second Mean Timer (MT2) and the mean time t_{M2} is computed:

$$t_{M2} = \frac{t_3 + t_4}{2} = t_{CR}^{bottom} + \frac{s_3 + s_4}{2v}$$

where t_{CR}^{bottom} is the impact time of the cosmic ray on the bottom scintillators plane and $s_{3(4)}$ is the distance between the impact point and the left (right) photomultiplier.

The two output signals t_{M1} and t_{M2} are then sent to a third Mean Timer (MT3) which gives:

$$t_M = \frac{t_{M1} + t_{M2}}{2} = \frac{t_{CR}^{top} + t_{CR}^{bottom}}{2} + \frac{l}{2v}$$

where l is the total lenght of the scintillator plane.

The cosmic ray time t_{CR}^{center} referred to the center of the station is:

$$t_{CR}^{center} = t_{CR}^{top} + \frac{h}{2c} \qquad \text{or} \qquad t_{CR}^{center} = t_{CR}^{bottom} - \frac{h}{2c}$$

and adding these two equations we obtain:

$$t_{CR}^{center} = \frac{t_{CR}^{top} + t_{CR}^{bottom}}{2} = t_M - \frac{l}{2v}$$

i.e.,

$$t_M = t_{CR}^{center} + \text{cte}$$

Thus, each trigger time is, except for a costant, the time of the cosmic rays at the center of the station. This feature is fundamental because it allows to reduce drastically the trigger time jitter. In Figure 3.7, the trigger time distribution measured with a finger scintillator, is shown: the time resolution is rather good, σ=1.34 ns.

---

[2] CAEN^{TM} 2 Channels CFD AND Mean Timer N253

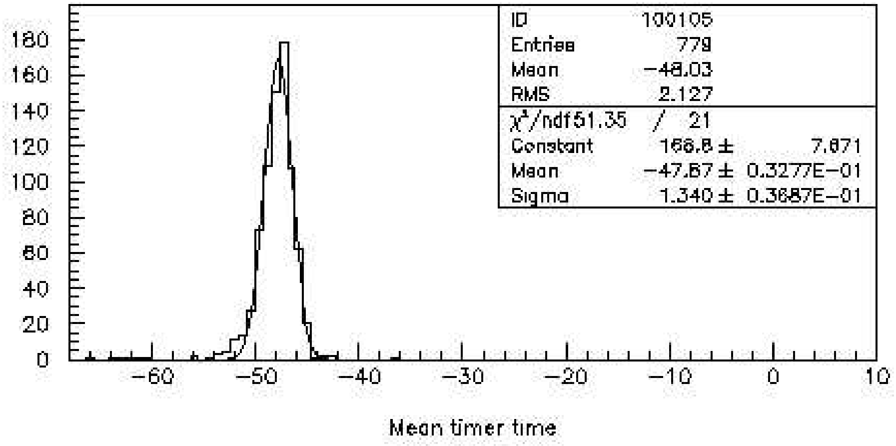

Figure 3.7: Time distribution of the trigger. The time resolution is σ=1.34 ns.

The setup described gives a trigger rate of about 10 Hz, that means a statistics of about 10^5 events in three hours.

3.3.2 Data acquisition

The signals coming from the chambers together with the trigger are collected by the ACQ boards developed by the Rome2 and LNF LHCb groups. The chambers are connected to the ACQ boards via LVDS shielded cables.

The ACQ board is a VME 6U standard Pattern Unit. A SPILL signal, injectable via a standard NIM input, disables the VME cycles and starts the acquisition cycle, enabling:

- 24 bits hit counter (Scaler), one for each channel.
- 16 bits trigger counter (TRC).
- 16 bits TDC to measure the trigger to SPILL delay (TSD).

Each trigger in time with the SPILL generates, after a programmable delay and with a programmable width (20-100 ns), an internal gate signal. This gate enables a 2 bits hit counter per channel (CHC). Each ACQ boards consists of 64 LVDS input channels with a programmable common delay (CHD) in steps of 6.25 ns between 12.5 ns (minimum) and 1600 ns (maximum). The scaler functionality implemented in the board could be very useful to perform electronic and detector noise measurements. The ACQ cards are readout via a dedicated VME Motorola CPU on which a C++ software developed by the Rome2 group controls both the data acquisition sys-

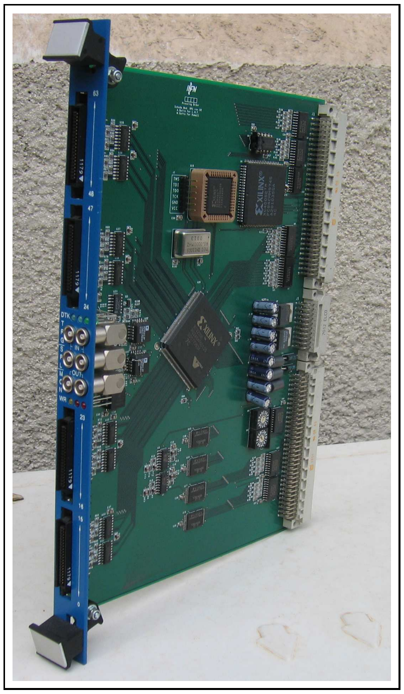

Figure 3.8: ACQ board

tem and the high voltage power supply.

3.4 Track reconstruction

By means of our cosmic rays test station, we studied the tracking with cosmics in the M2R3 and M5R4 chambers. The reconstructed tracks will be then used to measure the chambers efficiency (§3.5) and the gas gain uniformity (§3.6).

3.4.1 Hit multiplicity

The cosmic rays test station has been equipped with four double-gap chambers powered with a high voltage of 2700 V (each single gap). As consequence of the different average charge of the signals (see table 2.3), the FE electronics (ASDQ++) threshold were set to the value of 250 mV for the M2R3 chambers and 450 mV for the M5R4 chambers, i.e. about 7 fC and 15 fC respectively according to the calibration shown in Figure 2.23.

Since each double-gap of a chamber can be readout indipendently, the described setup allows us to handle a total of 8 double-gaps, which henceforth are referred to as *tracking layers*. Thus, in each event 7 tracking layers are used to reconstruct the track and evaluate the efficiency in the eighth layer. Of course, this analysis can be performed cyclically and therefore each run (made by 10^5 events) can be used to study all the chambers in the station.

In Figure 3.9 are shown two examples of the hits multiplicity distribution of the events, respectively in a M2R3 chamber and a M5R4 chamber.

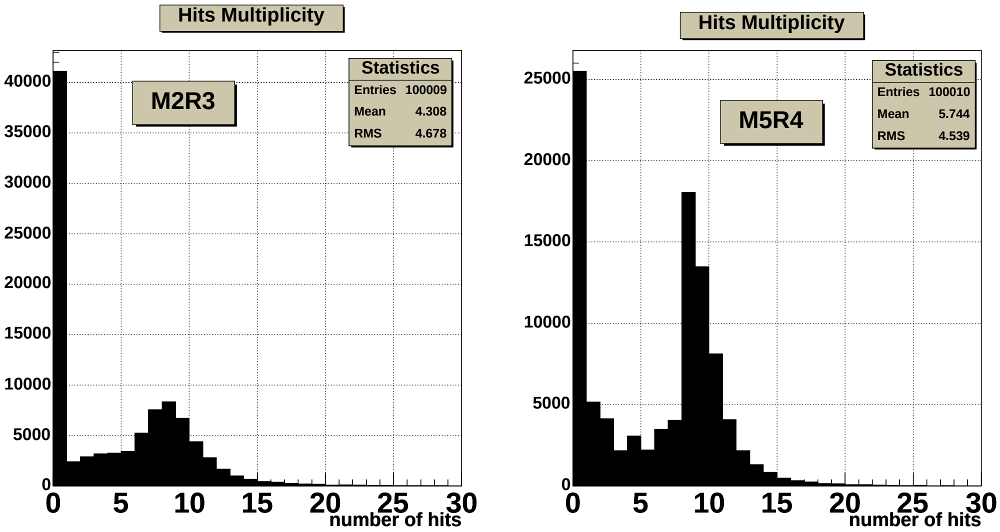

Figure 3.9: Hits multiplicity in a M2R3 chamber (left) and in a M5R4 chamber (right). The large amount of empty events is due to a geometry effect.

The large amount of empty events (0 hits) present in both plots is a consequence of the different geometries between the sensitive areas of the scintillator trigger and the tested chambers; this effect is obviously larger in the M2R3 chambers which have a sensitive area lower than the M5R4 chambers by a factor of about 1.5.

The two hits multiplicity distributions show a peak corresponding to a number of hits equal to 8, as one expects having eight layers in the station.

3.4.2 Tracking algorithm

A custom C++ software has been developed in order to perform the track reconstruction, while the ROOT Data Analysis Framework [46] has been used to display the results. The custom software uses the *Field of Interest* (FOI) method as the muon trigger will do in the LHCb experiment (see §2.4). In Figure 3.10 a typical event with a total of 10 hits is shown, where each layer is depicted with a white line; in this example, the layer we want to study is the layer 4 and it is highlighted in light blue. Note that the cosmic ray is assumed to cross each hitted pad in its center.

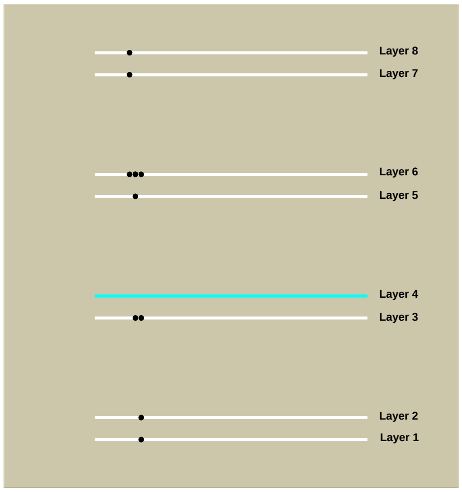

Figure 3.10: Example of an event with 10 hits. The layer under study is the layer 4 (light blue). In white the other layers.

Starting from the lower layer (layer 1) a straight line is traced from each hit of the layer 1 to each hit of the layer 2; in the example above, there is one hit per layer and therefore just one straight line has been traced (Figure 3.11a).

In general, each line traced is than extrapolated on the third layer and, around the extrapolation point, a FOI 3 pads wide is opened: if at least one hit is found inside the FOI, then a new line is traced and saved, otherwise the layer is skipped and the software moves to the next one. In our example, the only line is extrapolated on the layer 3 and two hits are founded inside the FOI: two new lines are therefore traced and saved (Figure 3.11b).

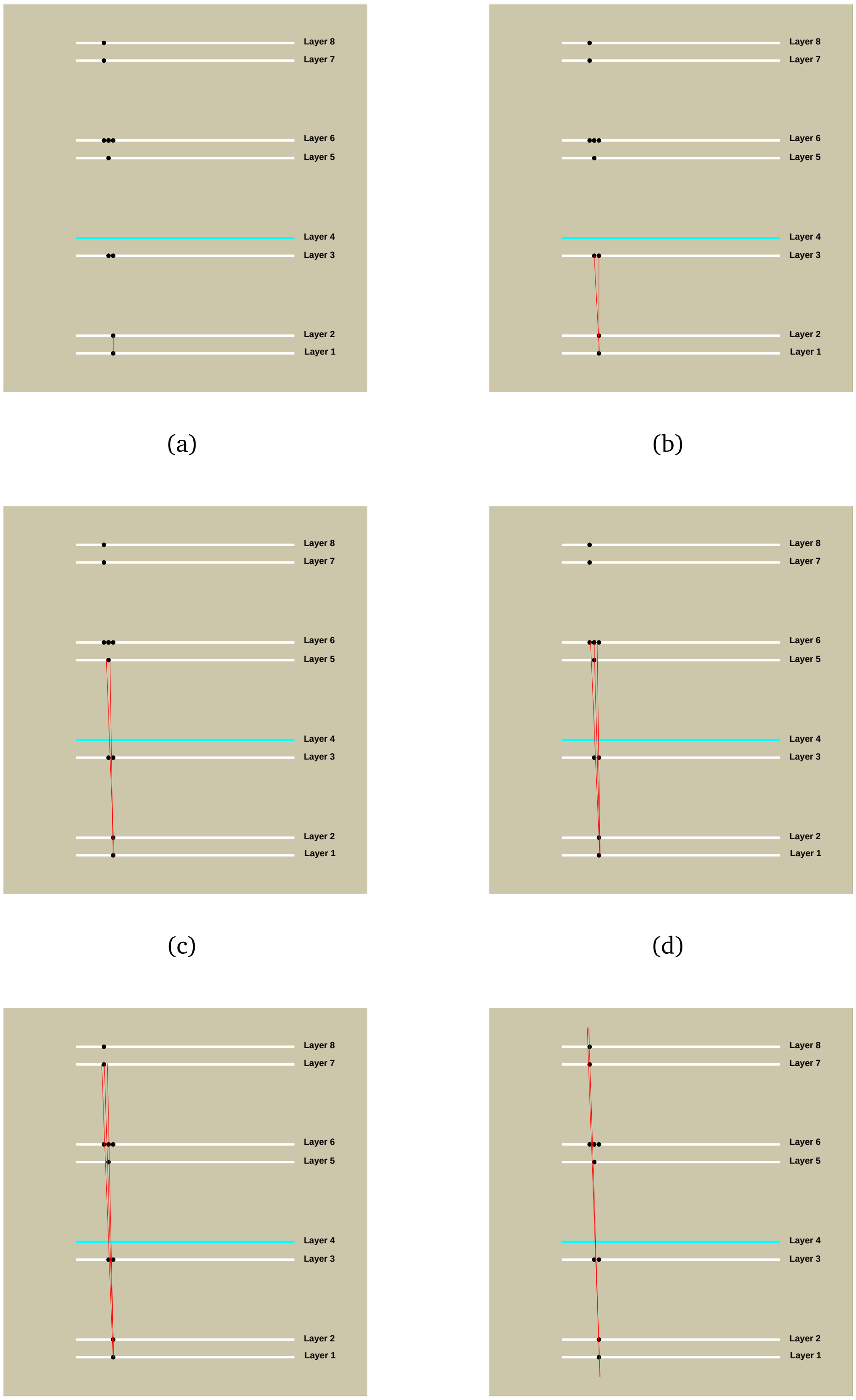

(a) (b)

(c) (d)

(e) (f)

Figure 3.11: Track finding method step by step.

The saved tracks are then extrapolated to the next layer and again a FOI is opened around each extrapolation point; looking for at least one hit inside each FOI allows to decide if to save or to discard the examinated line. In this example (layer 4 under study), the next layer is the layer 5: one hit is founded inside the two FOIs opened and therefore two new lines are traced and saved (Figure 3.11c).

The track finding goes on following this method until the last layer (Figure 3.11 d, e, f); at the end, if more than one line is a candidate track, the track is chosen by means of the Least-Squares method. The only requirement is that the track is composed by at least five layers out of seven. If this requirement is satisfied, the candidate track becomes a reconstructed track (Figure 3.12) and it can be used to evaluate the efficiency of the layer under study.

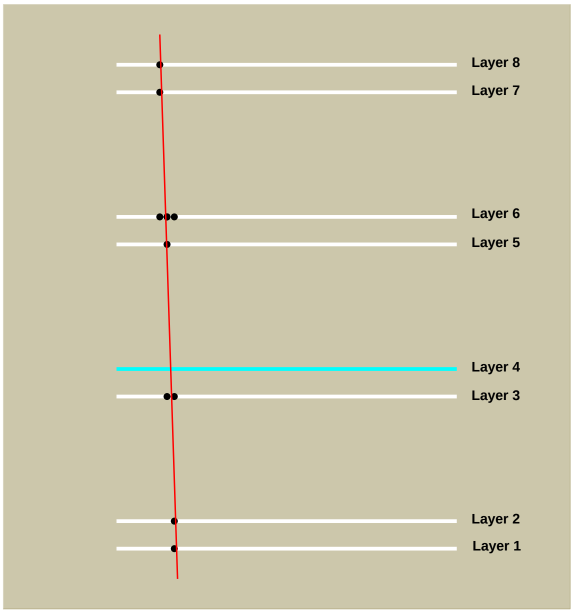

Figure 3.12: Reconstructed track.

3.4.3 Event selection

As already shown in Figure 3.9, there is a large amount of empty events due to a geometry effect; the first step in the event selection consists therefore in rejecting this class of events. In Figure 3.13 is shown the event multiplicity after this first cut.

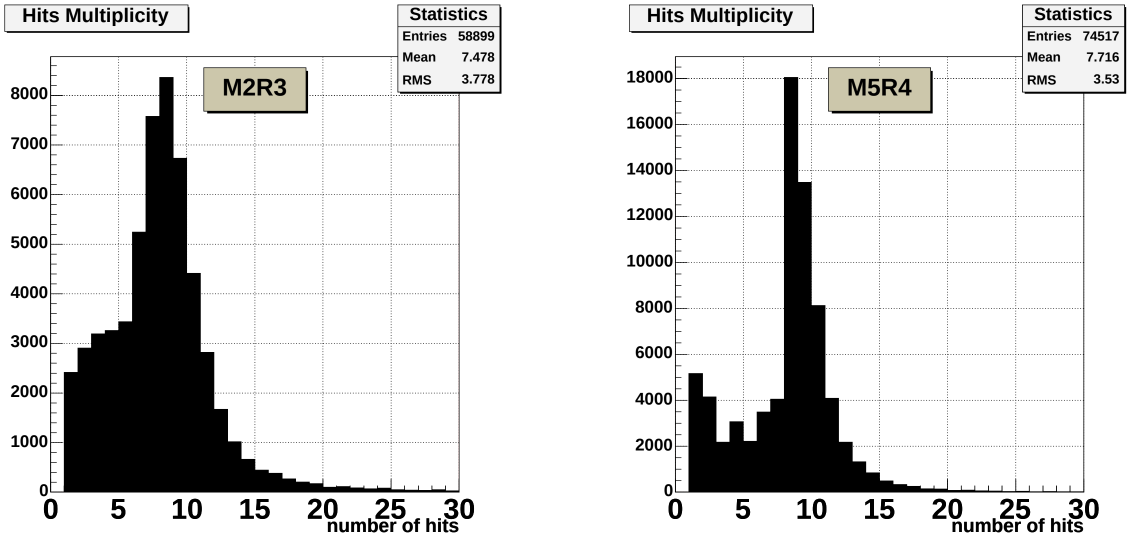

Figure 3.13: Hits multiplicity in a M2R3 chamber (left) and in a M5R4 chamber (right) once the empty events class has been removed.

In order to avoid possible incorrect hit association, we want to track with at least five layers, thus rejecting events with less than five hits. Moreover, both distributions show very few events with more than 25 hits, therefore it is not restrictive to introduce a cut that discards events with more than 25 hits. This cut allows to reject possible anomalous events due to momentary electronic noise or even to contemporary traversing particles in the event, as shown in Figure 3.14.

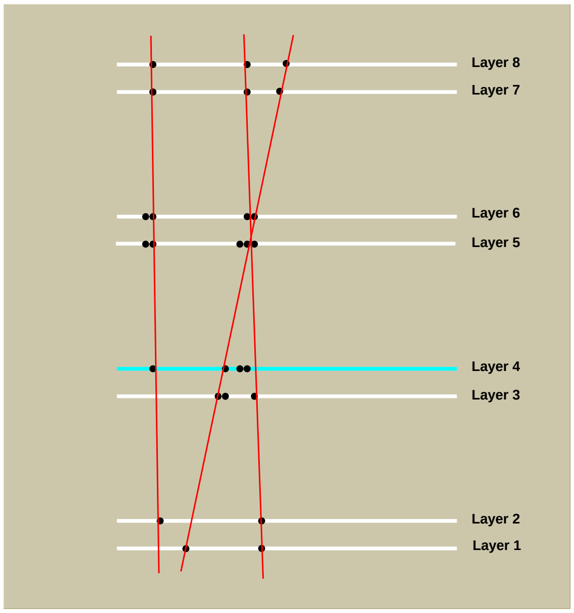

Figure 3.14: An example of an event with 26 hits that could be due to multiple traversing particles.

For this goal we set to 25 hits the maximum number of hit allowed and therefore the second step in the event selection consists in rejecting events with less than 5 hits or more than 25 hits. In Figure 3.15 is shown the event multiplicity after this second cut.

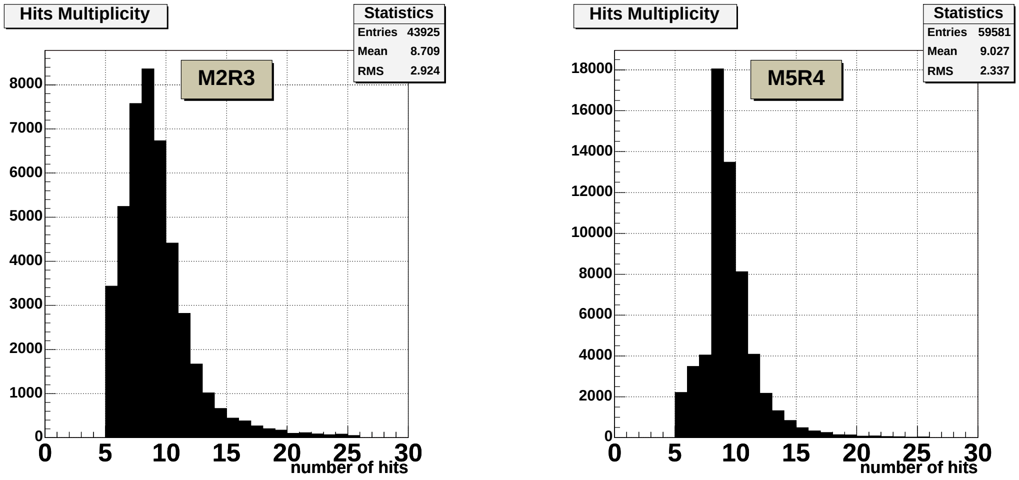

Figure 3.15: Hits multiplicity in a M2R3 chamber (left) and in a M5R4 chamber (right) after the second cut in the event selection.

The last cut we apply consists in requiring that the candidate tracks are composed by at least five layers out of seven, rejecting therefore events with hits distributed along four layers or less. This third cut lightly reduces the size of the allowed event class as shown in Figure 3.16, where the event multiplicity after this third cut is shown.

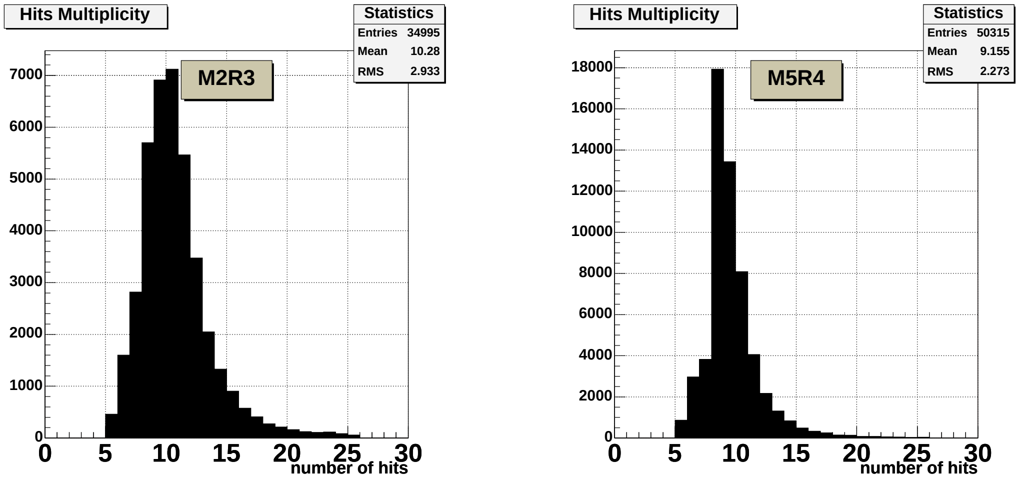

Figure 3.16: Hits multiplicity in a M2R3 chamber (left) and in a M5R4 chamber (right) after the third cut in the event selection.

After the events have been selected with these three cuts, the track finding is applied to the remaining events. In table 3.1 the event selection steps are summarized with their typical numbers. At the end of the event selection, about 45000 reconstructed tracks have been found using M5R4 chambers and about 30000 reconstructed tracks using M2R3 chambers.

Table 3.1: Typical numbers of event selection steps 1-3.

Selection steps	**M2R3**	**M4R5**
Events processed	100000	100000
Events after the 1^{st}cut	58900	74517
Events after the 2^{nd}cut	43925	59581
Events after the 3^{rd}cut	34995	50315
Selected Tracks	**29521**	**44164**

Defining the efficiency of the described tracking method as the ratio between the number of the selected tracks and the number of suitable events, we obtain an efficiency of 29521/34995 $\sim$ 84% and 44164/50315 $\sim$ 88% for the M2R3 and M5R4 chambers respectively. These numbers will be discussed in more details in the next Section.

The angular distribution of the selected tracks is shown in Figure 3.17 for an M5R4 chamber, where the angle θ is defined as the angle between the perpendicular to the chambers and the track. The angular distribution is shown with a resolution of $\Delta\theta$=5°; note that the two empty bins close to θ=0° are due to the discrete character of the system (the minimum possible angle of non-vertical tracks is $\theta_{\min}$ $\sim$18°). As expected, most of the tracks are vertical.

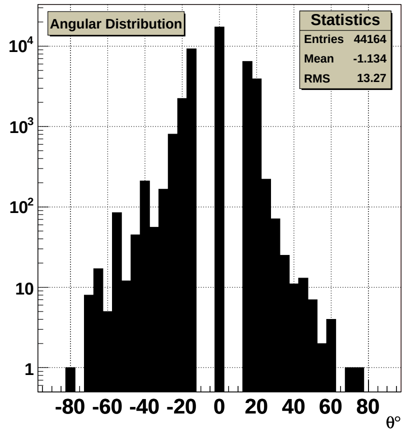

Figure 3.17: Angular distribution of the selected tracks in an M5R4 chamber.

3.5 Efficiency studies

Once the track has been reconstructed, it can be used to measure the efficiency of the layer under study. In order to be completely confident that the track has really crossed the chamber, the other layer (*partner layer*) present in the same chamber of the layer under study is checked. As shown in Figure 3.18, the track is extrapolated to both the partner layer and the layer under study; if at least one hit is found inside the FOI of the partner layer, then the efficiency of the layer under study is computed, looking for at least one hit in the crossed pad together with its right and left neighbour pads.

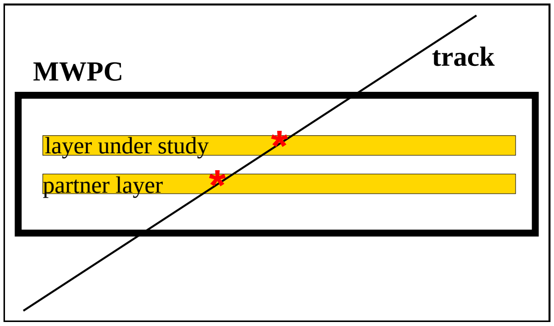

Figure 3.18: Definition of the partner layer.

This step is therefore an additional requirement (fourth cut) applied to the track finding method, because if the partner layer is not present in the reconstruction, the track is rejected. Thus, Table 3.1 has to be updated with the following one:

Table 3.2: Typical numbers of event selection steps 1-4.

Selection steps	**M2R3**	**M4R5**
Events processed	100000	100000
Events after the 1stcut	58900	74517
Events after the 2ndcut	43925	59581
Events after the 3rdcut	34995	50315
Selected Tracks	**29521**	**44164**
Tracks after the 4th cut	**25146**	**39374**

We tested four chambers at a time, for a total of 16 M2R3 chambers and 4 M5R4 chambers. All efficiencies have been computed for each single layer, i.e. each double-gap. Following the LHCb rules, we refer to them as double-gap AB (top layer) and double-gap CD (bottom layer).

3.5.1 M2R3 chambers

An efficiency profile of an M2R3 chamber is shown in Figure 3.19. As already explained in section 2.5, the M2R3 cathode plane is segmented in 48×2 cathode pads; thus, it is shown the efficiency integrated along the y (short side) direction.

The dotted red line shows the efficiency threshold required by the experiment in the 95% (i.e. 46 pads) of the chamber. The average efficiency is $<\epsilon>$=99% both in double-gap AB and double-gap CD. Both the double-gap have therefore an

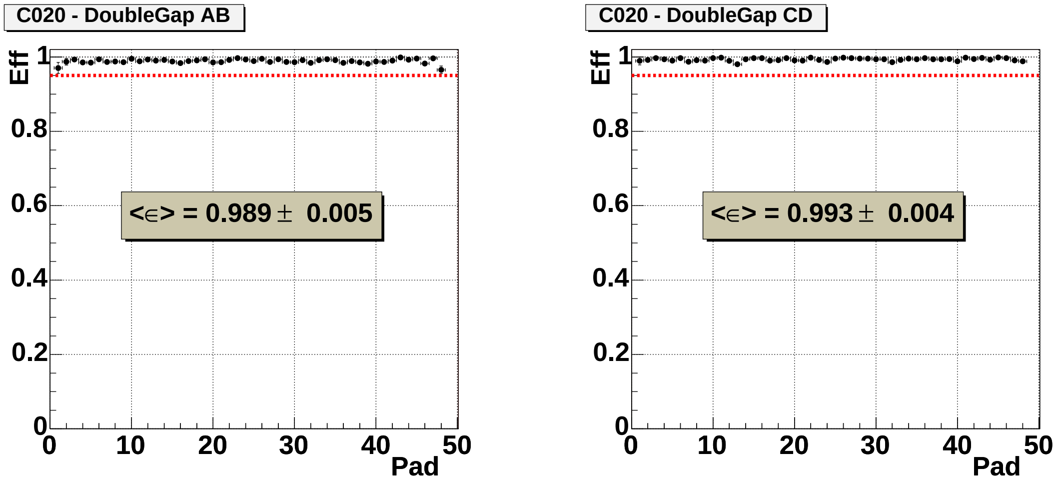

Figure 3.19: Efficiency profile of the M2R3 C020 chamber, double-gap AB (left) and double-gap CD (right).

.

efficiency well within the LHCb requirements.

The efficiency profile of another M2R3 chamber is shown in Figure 3.20.

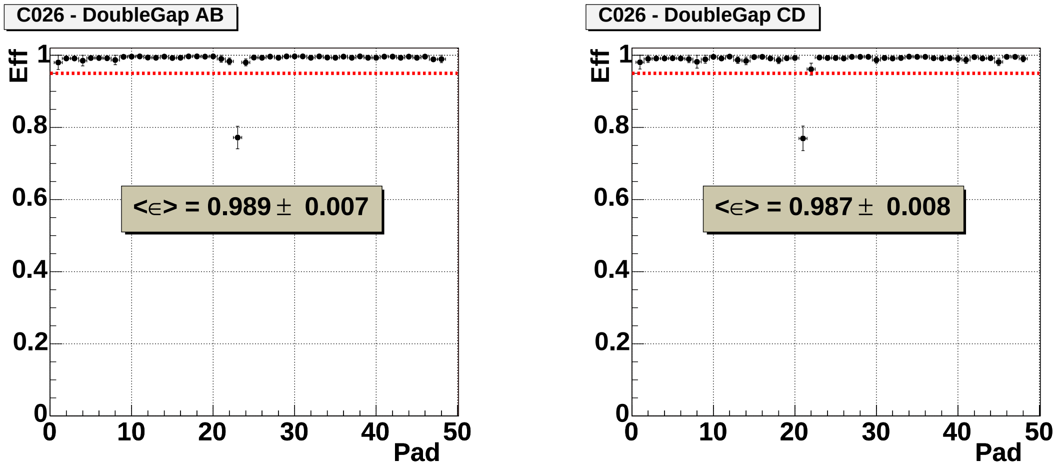

Figure 3.20: Efficiency profile of the M2R3 C026 chamber, double-gap AB (left) and double-gap CD (right).

.

In this example, both the double-gap have a quite low efficient pad ($\epsilon \sim$0.75): pad number 23 (double-gap AB) and pad number 21 (double-gap CD). In order to better understand the reason of that inefficiency, the bi-dimensional efficiency is given in Figure 3.21 for the double-gap CD.

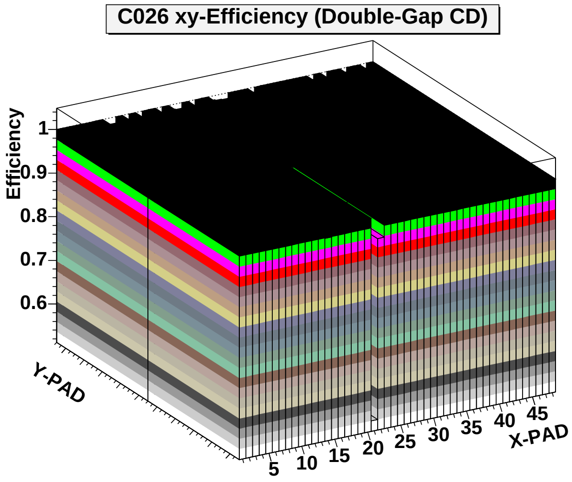

Figure 3.21: Bi-dimensional efficiency profile of the M2R3 C026 chamber, double-gap CD.

.

As shown in the above figure, just one of the two segments of pad 21 is inefficient (ϵ ~0.5), while the other has an efficiency very close to 1; the mean of this two values is exactly 0.75. Thus, the inefficent behaviour of pad 21 is not due to the chamber but instead to a not properly working electronic channel. The same conclusion can be drawn for the double-gap AB.

All the results obtained from the measurements performed on the 16 M2R3 chambers are summarized in Table 3.3. The results have been grouped following the setup of the test (four chambers each run) and the total chamber efficiency has been computed using the formula:

$$1-\epsilon_{\text{tot}}=(1-\epsilon_{AB})(1-\epsilon_{CD})$$

From the M2R3 column in Table 3.2 we can compute the efficiency of the tracking method: we have 34995 events suitable for finding tracks and 29521 reconstructed tracks. The tracking efficiency is therefore about

$$\epsilon_{\text{tracking}}=\frac{29521}{34995}\simeq 0.84 \qquad (3.2)$$

Note that the given numbers are referred to the first group of chambers in table 3.3.

We can predict this number taking into account the efficiency of each single layer. In general, if we have a tracking system composed by $\{n\}$ tracking layers and we use just $\{m\}$ of those to track, the efficiency of the system will be:

$$\epsilon_{\text{system}}=\frac{1}{\binom{n}{m}}\sum_{\forall\{m\}}\prod_{i=1}^{m}\epsilon_i$$

Table 3.3: M2R3 summary results.

Chamber	Eff. double-gap AB	Eff. double-gap CD	Total Eff.
C020	98.9%	99.3%	99.99%
C022	95.6%	97.6%	99.92%
C026	98.9%	98.7%	99.99%
C028	96.9%	98.5%	99.95%
C021	95.8%	99.1%	99.96%
C023	97.8%	95.9%	99.91%
C034	97.7%	95.8%	99.90%
C042	97.9%	96.9%	99.93%
C032	not working	81.5%	/
C037	97.9%	95.3%	99.90%
C038	95.2%	98.1%	99.91%
C040	96.8%	96.5%	99.89%
C024	95.7%	98.4%	99.93%
C029	97.8%	98.1%	99.96%
C030	98.8%	96.0%	99.95%
C036	96.7%	98.4%	99.95%

In our case, the system is composed by $n = 8$ tracking layers and, due to the requirements of the event selection, we can use $m = 5, 6$ or 7 layers to find a track. Referring, as always, to the first group of chambers in Table 3.3, we found the following fractions of events with 5,6 or 7 layers fired:

Events with 5 layers fired	f_1	2%
Events with 6 layers fired	f_2	13%
Events with 7 layers fired	f_3	85%

Thus, the efficiency of the tracking system, tacking into account the efficiencies of the 8 layers listed in Table 3.3 (first group), will be:

$$\epsilon_{\text{system}} = \frac{f1}{56} \sum_{\forall\{5\}} \prod_{i=1}^{5} \epsilon_i + \frac{f2}{28} \sum_{\forall\{6\}} \prod_{i=1}^{6} \epsilon_i + \frac{f3}{8} \sum_{\forall\{7\}} \prod_{i=1}^{7} \epsilon_i \qquad (3.3)$$

i.e.

$$\epsilon_{\text{system}} \simeq 0.87 \qquad (3.4)$$

The predicted value ϵ_{system} in Eq. 3.4 is therefore in fair agreement with the computed $\epsilon_{\text{tracking}}$ given in Eq. 3.2.

We summarized, for each group of M2R3 chambers, the comparison between the tracking efficiency and the expected system efficiency in table 3.4. From the results shown in the table we can conclude that all the expected and computed efficiencies are in good agreement between them.

Table 3.4: Comparison between the expected system efficiency and the tracking efficiency.

Groups of chambers	ϵ_{system}	$\epsilon_{\text{tracking}}$
C020-C022-C026-C028	87%	84%
C021-C023-C034-C042	82%	79%
C032-C037-C038-C040	61%	59%
C024-C029-C030-C036	84%	81%

3.5.2 M5R4 chambers

An efficiency profile of an M5R4 chamber is shown in Figure 3.22. As already explained in section 2.5, the M5R4 anode plane is segmented in 24 wire pads.

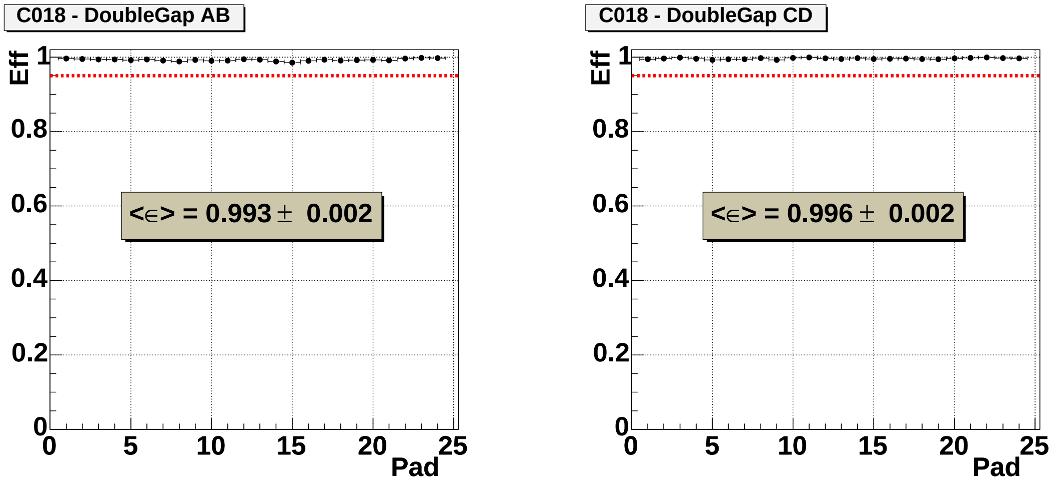

Figure 3.22: Efficiency profile of the M5R4 C018 chamber, double-gap AB (left) and double-gap CD (right).

.

The dotted red line shows the efficiency threshold required by the experiment in the 95% (i.e. 23 wire pads) of the chamber. The average efficiency is $<\epsilon>$=99% in the double-gap AB and $<\epsilon>$=100% in the double-gap CD. Both the double-gap have therefore an efficiency well within the LHCb requirements.

The efficiency profile of another M5R4 chamber is shown in Figure 3.23.

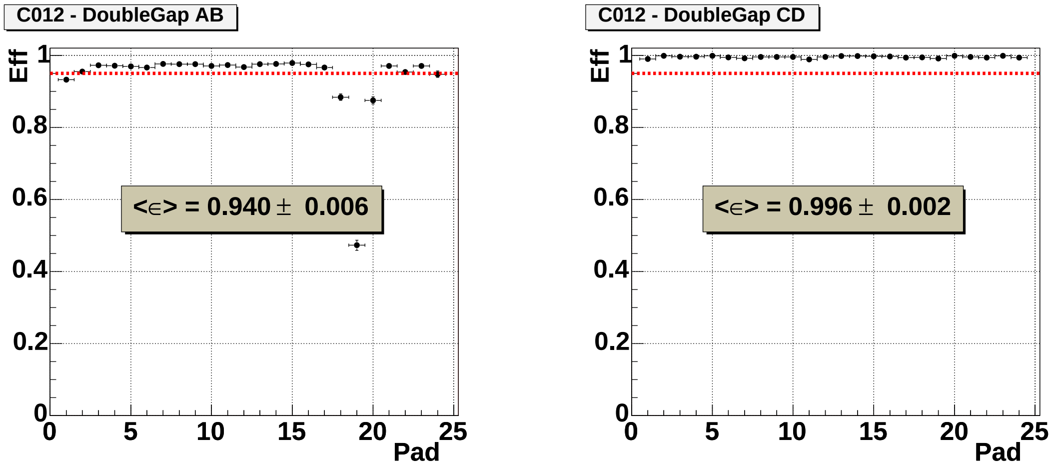

Figure 3.23: Efficiency profile of the M5R4 C012 chamber, double-gap AB (left) and double-gap CD (right).

.

In this example, the double-gap AB has a very low efficient pad (pad number 19 with $\epsilon \sim$0.45) and from the plot shown this chamber would not pass the LHCb requirements. In order to better understand the reason of this inefficiency, the electronic channel occupancy is shown in Figure 3.24.

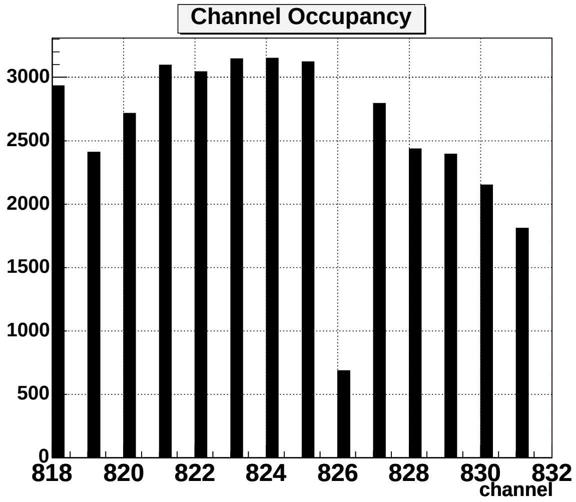

Figure 3.24: FE occupancy in the M5R4 C012 chamber, double-gap AB.

.

In the FE setup used, the channel 826 corresponded just to the wire pad 19 and thus its inefficiency is due to a not properly working electronic channel. Because of the fact that to determine the efficiency of a pad the efficiency method uses also the neighbouring pads, in Figure 3.23 pad 18 and pad 20 show a not perfectly efficient behaviour themeselves. Nevertheless, the chambers C012 has been considered well within the LHCb requirements.

The results obtained from the measurements performed on the 4 M5R4 chambers are summarized in Table 3.5, together with the total chamber efficiency.

Table 3.5: M5R4 summary results.

Chamber	**Eff. double-gap AB**	**Eff. double-gap CD**	**Total Eff.**
C012	94.0%	99.6%	99.98%
C018	99.3%	99.6%	100.00%
C019	99.4%	98.1%	99.99%
C026	99.6%	98.1%	99.99%

Using the efficiencies of each double-gap reported in the table above, we can compute the expected tracking system efficiency. As for the M2R3 chambers, the system was composed by 8 tracking layers and the tracking method looks for track using 5,6 or 7 layers. The fractions of events with m layers fired are:

Events with 5 layers fired	f_1	2%
Events with 6 layers fired	f_2	5%
Events with 7 layers fired	f_3	93%

Thus, from equation 3.3, the expected efficiency will be:

$$\epsilon_{\text{system}} \simeq 0.90 \tag{3.5}$$

On the other hand, we can compute the efficiency of the tracking method from the M5R4 column in Table 3.2: there are 50315 events suitable for finding tracks and 44164 reconstructed tracks. The tracking efficiency is therefore:

$$\epsilon_{\text{tracking}} = \frac{44164}{50315} \simeq 0.88 \tag{3.6}$$

that is in nice agreement with the expected value in Eq. 3.5.

3.6 Gas gain uniformity measurements

As already explained in Section 2.6, the LHCb collaboration has adopted a stringent procedure for the quality control test in order to guarantee the fullfilment of all the requirements needed. We saw that the gas gain uniformity mesurement is an important step of this procedure. Two of the M5R4 chambers we studied in the previous section (C012 and C019) have undergone this test in the Frascati laboratories, where the LHCb LNF group has measured their gas gain uniformity with a ^{137}Cs radioactive source (see §3.2). The results is shown in Figure 3.25. The data have been integrated along the y position and thus shown just in function of the x position. Moreover, the average current drawn by the two gaps A(C) and B(D), making up the double-gap AB(CD), is shown in the figure.

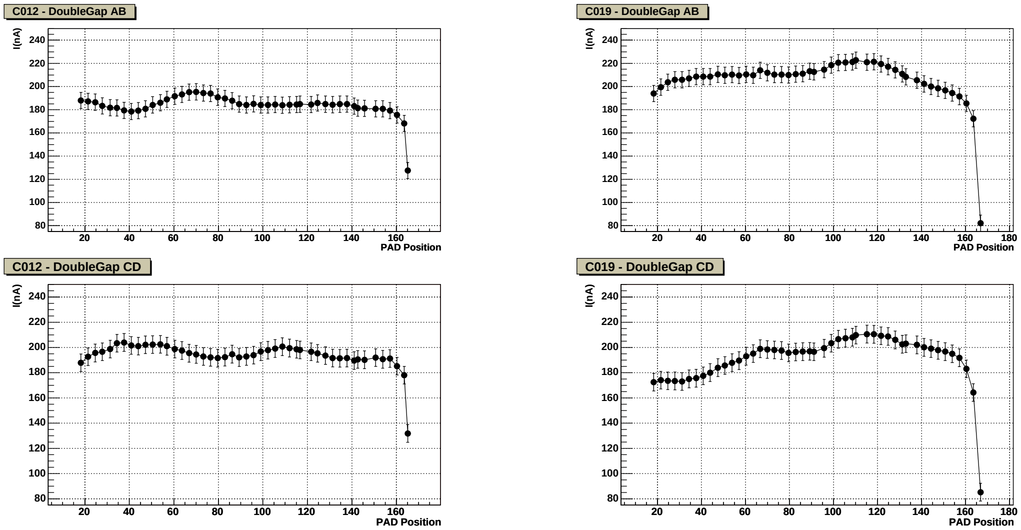

Figure 3.25: Current drawn by the M5R4 C012 chamber (left) and C019 (right) versus the x position in double-gap AB (top) and double-gap CD (bottom).

As already explained, our group has developed an alternative method to measure the gas gain uniformity by means of the cosmic rays. In the next paragraphs, the method and the measurement results will be reported.

3.6.1 The method

If we know the current I_0 drawn by an MWPC at the high voltage V_0, we can predict the current I drawn at the voltage V using the relation:

$$I(V) = I_0 \; e^{\alpha(V-V_0)}$$

where α is the Townsend coefficient and it has been experimentally measured to be $\alpha = \ln 2/106$. If the current depends also on the x position in the chamber where we measure it (e.g. because of non uniform gap width), then the previous equation becomes:

$$I[V] = I_0 \; e^{\alpha[V-V_0(x)]}$$

Defining V_{50} as the voltage at which the chamber is 50% efficient (i.e. $\epsilon(V_{50}) = 0.5$), the last equation can be translated in terms of V_{50}, because by definition the quantity $V_{50}(x) - V_0(x)$ is constant:

$$I[V] = I_0 \; e^{\alpha[V-V_{50}(x)+k]} \tag{3.7}$$

The current measurements are performed keeping the voltage V constant while the position x of the radioactive source is varied, so that the quantity $V + k = \tilde{k}$ is constant. The previous equation becomes:

$$I(x) = I_0\, e^{\alpha\left[\tilde{k} - V_{50}(x)\right]} \tag{3.8}$$

Since the gas gain is of course $G(x) = I(x)/I_0$, equation 3.8 gives the relation between the gas gain and the voltage at which the chamber is 50% efficient. Once we determine $V_{50}(x)$, we can compare the gas gain values from Eq. 3.8 with the measurements shown in Figure 3.25.

In order to measure $V_{50}(x)$, 6 dedicated runs have been performed with the cosmic rays test station. Each run is characterized by having 7 layers at the nominal high voltage (i.e. 2700 V) and the eighth layer at an high voltage varying between 2350 V and 2600 V. The goal is to determine V_{50} for each single pad of the eighth layer.

We started from 2350 V and increasing the high voltage by 50 V steps up to 2600 V, we compute the efficiency of each pad following the tracking and efficiency methods described previously. A typical result, obtained for the M5R4 chamber C019, is shown in Figure 3.26. Each coloured line corresponds to the efficiency behaviour of each pad in the range 2350-2600 volts.

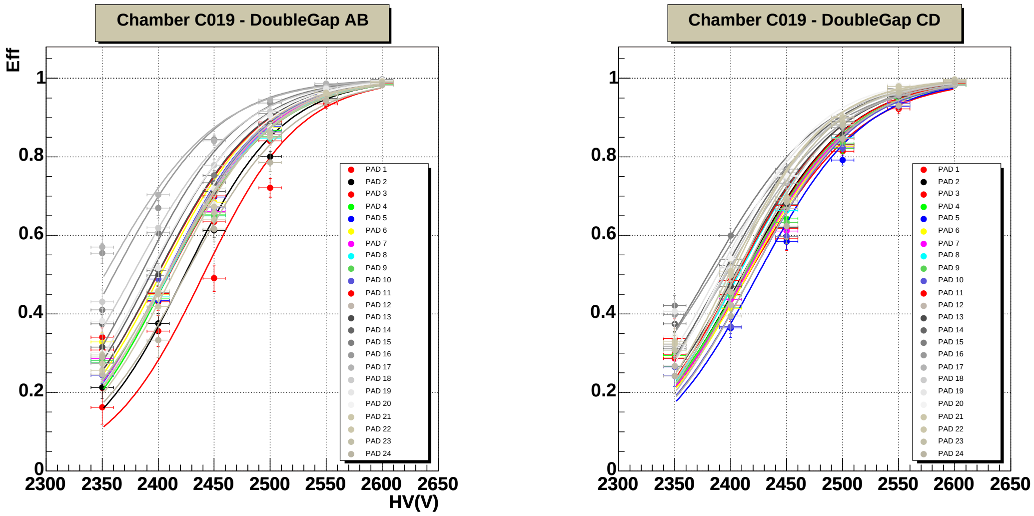

Figure 3.26: Efficiency versus the high voltage in the M5R4 C019 chamber for the double-gap AB (left) and the double-gap CD (right). The coloured lines correspond to the 24 wire pads.

To fit the experimental points we used the function:

$$\epsilon(V) = \frac{1}{2}\left(\tanh\left[a(V - \hat{V})\right] + 1\right)$$

where a and $\hat{V}$ are the fit parameters. The choice of this function is only due to the fact that, in most of cases, it well adapts to the experimental data.

3.6.2 Results

From the curves shown in Figure 3.26, we can determine the voltage at which the efficiency is equal to 0.5. The result obtained with the C019 chamber is given in Figure 3.27.

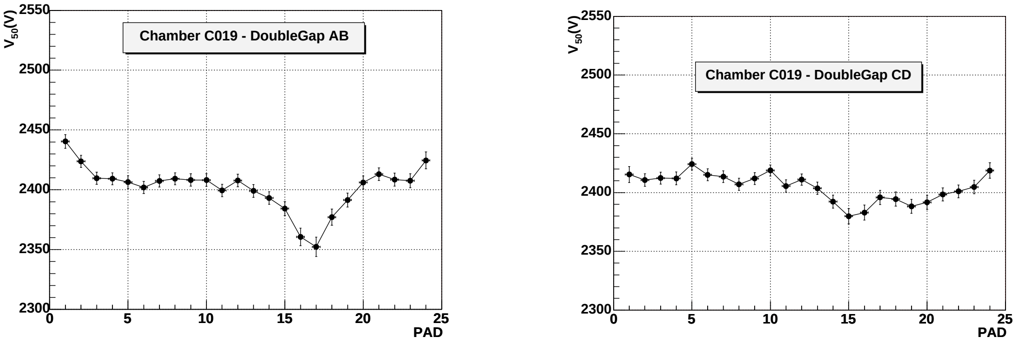

Figure 3.27: Values of V_{50} versus the PAD number in the M5R4 C019 chamber for the double-gap AB (left) and the double-gap CD (right).

Thus, we can compare the gas gain uniformity of the C012 and C019 chambers from the ratio $I(x)/I_0$ computed using the LNF current measurements and also from the equation 3.8 together with our experimental V_{50} values. The only unknown quantity is the multiplicative constant $c = e^{\alpha\tilde{k}}$ we used as a scale factor in order to compare the $G(x)$ behaviours computed in the two described ways. The result of this comparison is shown in Figure 3.28 for the C012 chamber, where the red points represent the data from the LNF test while the black points represent the result from the cosmic ray test station.

In the double-gap AB, the drop in our data corresponding to PAD 19 is the same already seen in the efficiency profile shown in Figure 3.23 and due to non properly working electronic channels. Thus, the agreement between the LNF data and our measurements seems to be rather good.

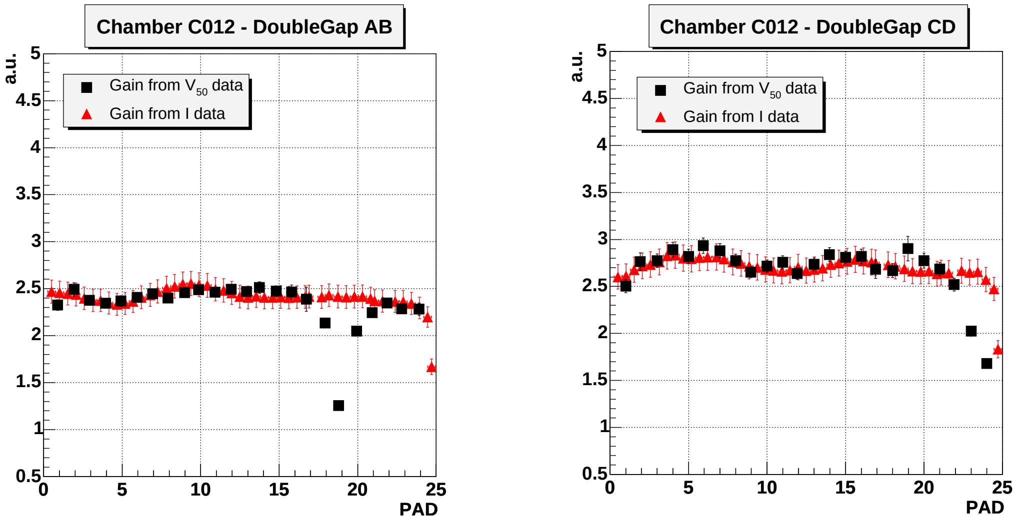

Figure 3.28: Comparison of the gas gain $G(x)$ uniformity versus the PAD number in the M5R4 C012 chamber for the double-gap AB (left) and the double-gap CD (right).

An analogous comparison has been carried out for the C019 chamber and is shown in Figure 3.29.

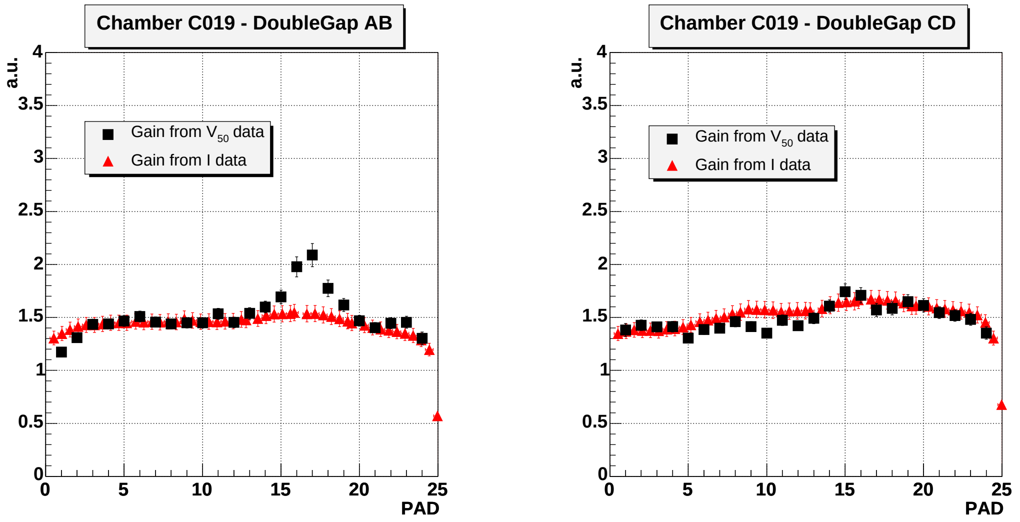

Figure 3.29: Comparison of the gas gain $G(x)$ uniformity versus the PAD number in the M5R4 C019 chamber for the double-gap AB (left) and the double-gap CD (right).

While the agreement between the LNF data and our data seems to be good in the double-gap CD, we observe a pretty bad agreement in the double-gap AB around the pad number 17. In particular, the current bump shown by the LNF data is extremely enhanced in our data.

This bump could be due to a real disuniformity in the chamber, as for example a reduced thikness of the gas gap and therefore an higher electric field, and in this case there will be no reason to explain the difference between the data from the two performed tests. Instead, if in our data the bump is actually due to a not poperly working front-end channel, then we can conclude that the difference between the two methods is not real.

In order to better understand the reason of this disagreement, we can look at the front-end channel occupancy of the double-gap AB of the chamber C019. In Figure 3.30 the channel occupancy is shown at various HV values for different runs of 100k events. In this figure, the number of the pad instead of the number of the corresponding electronic channel is shown for higher clarity. The occupancy is shown for the pads in the range 14-20.

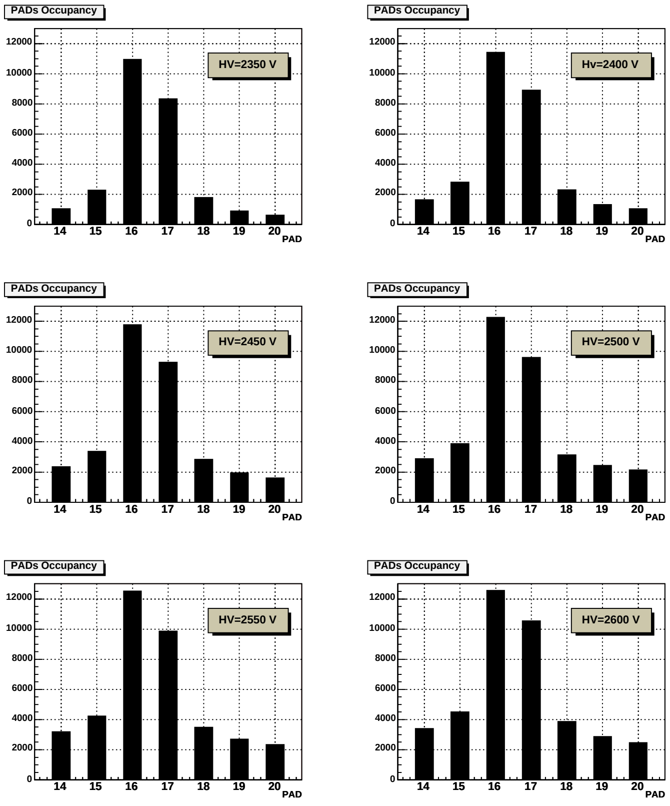

Figure 3.30: Pad occupancy distributions in the M5R4 C019 chamber double-gap AB for six different high voltages.

It is clear that the front-end channels connected to pads 16 and 17 are not properly working and there is a very high noise. For example, we had about $11{\times}10^3$ hits in the pad 16 at 2350 V against about 10^3 hits in the pad 14 at the same high voltage over 100k events. These noise hits could contribute to the efficiency for as much as 10% which therefore should be subtracted.

We can compute a *fake* efficiency of the i-pad selecting the tracks which pass trough all the rest of the layer (i.e. excluding the i-pad) and counting the number of hits in the i-pad. In order to completely disentangle the class of selected tracks from the class of i-pads hits, we require that the track passes trough the first eight pads and it is therefore very far from the noise region. The result is shown in Figure 3.31 and it is referred to chamber C019 double-gap AB at 2400 V, i.e. the voltage at which the chamber is approximately 50% efficient.

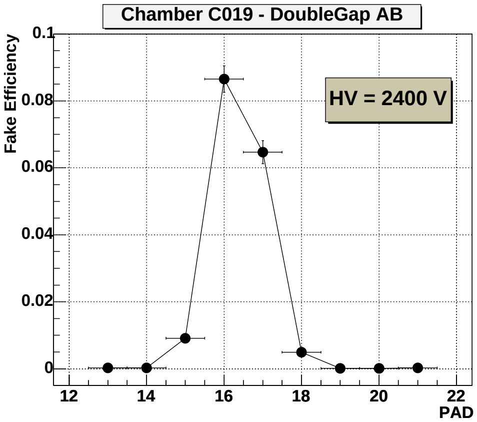

Figure 3.31: *Fake* efficiency versus pad in the M5R4 C019 chamber double-gap AB at 2400 V.

The high values of *fake* efficiency of pads 16 and 17 invalidate of course the result of the comparison shown in Figure 3.29 (left side). In order to correctly determine the V_{50} values around pad 17, we need to compute the *fake* efficiency of the pads 15-18 in the range 2350-2600 volts. The result is shown in Figure 3.32.

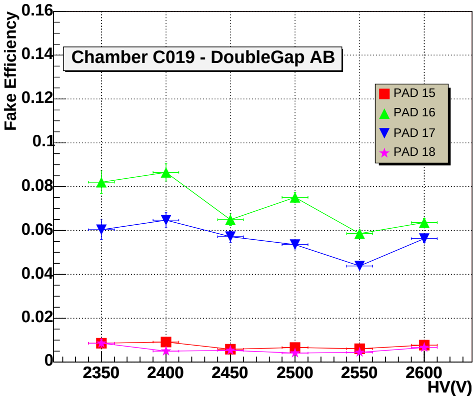

Figure 3.32: Values of the *fake* efficiency versus the high voltage for pads 15,16,17 and 18 in the M5R4 C019 chamber double-gap AB.

Thus, subtracting the *fake* efficiency values from the measured efficiencies in Figure 3.26, we can determine the new V_{50} values and then the corrected gas gain G(x). The comparison between the gas gain values obtained by the LNF current measurements and the cosmic ray test station corrected data is shown in Figure 3.33. The agreement between the two gas gain uniformity measurements is now much better.

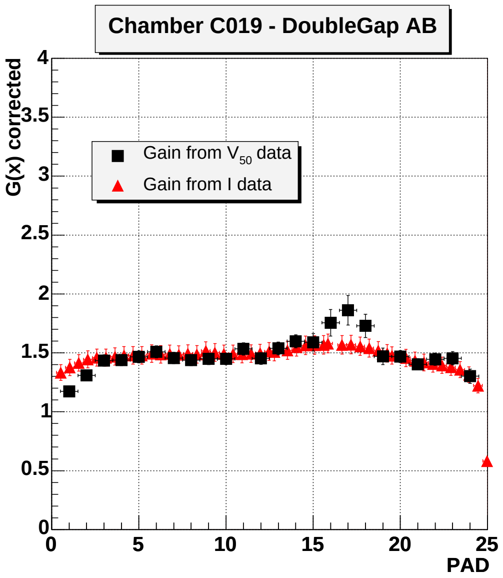

Figure 3.33: Values of the gas gain $G(x)$ versus the PAD number in the M5R4 C019 chamber for the double-gap AB (left) and the double-gap CD (right). Data obtained from the V_{50} values (blak points) have been corrected according to the *fake* efficiency values.

Although the method seems to be reliable and does not require to comply with safety regulations (absence of radioactive source), it has not been adopted by the collaboration to measure the gas gain uniformity of the produced chambers. This decision is mainly due to the fact that, because at the time of performing the measurements the final front-end electronics were not ready for the equipment of all the chambers produced, the test would have been very slow requiring the continous plugging and unplugging of the same FE electronics. For this reason the radioactive source test has been preferred.

3.7 Conclusions

In this chapter the study of the multiwire proportional chambers with the cosmic rays test station designed and developed by the Rome2 group is reported. First of all, the cosmic rays stand has been used to probe the tracking capability of the chambers with a dedicated study of the tracking with cosmics, carried out with two chamber types.

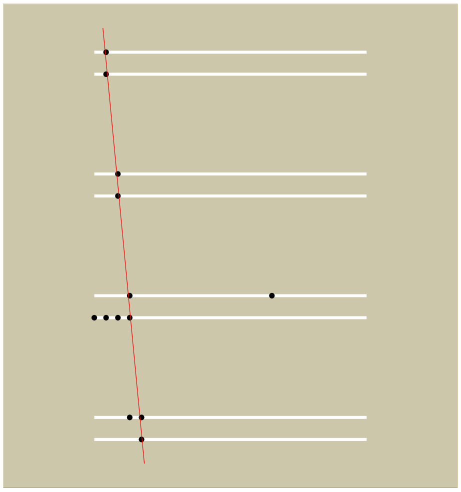

Figure 3.34: Reconstructed track in an event recorded with four M5R4 chambers.

The custom finding track algorithm, developed similarly to the experiment method, has proven to be reliable and in well agreement with what it is expected corrisponding to the tracking layers efficiency(∼80-90%). The tracks reconstruction has then been used to perform precise efficiency measurements, which have demonstrated that the MWPC produced for the Muon System will fulfil the trigger requirements(ϵ >99%).

The information collected with the cosmic rays station has also been used to measure the gas gain uniformity of the chambers. This method is alternative to the default test which instead is carried out by means of a radioactive source. The comparison of the two methods has proven that the method discussed here is reliable and does not require to comply with safety regulations (absence of radioactive source).

Part II

Physics studies

Chapter 4

Studies of the Parton Density Functions with the Z^0 boson

4.1 Introduction

The Z^0 boson is the gauge boson responsible for the weak neutral current interactions. The CERN proton-antiproton collider was proposed [47] and built to produce this particle with its charged companions W^+ and W^-. The center-of-mass energy in the $\mathrm{Sp\bar{p}S}$ collider was initially 540 GeV (630 GeV later), but because of the quark structure of the nucleon, the effective energy available in a $q\bar{q}$ collision was just adequate to produce the new particles.

Then the Z^0 characteristics were precisely measured at LEP, where e^+ and e^- beams were tuned just at the Z^0 resonance energy, to get the highest production cross-section.

When the W and Z bosons are produced they decay via the weak interaction into pairs of fermions (quarks or leptons). The number of quark decay channels is larger than the number of lepton channels but also more difficult to observe clearly because of the background from QCD processes. The experimental searches for the W and Z therefore concentrated on lepton decay channels:

$$\begin{aligned} W &\rightarrow e\nu_e, \mu\nu_\mu \\ Z &\rightarrow e^+e^-, \mu^+\mu^- \end{aligned}$$

The experimental signature for all these processes is an electron or muon with a high transverse momentum relative to the beam direction.

For the Z^0 boson, the large invariant mass of the particles provide a clear selection strategy and ensures a good efficiency in the rejection of the combinatorial background, practically negligible at such high values of p_{T} .

Even if the Z^0 detection is not included in the main LHCb B-physics program, its features make this channel very useful for calibration, alignment purposes and absolute luminosity measurement. Moreover the LHCb detector geometry, designed to cover low polar angles, turns out to be decisive in the study of peculiar proton structure functions, selecting quasi-free partons.

In this chapter the process $pp \to Z^0 \to \mu^+\mu^-$ will be studied, exploiting the capabilities of the LHCb detector. The aim of the study is to demonstrate that in spite of the limited angular acceptance and the optimization for a different kind of physics, the number of Z^0 detected at LHCb is sufficient to make profitable physics. In fact, although muons from the Z^0 decay have a very high momenta (see Figure 4.1, left side) and the LHCb spectrometer has not been optimized to measure such large p values, however the relative error on the momentum measurement is expected to be reasonably small. For example, a momentum of 750 GeV/c, corresponding to the mean value of Z^0 decaying muons distribution, is determined with a 3% error[1]. Therefore the dimuon invariant mass will be measured with good accuracy, as shown in Figure 4.1 (right side).

On the other hand, the huge energy of the Z^0 decay products does not allow to study the other lepton channel ($pp \to Z^0 \to e^+e^-$) because of the saturation in the Electromagnetic Calorimeter readout.

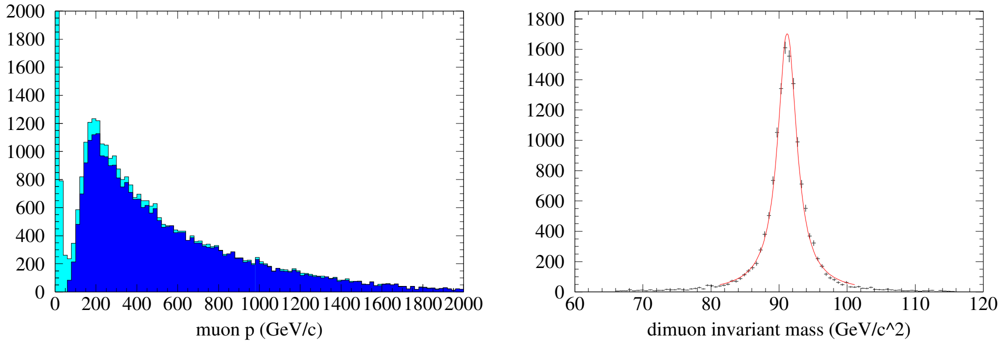

Figure 4.1: **(Left)** Momentum spectra of the reconstructed (light) and selected (dark) muons tracks. **(Right)** Invariant mass spectrum of the di-muons fitted with a Breit-Wigner function. Figures taken from [48].

The $pp \to Z^0 \to \mu^+\mu^-$ process has recently been proposed as an absolute luminosity measuring method for the LHCb experiment [48]. The studies described here will instead be focused on the LHCb capabilities to improve the knowledge of the Proton Structure Functions (PDF) at high $Q^2 \sim 10^4$ GeV^2 and very low $x \sim 10^{-4}$, i.e. in a kinematic region not probed by the present experiments.

---

[1] at LHCb, the relative error on the momentum measurement follows the relation: $\Delta p/p = 3.6 \times 10^{-5}\ \mathrm{GeV/c}^{-1}\ p$

4.2 Hadronic production of the Z^0 boson

The first successful description of massive lepton pair production in the context of the parton model was given by S.D. Drell and T.M. Yan [49] in 1970 and it is schematized in Figure 4.2.

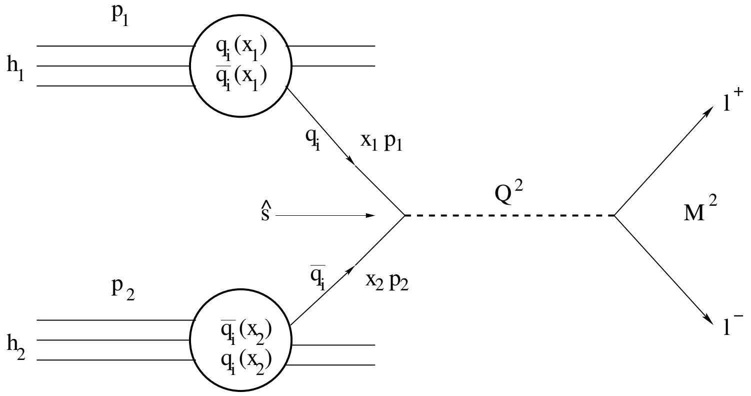

Figure 4.2: The Drell-Yan process in the context of the parton model.

The first experiment to study this reaction was carried out by the Columbia-BNL group [50] during the same years. From that time onwards this process attracted the attention of many experimentalists as well as theorists in elementary particle physics, leading to the discovery of the J/ψ meson and then of the Υ meson.

When the Drell-Yan reaction takes place at relatively low energies ($\sqrt{s} < 20$ GeV), the hadrons are probed by a highly virtual timelike photon which is experimentally observed through its decay into a massive lepton pair. Therefore this process is complementary to deep inelastic lepton-proton scattering where the exchanged photon is spacelike. The reaction belongs to the class of hard processes which means that at increasing energies all kinematical variables get large while their ratios stay fixed. In such a case one can apply the methods of perturbative QCD, which therefore in the following years supplemented the Drell-Yan mechanism.

At sufficiently high energies, the process can be described by the Standard Model and a real Z^0 can be produced. Thus, by means of the Standard Model and in particular of the QCD theory, the Z^0 production cross section at first order of approximation can be written as [51]:

$$\sigma(p_A p_B \to Z^0 X) = \frac{1}{3}\sum_{q,\bar{q}} \int_0^1 dx_1 \int_0^1 dx_2 \left[f_A^q(x_1) f_B^{\bar{q}}(x_2) + f_A^{\bar{q}}(x_1) f_B^q(x_2)\right] \hat{\sigma} \qquad (4.1)$$

where $\hat{\sigma}$ is the partonic cross section:

$$\begin{aligned} \hat{\sigma} &= R(q\bar{q} \to Z^0)\ \delta(x_1 x_2 s - M_Z^2) \ = \\ &= \frac{\pi^2 \alpha}{\sin^2\theta_W}\left(\frac{C_V^2 + C_A^2}{\cos^2\theta_W}\right)\delta(x_1 x_2 s - M_Z^2) \end{aligned}$$

The factor 1/3 accounts for the fact that all three colors of q and $\bar{q}$ occur with equal probability, but only a q and $\bar{q}$ of the same color can annihilate to form a colorless boson.

The $f^q_{\mathrm{A(B)}}(x)$ represents the distribution function of the parton q inside the proton A(B), which must be known at different values of fractional momenta x, in order to evaluate the integral. The parton distribution functions $f_i(x, Q^2)$ parametrize the probability to find a parton i with a fraction x of the beam energy ($x = p_{parton}/E_{beam}$) when the beam particle is probed by a hard scattering at the scale Q^2:

$$\sigma = \int dx_1 dx_2 f_1(x_1, Q^2) f_2(x_2, Q^2)\, \hat{\sigma} \tag{4.2}$$

The relevant types of partons in the case of the proton are both the valence and sea quarks (or antiquarks) and the gluons. Many different sets of parton distribution functions exists in literature for the proton [52]. These have been determined from experimental observables in lepton-hadron deep inelastic scattering (from fixed target and experiments at the DESY ep collider HERA) and Drell-Yan lepton pair production processes at hadron colliders [53, 54]. These results, obtained at different Q^2, have then to be extrapolated at the relevant Q^2 scale of the studied process. An example of proton structure functions taken by the CTEQ5M data set [55] is shown in Figure 4.3.

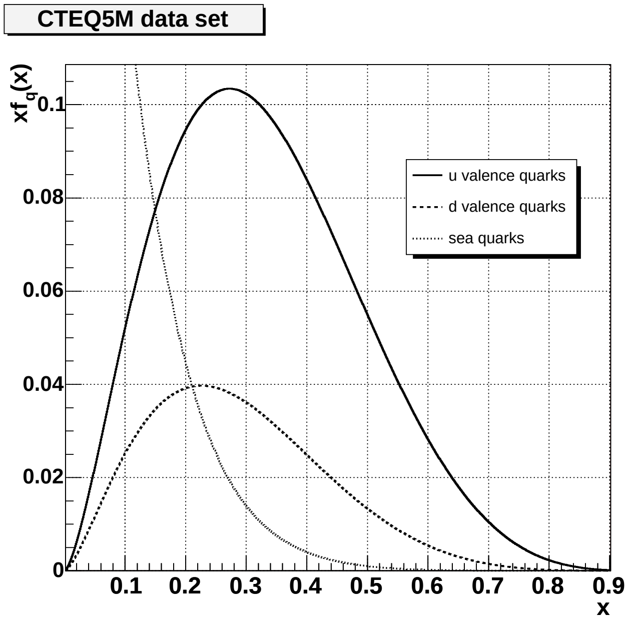

Figure 4.3: Momentum-weighted proton structure functions for *up* and *down* valence quarks and for sea quarks-antiquarks, plotted against the fractional momentum x for a fixed $Q^2 = M_Z^2$. The data set is CTEQ5M [55].

Figure 4.3 shows the momentum-weighted combination $xf_i(x, Q^2)$, for which the normalization condition $\sum_i \int dx x f_i(x, Q^2) = 1$ normally applies, drawn for up and $down$ valence quarks and for sea quarks, as a function of x at $Q^2 = M_Z^2$.

Between 1978 and 1980 the first order α_s corrections to the Z^0 production cross section were computed by many groups. The first-order correction (NLO) to the $q\bar{q} \rightarrow$ Z^0 process receives contribution from virtual (Figure 4.4) as well as real (Figure 4.5) gluon graphs [56].

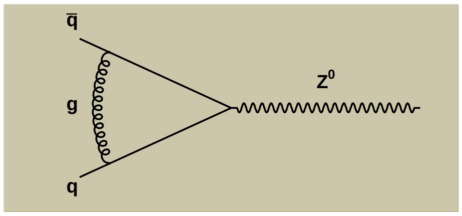

Figure 4.4: The one-loop correction to the process $q + \bar{q}$ →Z^0 .

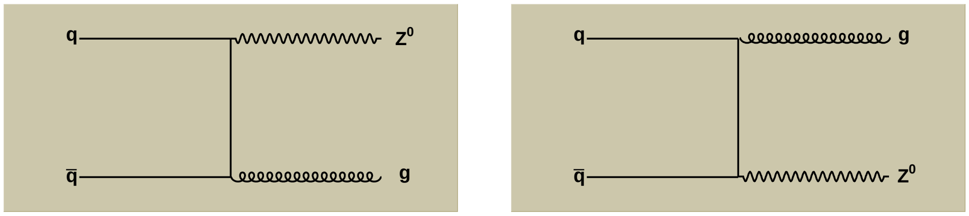

Figure 4.5: Diagrams contributing to the subprocess $q + \bar{q} \rightarrow$ Z^0 $+g$. The graphs corresponding to the subprocess $q(\bar{q}) + g \rightarrow$ Z^0 $+q(\bar{q})$ can be obtained from those presented in this figure via crossing.

In the second order of α_s (NNLO) the set of possible parton-parton reactions is completed by the qq and gg subprocesses. A complete review of all the possible NNLO diagrams is summarized in Appendix A.

Adding all the contributions, the Z^0 production cross sections has been computed at the NNLO in QCD perturbation theory. The input electroweak parameters (i.e Z^0 mass, weak couplings, etc.) are known to high accuracy and also the complete QED $\mathcal{O}(\alpha)$ electroweak radiative corrections are known [57]. In the next paragraph, the uncertainties relative to the NNLO calculations and to the input PDFs will be discussed and it will be shown that, theoretically, the main uncertainty derives from the particular choice of the PDF set used. Moreover, it will be shown that the study of the Z^0 $\rightarrow \mu^+\mu^-$ channel allow to improve the knowledge of the structure of the proton.

4.2.1 Effect of the PDFs on the production cross section

The production cross section of Z^0 boson has been measured at different energies by various experiment with increasing accuracy, as shown in Figure 4.6. The latest result has been obtained at the Tevatron Collider, the proton-antiproton machine with $\sqrt{s}$ = 1.96 TeV, by the CDF experiment. The result for the Z$^0 \rightarrow \mu^+\mu^-$ cross sections is $\sigma_Z B(Z \rightarrow \mu\mu)$ = 248.0 ± 5.9(stat.)± 7.6(syst.) ± 14.8(lum.) pb [58]. The measurement is in good agreement with the NNLO QCD calculation [56, 59, 60] which predicted a value of 251.3±5.0 pb with the MRST parton distribution functions as input. All the values already include the branching ratio for the $\mu\mu$ decay mode, which is (3.366 ± 0.007)% [61].

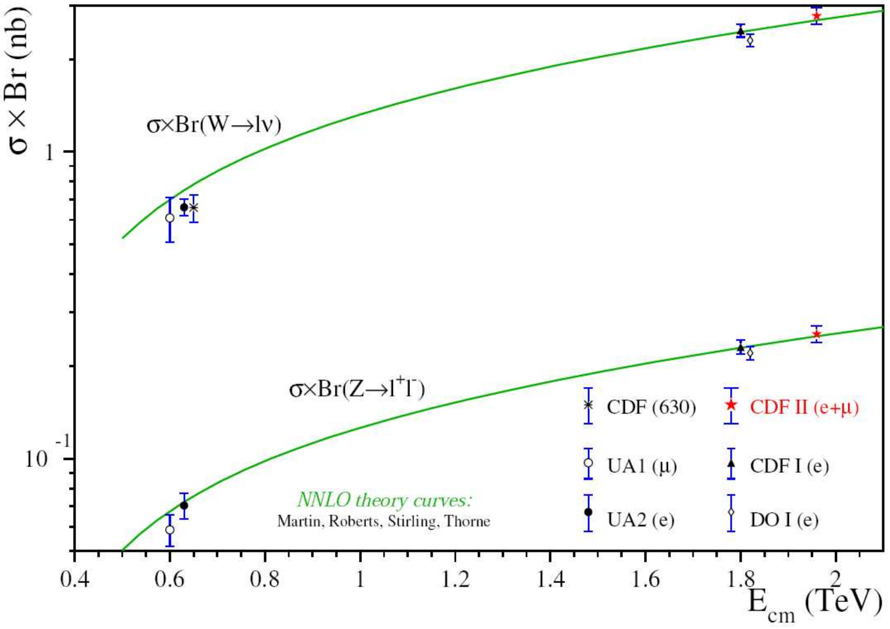

Figure 4.6: $W \rightarrow l\nu$ and $Z \rightarrow ll$ cross section measurements as a function of the $p\bar{p}$ center-of mass E_{cm}. The solid lines correspond to the NNLO Standard Model calculations.

The uncertainty on the Z^0 cross section prediction at the Tevatron energy, due to the choice of the input PDF set, is shown in Figure 4.7, where the Z^0 production cross section has been computed with different PDF sets. The various sets are labelled following the statements reported in table 4.2.1. From Figure 4.7 we can conclude that the error relative to the input PDFs could, conservatively, be as large as ± 5%. However, the present experimental error is still larger than the uncertainty in the theoretical prediction and therefore it does not allow to clearly identify the correct theoretical description of the proton structure.

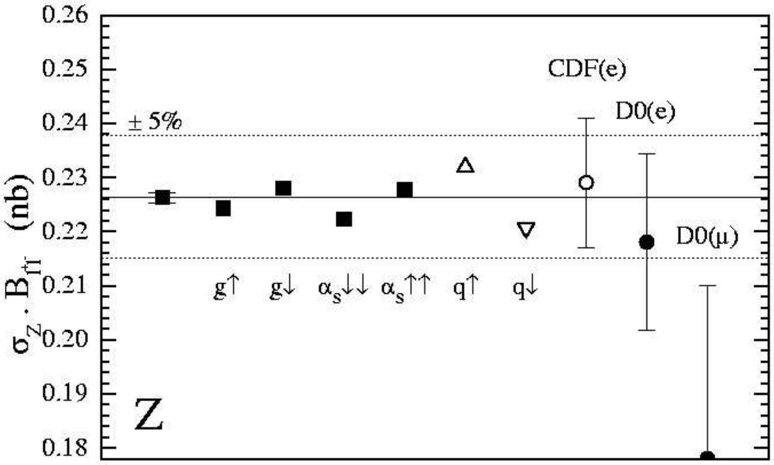

Figure 4.7: The predictions of the cross-section for Z^0 production and leptonic decay at Tevatron ($\sqrt{s}$=1.8 TeV) obtained using various NNLO sets from MRST99 [64].

Set	α_s (M_Z^2)	Description
MRST c-g	0.1175	default set
MRST $g\uparrow(\downarrow)$	0.1175	larger (smaller) gluon at large x
MRST $\alpha_s\uparrow\uparrow(\downarrow\downarrow)$	0.1225 (0.1125)	larger (smaller) α_s
MRST $q\uparrow(\downarrow)$	0.1178	larger (smaller) quarks at large x
MRST $s\uparrow(\downarrow)$	0.1175	larger (smaller) strange quarks
MRST $c\uparrow(\downarrow)$	0.1175	larger (smaller) charm quarks

Table 4.1: The various MRST99 PDF sets used.

Recently a NNLO estimation of the Z^0 and W production cross sections has been done for the LHC energy of 14 TeV as well [62]. At such a higher energy the cross section is foreseen to be almost an order of magnitude larger (see Figure 4.8), as high as:

$$\sigma(\mathrm{Z}^0)\cdot B(\mathrm{Z}^0\to\mu\mu)=(1.86\pm0.07)\ \mathrm{nb} \tag{4.3}$$

From Figure 4.8 we see that the LO →NLO→NNLO covergence of the predictions for $\sigma_{W,Z}$ is good. The jump from σ_{LO} to σ_{NLO} is mainly due to the well-known large $\mathcal{O}(\alpha_s)$ double logarithmic correction arising from soft-gluon emission. The final result has an error band, accounting for uncertainties in some deep inelastic coefficient function and in $\alpha_s(M_Z^2)$, of about 1%, which represents the uncertainty relative to the QCD NNLO calculations.

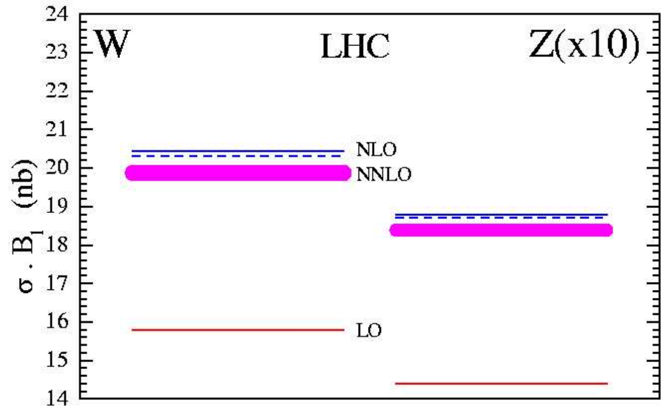

Figure 4.8: The prediction of the cross-sections for W and Z^0 production and leptonic decay at LHC obtained from global analysis of the same data set MRST00 [63]. The band of the NNLO predictions takes into account the ambiguity in the corresponding splitting functions [60].

In Figure 4.9 the effect of the uncertainties relative to the input of the quark density functions (PDF) on the Z^0 cross section predictions at the LHC energy is shown: the values of $\sigma_Z \times B(Z^0 \rightarrow \mu^+\mu^-)$ for different MRST PDF sets have been reported. As at the Tevatron energy, the error relative to the input PDFs is as large as ± 5%, therefore quite larger than the error due to the NNLO calculations.

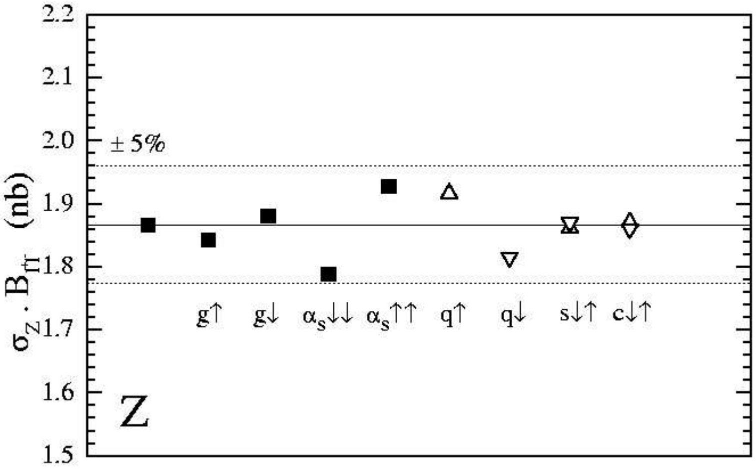

Figure 4.9: The predictions of the cross-section for Z^0 production and leptonic decay at LHC obtained using various NNLO sets from MRST99 [64].

In the recent past, new PDF data sets have been developed and used to predict the vector bosons cross section at 14 TeV; for example, we can add to the previous figure the total cross section predictions using the latest CTEQ [55] parton distributions. Since these are obtained in a similar way to the MRST partons, we would expect the predictions to lie well within the MRST99±5% band. But this is not the case: Figure 4.10 shows the CTEQ5M and CTEQ5HQ predictions compared to those of the various MRST99 sets.

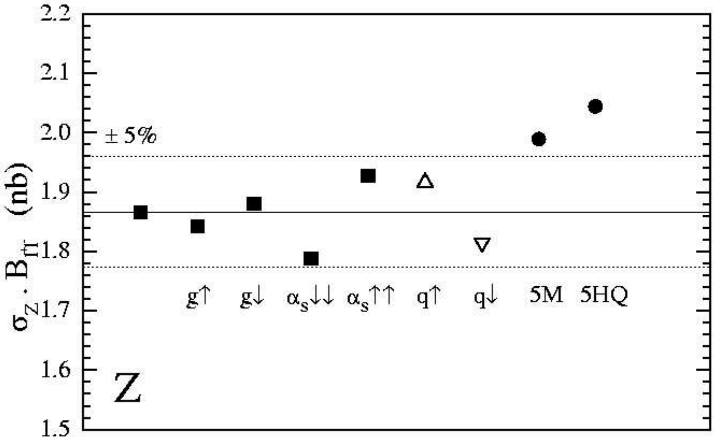

Figure 4.10: Predictions for Z^0 production cross sections times leptonic branching ratios in pp collision at 14 TeV using the MRST99, CTEQ5M and CTEQ5HQ parton sets. The 5M and 5HQ CTEQ sets differ in the treatment of the heavvy quark distributions.

The CTEQ5M predictions are about 7% larger at LHC than those of MRST99 and the CTEQ5HQ predictions are even larger, lying well outside the ±5% band. Note that, from the point of view of the theroretical assumptions and fitting procedures, the 5HQ distribution is the most comparable to the MRST treatment.

The differences between the MRST99 and CTEQ5 cross section predictions can be interpretated as corresponding differences in the underlying quark distributions. These differences are illustrated in Figure 4.11, which shows the ratio of CTEQ5HQ and MRST99(c-g) partons at $Q^2 = M_Z^2$.

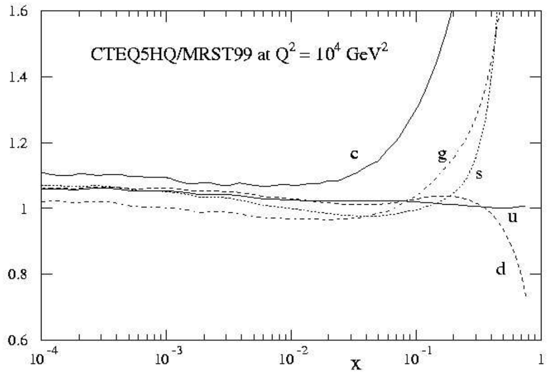

Figure 4.11: Ratio of the partons of the CTEQ5HQ set to those of the default MRST99 at $Q^2 = 10^4$ GeV^2.

The most striking difference is in the gluon at large x. Since the sea quark PDFs are driven by the $g \rightarrow q\bar{q}$ process, the same behaviour is seen in the ratio of the strange and charm distributions.

These differences have a large effect on the cross section predictions. At high energies, in fact, the contribution to the Z^0 cross section of the $q\bar{q}$ annihilation strongly depends on the flavour content of the q pairs: in particular, we have $u\bar{u} \simeq d\bar{d} >> s\bar{s} >> c\bar{c} >> b\bar{b}$, in line with the ordering of the parton distributions at the relevant x and Q^2 values. Thus, if we consider the parton flavour decomposition of σ_Z in $p\bar{p}$ and pp processes (i.e. at Tevatron and at LHC), we obtain the result illustrated in Figure 4.12.

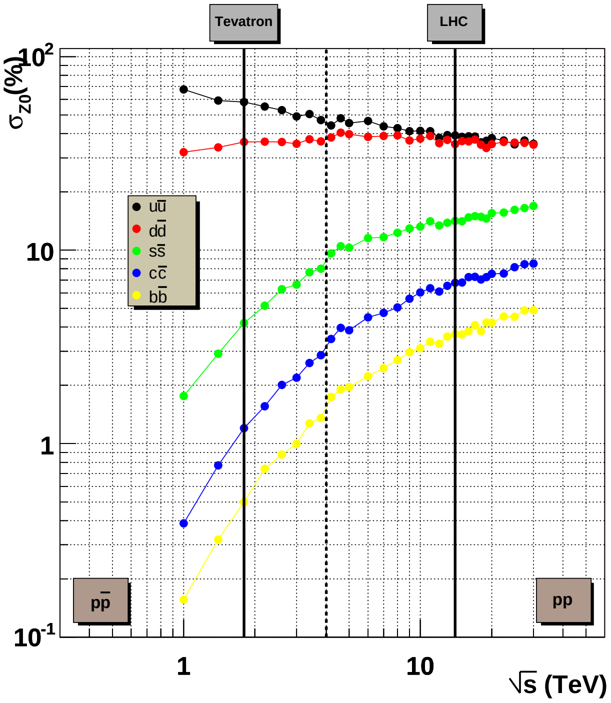

Figure 4.12: Parton decomposition of the Z^0 total cross section in $p\bar{p}$ and pp collisions. Individual contributions are shown as a percentage of the total cross section. The data set is MRST99, the standard PYTHIA generator input.

Since the Z^0 cross section is dominated by the leading order $q\bar{q} \rightarrow Z^0$ processes, just the relative contributions of these to the total have been considered. From the figure we see that, at the LHC energies of 14 TeV, about the 80% of the Z^0 cross section is due to the annihilation of quarks u and d. From Figure 4.11, we see that at $Q^2 = 10^4$ GeV^2 the CTEQ5HQ u and d quarks are between 2% (at $x \sim 0.1$) and 5% (at $x \sim 0.0001$) larger than those of MRST99 at small x. As consequence, the Z^0 cross section predictions have the large uncertainties shown in Figure 4.10.

4.3 The LHCb capabilities

In the previous section we have seen how important is the quark densities contribution to the Z^0 production cross section.

While the x distributions of the valence quarks are now quite well constrained, uncertainties for the x distributions of sea quarks, sea antiquarks and gluons remain important. As a consequence of these structure functions uncertainties, total cross sections predictions of Z^0 boson production at 14 TeV pp collisions (LHC) are much less accurate than the perturbative QCD calculation would allow.

Therefore, assuming the parton cross section $\hat{\sigma}$ known with good accuracy, a precise measure of the Z^0 production cross section would allow, from Eq. (4.2), to determine the parton distribution functions $f(x, Q^2)$ at $Q^2 = M_Z^2$ for different x. Since at LHC, in contrast to proton-antiproton colliders (e.g. Tevatron), the antiquarks entering the process must come from the sea, there is the possibility to highly improve the accuracy of the sea quarks distribution functions.

The designed LHCb geometry allows to determine the parton distribution functions in a unexplored (x, Q^2) region. If p_A and p_B are the momenta of the two incoming beam protons in their center-of-mass frame, each with energy E_{beam}, the total squared center-of-mass energy is $s = 4E_{beam}^2$. Thus, the two partons $q\bar{q}$ (as well as qg) that enter the hard interaction carry fractions x_1 and x_2 of the total beam momentum, i.e. they have four-momenta:

$$\begin{aligned} p_1 &= E_{beam}(x_1; 0, 0, x_1) \\ p_2 &= E_{beam}(x_2; 0, 0, -x_2) \end{aligned}$$

The squared invariant mass of the two partons is defined as:

$$\hat{s} = (p_1 + p_2)^2 = x_1\, x_2\, s$$

Instead of x_1 and x_2 it is often customary to use the related variables τ and y:

$$\begin{aligned} \tau &= x_1\, x_2 = \frac{\hat{s}}{s} \\ y &= \frac{1}{2}\ln\frac{x_1}{x_2} \end{aligned}$$

the first relation thus fixes the product of $x_1\, x_2$ at LHC ($\sqrt{s} = 14$ TeV) to $\tau \approx 4 \times 10^{-5}$. It is effortless to demonstrate that the variable y is the rapidity of the Z^0 boson, so that the single fractional momenta of the quarks and antiquarks are directly related to the rapidity distribution of the weak boson:

$$x_1 = \sqrt{\frac{M_Z^2}{s}}\, e^{y} \qquad x_2 = \sqrt{\frac{M_Z^2}{s}}\, e^{-y} \tag{4.4}$$

For momenta much larger than the Z^0 mass ($p \gg M_Z$), y can be safely approximated by the pseudorapidity

$$y \approx \eta = -\ln\tan(\theta/2)$$

As a consequence the x distributions of the partons can be argued from the observable pseudorapidity distributions of the muons from the Z^0 decay.

As a result of the forwardness of LHCb, low polar angle and high pseudorapidity particles are selected. This means that the parton coming downstream the detector carries almost the whole amount of momentum, while the parton coming upstream the detector is essentially at rest (Fig. 4.13).

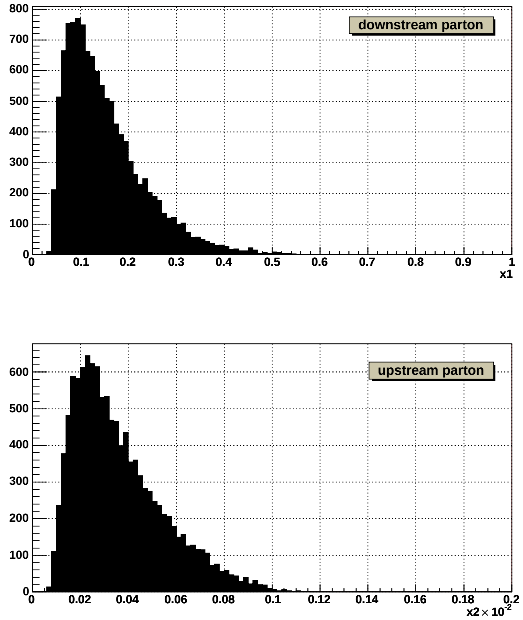

Figure 4.13: Fractional momentum distributions of the downstream parton (top) and upstream parton (bottom). Note the different scales.

LHCb will have therefore a great potential to study the parton distribution function at high $Q^2 = M_Z^2 \sim 10^4$ GeV^2 and very low $x \sim 10^{-4}$, in a kinematic region not probed by the present experiments, as results from Figure 4.14. LHCb will be able to confirm the Tevatron and Hera data at high Q^2 values reducing the statistical error and to extend the measurements to a very low x region.

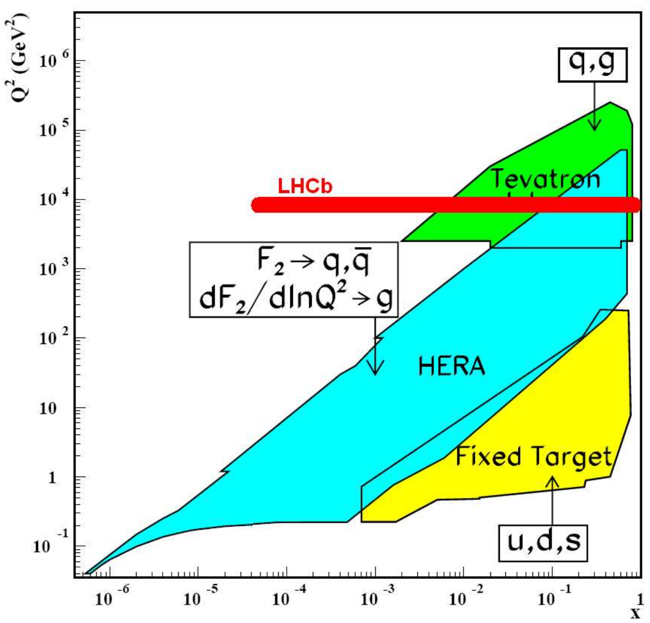

Figure 4.14: Kinematic domains in x and Q^2 probed by fixed-target and collider experiments, shown together with the important constraints they make on the various parton distributions. At $Q^2 = M_Z^2$, LHCb will be able to explore the red region.

4.4 Event characteristics

As we have seen in §4.2.1, the differences between the cross section predictions made with different PDF sets are due to corresponding differences in the underlying quark distributions. This means that, if we assume the absolute luminosity known with high accuracy, will be able to perform a precise measurement of the Z^0 boson production cross section and therefore to use its high cross section sensitivity to the various PDF sets in order to distinguish between them.

But the Z^0 cross section predictions shown in Figure 4.10 have been computed in the full solid angle, while, as we previously explained, the LHCb detector is a forward spectrometer covering polar angles in the range 20-300 mrad.

Thus, it is a fundamental point to understand what is the effect of the LHCb acceptance on the cross section sensitivity to the parton distribution functions. In this section a detailed study of this effect will be presented with two different event generators, PYTHIA and MC@NLO.

4.4.1 PYTHIA event generator

The proton-proton interactions have been generated using PYTHIA 6.2 [66], the standard event generator in high-energy physics, continuously tuned to reproduce the latest experimental results.

All the tree level processes described in §4.2 have been included in the simulation of the Z^0 production, with the exception of the self-energy graph (Figure 4.4). In fact, the normal PYTHIA event generator machinery does not contain any full higher-order matrix element, with loop contribution included.

Despite that, there are several cases where higher-order matrix elements are included at the Born level, as in the case of the $q\bar{q} \rightarrow Z^0$ process: PYTHIA also contains the two first-order processes $qg \rightarrow Z^0 q$ and $q\bar{q} \rightarrow Z^0 g$. But the cross sections for these processes are divergent when the transverse momentum becomes very low ($p_{\mathrm{T}} \rightarrow 0$). In this region a correct treatment would therefore have to take into account loop corrections, which are not available in PYTHIA: all the cross sections have therefore to be intended at the leading order.

100k Z^0 events have been generated using the MRST99(c-g) PDF set and 100k events using the CTEQ 5M PDF set. A simplified LHCb geometry has been considered, taking into account the M2 station dimensions and its distance from the interaction point, in order to simulate the detector acceptance. Being interested only in real Z^0 bosons, the Z^0/γ^* interference structure has been not considered, just including the Z^0 matrix elements, so that only *on mass-shell* Z^0 have been generated. Since, in the present context, the decay channel $Z^0 \rightarrow \mu^+\mu^-$ is the only channel of interest, the Z^0 has been forced to decay to $\mu^+\mu^-$.

In Figure 4.15 the Z^0 momentum spectrum is shown for both the parton distribution functions: the dark distributions represents the momentum spectrum of all the Z^0 generated (full solid angle), while the yellow distribution represents the momentum spectrum of the Z^0 which decay in two muons in the LHCb acceptance and they will be referred to as *selected*.

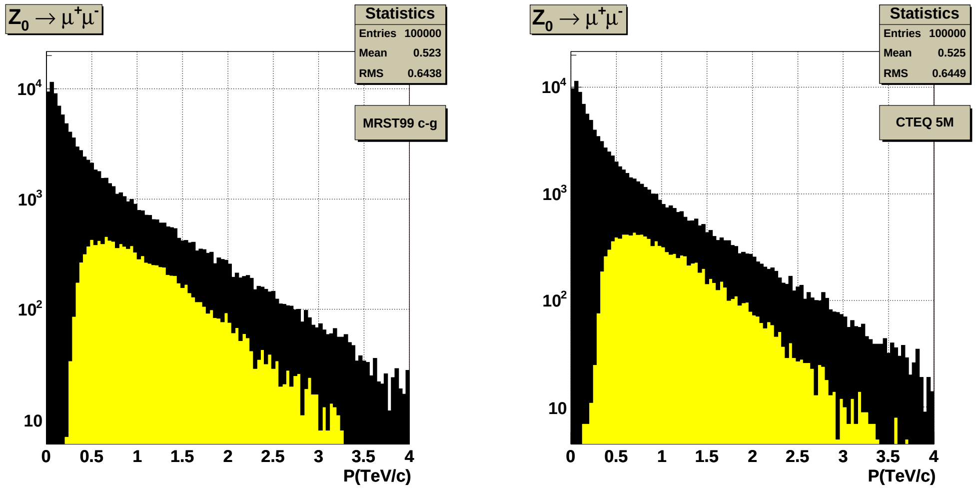

Figure 4.15: Momentum spectrum of the generated (black) and selected (yellow) Z^0 boson. Distributions on the left have been obtained using the MRST99(c-g) PDF set, while distributions on the right have been obtained using the CTEQ 5M PDF set.

Note how, when the acceptance cut is applied on this quantity, only particles with more than 250 GeV/c momenta are selected. The figure also shows how the Z^0 momentum distribution are not affected by the particular choice of the used parton distribution function at all.

Also the transverse momentum spectrum (Figure 4.16) and the polar angle θ distribution (Figure 4.17) are not affected by the particolar choice of the PDF set.

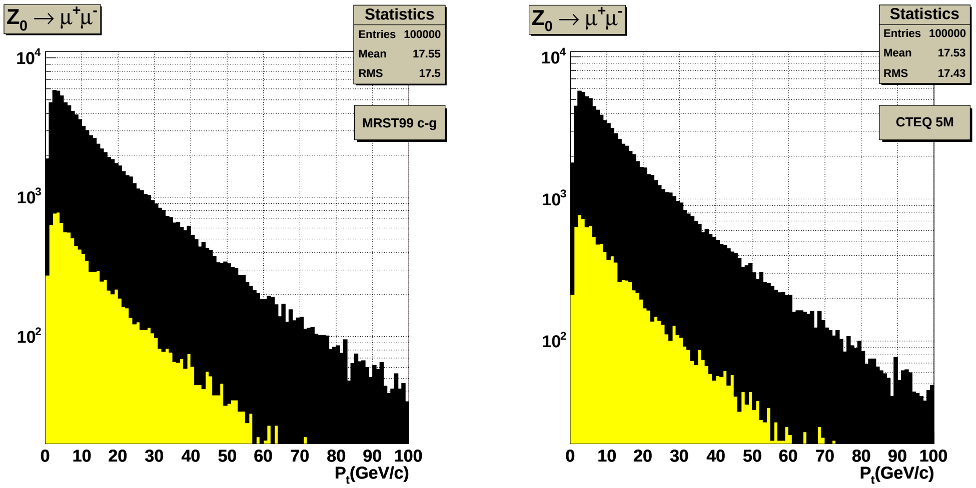

Figure 4.16: Transverse momentum spectrum of the generated (black) and selected (yellow) Z^0 boson.

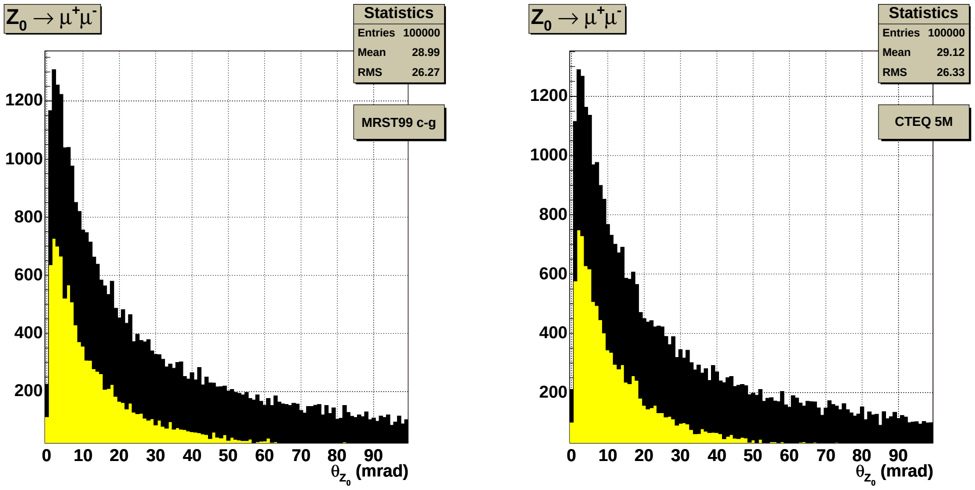

Figure 4.17: Polar angle distributions (bottom) of the generated (black) and selected (yellow) Z^0 boson.

Note that only Z^0 with a polar angle lower than ∼80 mrad decay into two muons both in the LHCb acceptance. This represents a major difference respect to the 4π experiments, which predominantly collect particles at high angles.

In Figure 4.18 the rapidity distribution is shown, again for all the Z^0 in 4π and for the Z^0 decaying in two muons in the LHCb acceptance.

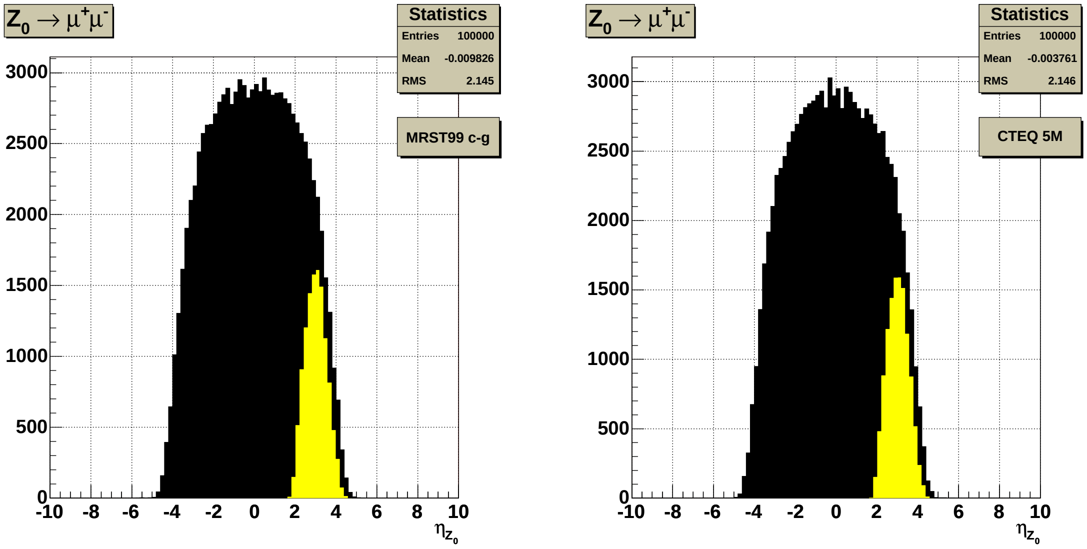

Figure 4.18: Rapidity distributions of the generated (black) and selected (yellow) Z^0 boson. Distributions on the left have been obtained using the MRST99(c-g) PDF set, while distributions on the right have been obtained using the CTEQ 5M PDF set.

From this figure we see that the LHCb rapidity acceptance is $2 \lesssim \eta \lesssim 5$. Note the cuts at very high rapidity ($\eta > 5$) indicates that muons escape from the detector acceptance as they enter the hole left for the beam-pipe, which has a coverage of about 20 mrad in x plane and 15 mrad in y plane.

Finally, the fractional momentum distributions of the downstream parton (x_1) and upstream parton (x_2) are shown in Figure 4.19 for the MRST (c-g) and CTEQ (5M) PDF sets. From these figure we can see again that the parton coming downstream the detector carries almost the whole amount of momentum, while the parton coming upstream the detector is essentially at the rest.

From all the figures shown we can deduce that, from the point of view of the event distributions, there is no evidence of an effect due to the particular choice of the PDF set. In the next paragraph, the same study with a NLO event generator will be discussed.

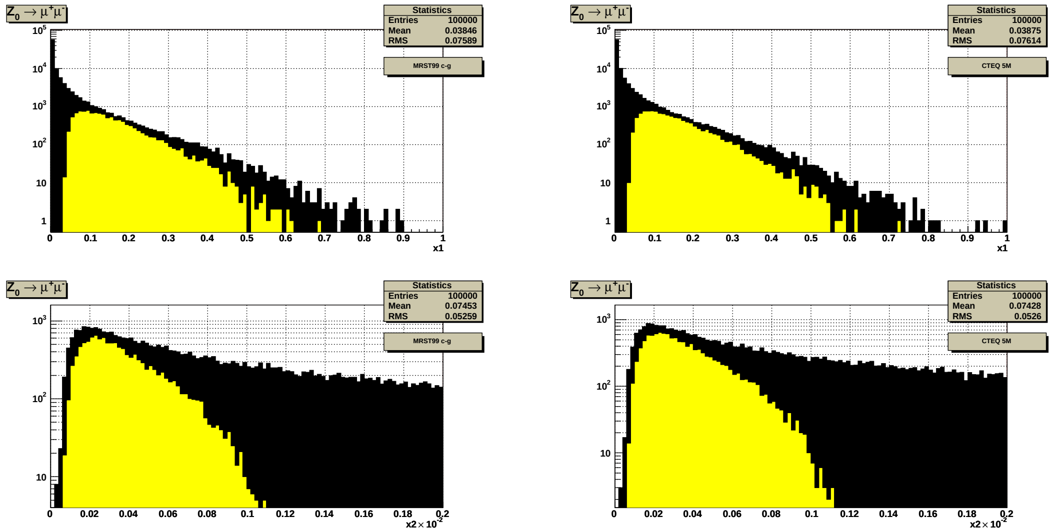

Figure 4.19: **(Left)** Fractional momentum distributions of the downstream parton (top) and upstream parton (bottom) in 4π (black) and in the LHCb acceptance (yellow) with the MRST99(c-g) PDF set. **(Right)** As the left plots, but with the CTEQ(5M) PDF set as input.

4.4.2 MC@NLO event generator

The MC@NLO package [67] is a practical implementation of the HERWIG event generator [68] which allows to incorporate NLO QCD matrix elements consistently into a parton shower framework. In contrast with the PYTHIA simulation, all the next to leading order processes (self-energy contribution included) described in §4.2 have been included in the simulation of the Z^0 production, so that in this case cross sections are intended to be at the NLO. As in the case of the PYTHIA simulation, the Z^0/γ^* interference structure has been not considered, just including the Z^0 matrix elements, so that only *on mass-shell* Z^0 have been generated and forced to decay into $\mu^+\mu^-$.

100k Z^0 events have been generated using the MRST99(c-g) PDF set and 100k events using the CTEQ 5M PDF set. In Figure 4.20 the Z^0 momentum spectrum is shown for both the parton distribution functions: the dark distributions represents the momentum spectrum of all the Z^0 generated, while the yellow distribution represents the momentum spectrum of the Z^0 which decay in two muons in the LHCb acceptance. This figure shows how the Z^0 momentum distribution are not affected by the particular choice of the used parton distribution function at all.

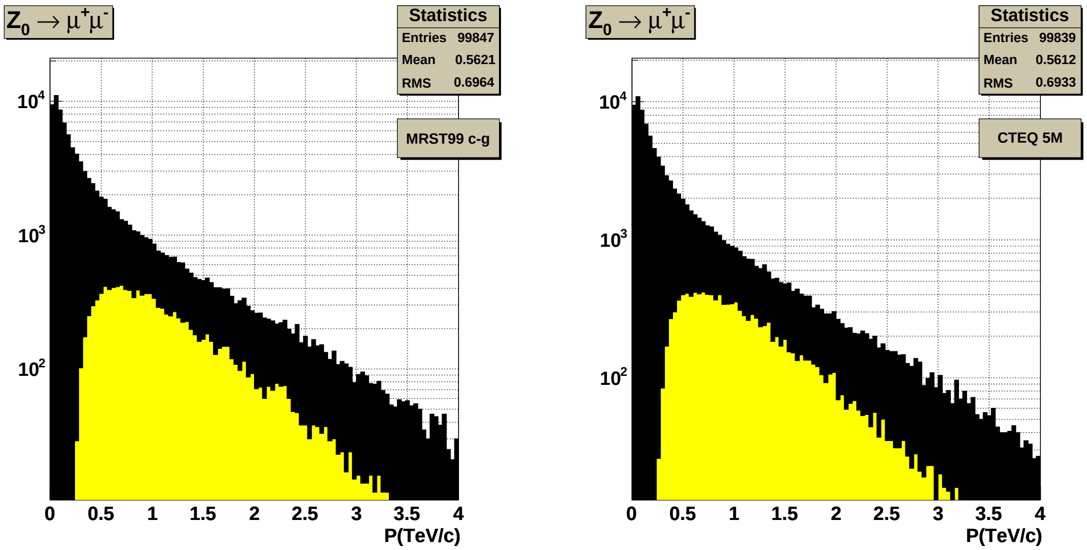

Figure 4.20: Momentum spectrum of the generated (black) and selected (yellow) Z^0 boson. Distributions on the left have been obtained using the MRST99(c-g) PDF set, while distributions on the right have been obtained using the CTEQ 5M PDF set.

Also the transverse momentum spectrum (Figure 4.21) and the polar angle θ distribution (Figure 4.22) are not affected by the particular choice of the PDF set.

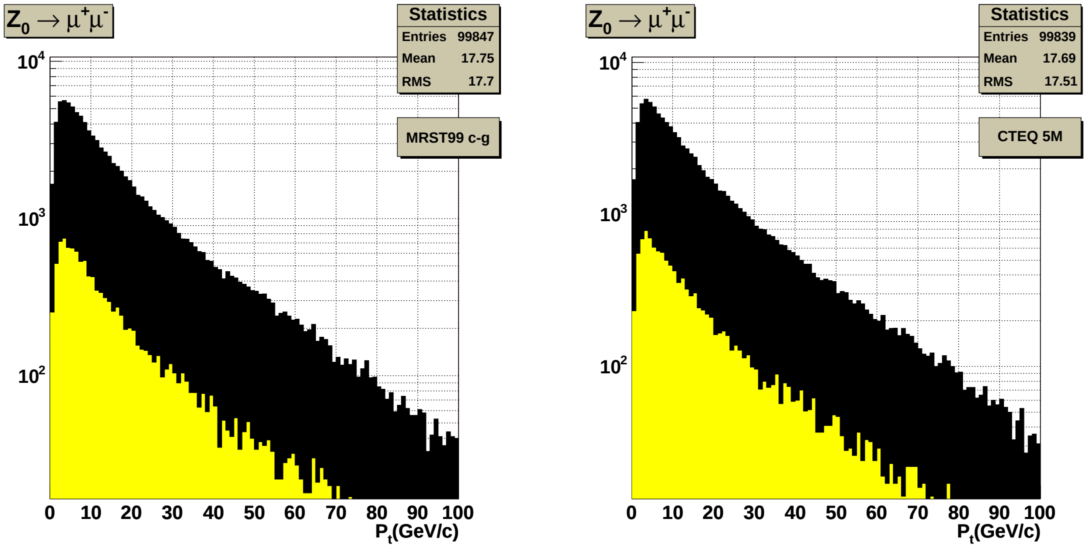

Figure 4.21: Transverse momentum spectrum of the generated (black) and selected (yellow) Z^0 boson. Distributions on the left have been obtained using the MRST99(c-g) PDF set, while distributions on the right have been obtained using the CTEQ 5M PDF set.

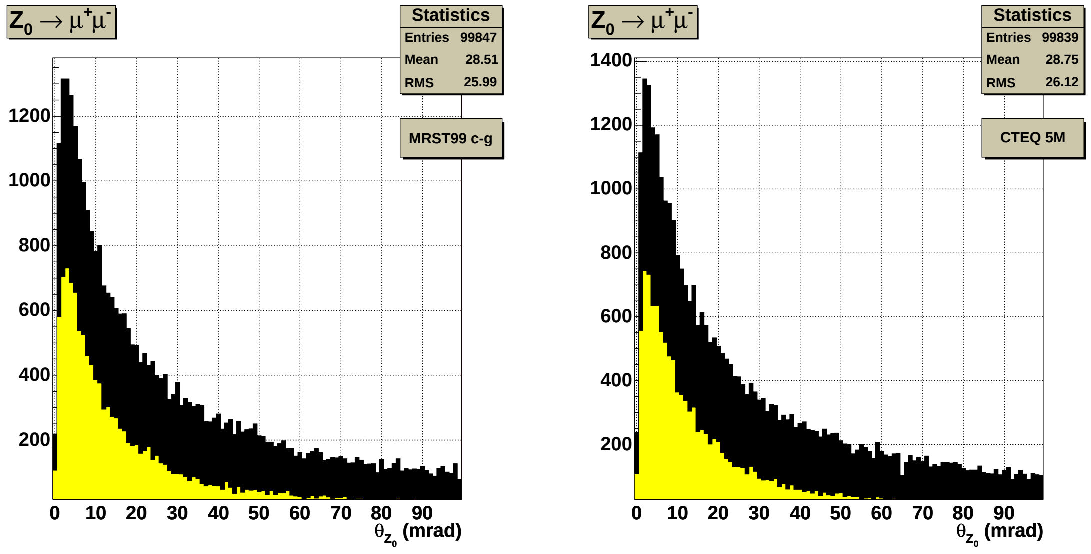

Figure 4.22: Polar angle distributions of the generated (black) and selected (yellow) Z^0 boson. Distributions on the left have been obtained using the MRST99(c-g) PDF set, while distributions on the right have been obtained using the CTEQ 5M PDF set.

In Figure 4.23 the rapidity distribution is shown, again for all the Z^0 in 4π and for the Z^0 decaying in two muons in the LHCb acceptance. No difference is highlighted.

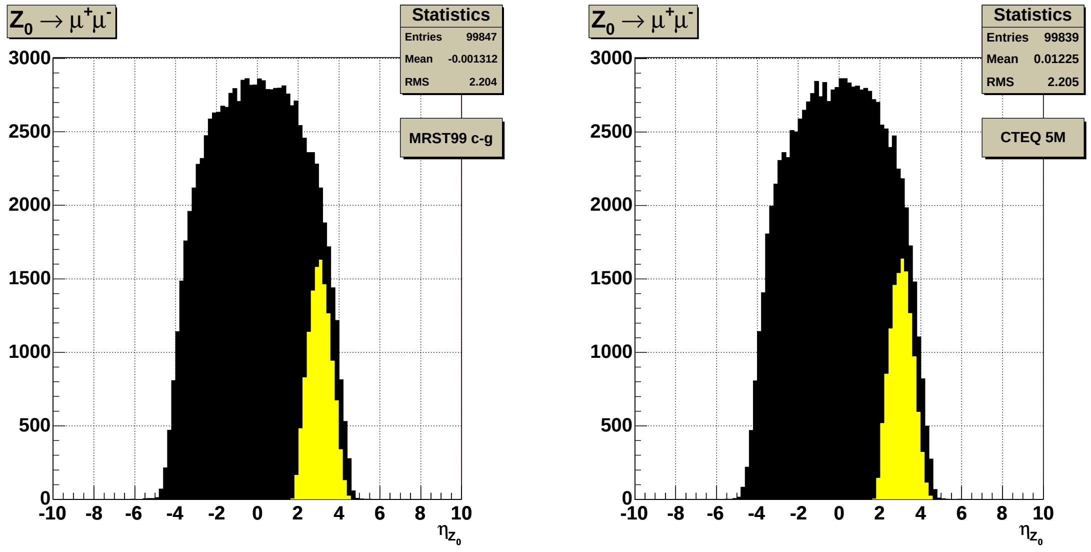

Figure 4.23: Rapidity distributions of the generated (black) and selected (yellow) Z^0 boson. Distributions on the left have been obtained using the MRST99(c-g) PDF set, while distributions on the right have been obtained using the CTEQ 5M PDF set.

Finally, the fractional momentum distributions of the downstream parton (x_1) and upstream parton (x_2) are shown in Figure 4.24 for the MRST (c-g) and CTEQ (5M) PDF sets.

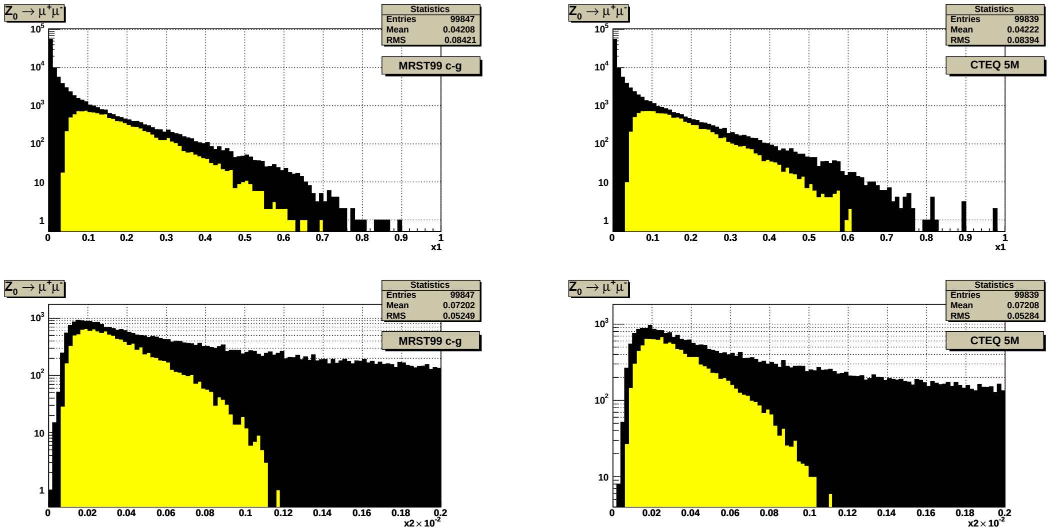

Figure 4.24: **(Left)** Fractional momentum distributions of the downstream parton (top) and upstream parton (bottom) in 4π (black) and in the LHCb acceptance (yellow) with the MRST99(c-g) PDF set. **(Right)** As the left plots, but with the CTEQ(5M) PDF set.

Figures 4.23 and 4.24 show again that the choice of the PDF set has no effect on the event distributions, as already seen in the simulation performed with PYTHIA.

4.5 Production cross section

In the previous section, we have seen that both the $pp \to Z^0 \to \mu^+\mu^-$ simulation studies carried out with the PYTHIA and MC@NLO event generators have shown how the event distributions are not sensitive to the different sets of parton distribution functions and also that the LHCb geometrical acceptance does not change this behaviour. Moreover, the two event generators used (PYTHIA and HERWIG+MC@NLO) produced very similar results; this is not true concerning the cross sections predictions and in the next paragraph a detailed study about the differences between this two generators and the effect of the LHCb acceptance will be presented.

As already seen in §4.2.1, the effect of the PDF set choice on the Z^0 cross section prediction is rather large (>10%). A precise measurement of this cross section would therefore allow to clearly distinguish between all the PDF sets developed by theorists, obtaining new important informations about the quark densities inside the proton at the LHC energy scale.

In this section, the effect of the geometrical LHCb acceptance on the cross section sensitivity to the PDFs will be described, in order to understand if the foward geometry of the detector will highlight this sensitivity or, on the contrary, will reduce it.

4.5.1 PYTHIA event generator

The cross section of the production process $pp \to Z^0 \to \mu^+\mu^-$ in the full solid angle has been computed for each of the seven different sets of proton structure functions as illustrated in Figure 4.25.

The result of the simulation is:

$$\sigma_{\rm LO} \cdot {\rm B}_{\mu\mu} = (1.69 \pm 0.09)\ {\rm nb}$$

where the uncertainty given corresponds to the ±5% band shown in the figure. All the predictions made with the MRST sets lie well within the ±5% band, while the predictions made with the new CTEQ PDF sets give much larger values.

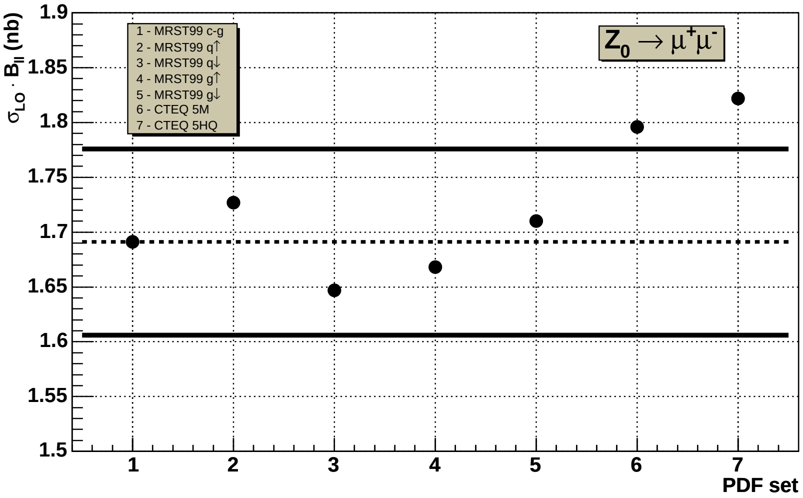

Figure 4.25: Cross section predictions for various PDF sets.

We want to understand what is the effect of the LHCb acceptance on these cross sections and in particular on the relative ratios between each set. In Figure 4.26, the cross section of each PDF set, relative to the reference MRST99(c-g) PDF set, is shown: the simulation corresponds to events where the Z^0 decays in two muons in the full solid angle (black points) or just inside the LHCb acceptance (blue points).

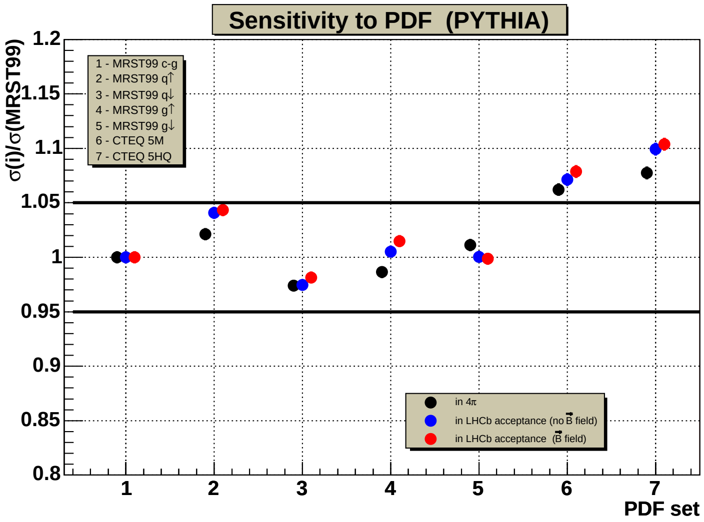

Figure 4.26: Cross section predictions dependance on different sets of structure functions relative to the reference MRST99(c-g) parametrization.

From this comparison, we conclude that the geometrical acceptance does not affect the cross section sensitivity to the parton distribution function sets. Moreover, in order to slightly improve the simulation, the LHCb magnetic field has been roughly simulated, as a uniform field at the center of the magnet (red points). Also in this case we can conclude that the effect is not relevant.

Thus, from the simulation performed with PYTHIA, we can conclude that the cross section is very sensitive to the choice of the parton distribution functions and that a precise measurement of the Z^0 production cross section allows to clearly identify the best theoretical parametrization of the proton structure.

4.5.2 MC@NLO event generator

Since, as previously seen, the $\mathcal{O}(\alpha_s)$ QCD corrections to the Z^0 production process are rather large, a next to leading order simulation could be useful to be more confident with the conclusions drawn in the previous paragraph. For this goal, the MC@NLO event generator has been used and the NLO cross section predictions have been computed for the same seven PDF sets used in PYTHIA. The result of the simulation is shown in Figure 4.27.

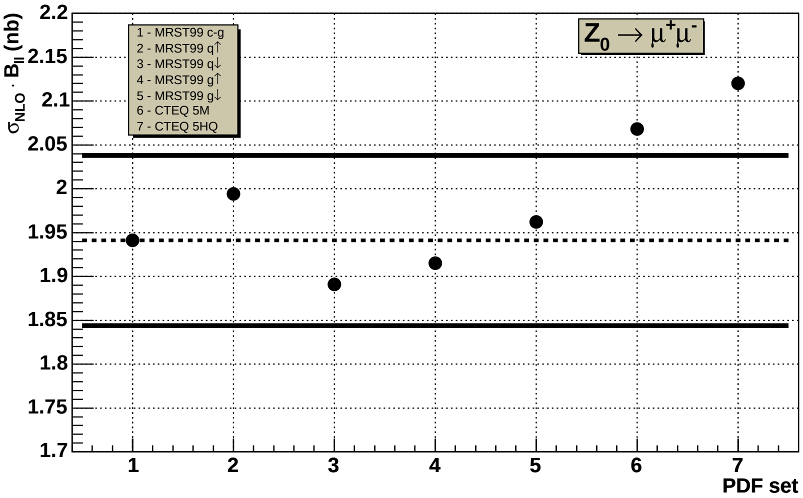

Figure 4.27: Cross section predictions for various PDF sets.

The cross section at the NLO level is:

$$\sigma_{\rm NLO} \cdot {\rm B}_{\mu\mu} = (1.94 \pm 0.1)\ {\rm nb}$$

and it is slighlty larger than the NNLO cross section prediction given in Eq. 4.3 as expected (see Figure 4.8).

In Figure 4.28, the cross section of each PDF set, relative to the reference MRST99(c-g) PDF set, is shown: also for the MC@NLO event generator, the simulation corresponds to events where the $\rm Z^0$ decays in two muons in the full solid angle (black points) or just inside the LHCb acceptance (blue points). Again, the LHCb magnetic field has been roughly simulated as a uniform field at the center of the magnet (red points).

The comparison shows as the geometrical LHCb acceptance does not affect the cross section sensitivity to the parton distribution function sets. From the simulation performed with MC@NLO+HERWIG therefore, we can again conclude that the cross section is very sensitive to the choice of the parton distribution functions and that a precise measurement of the $\rm Z^0$ production cross section allows to clearly identify the best theoretical parametrization of the proton structure.

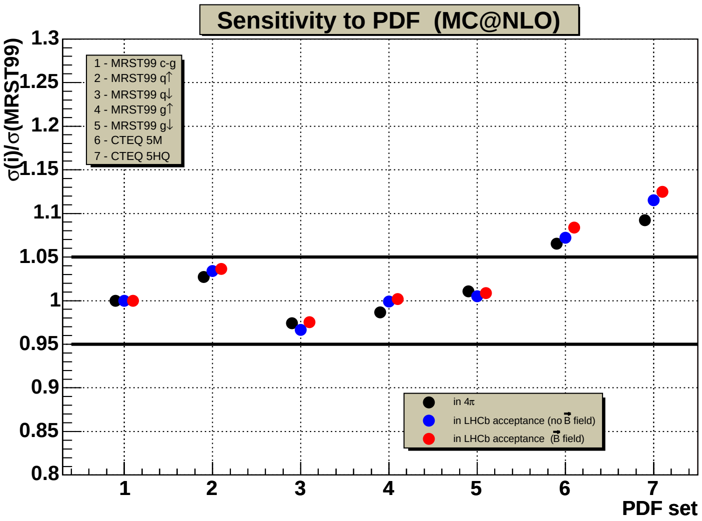

Figure 4.28: Cross section predictions dependance on different sets of structure functions relative to the reference MRST99(c-g) parametrization.

4.6 Absolute luminosity measurements

In §4.3 we have seen that a precise measurement of the Z^0 production cross section needs a corresponding knowledge with high accuracy of the machine luminosity.

In fact, once the absolute luminosity is known, the cross section can be calculated by the relation:

$$\sigma_{Z^0} = \frac{N_{Z\to\mu\mu}}{\mathcal{L} \times B_{\mu\mu} \times \epsilon_{tot}} \tag{4.5}$$

where $N_{Z\to\mu\mu}$ is the signal event yield observed, $B_{\mu\mu}$ is the branching ratio for the relevant channel, and ϵ_{tot} is the total efficiency of the detector. The annual signal yield S is computed as:

$$S = \mathcal{L}_{int} \times \sigma_{Z^0} \times B_{\mu\mu} \times \epsilon_{tot}$$

where $\mathcal{L}_{int}$ = 2 fb^{-1} is the annual integrated luminosity[2] and $\sigma_{Z^0} \times B_{\mu\mu} \approx$ 1.86 nb is the Z^0 production cross section[3] expected at 14 TeV (see Eq 4.3).

Thus, the number of events produced in one year of data taking in the full solid angle is $S \simeq 3.72 \times 10^6$ and once the total detector efficiency of about 8% [48] is included, we obtain $S \simeq 300$k events per year. As a comparison, the total number of $Z^0 \to \mu^+\mu^-$ collected by the Aleph experiment was about 200k in 5 years of data taking (1990-1995) at $\sqrt{s} \simeq$ 91 GeV [65].

Therefore, even if in the LHCb experiment most of the relevant quantities of the main physics program (e.g. branching ratios) will be determined just making

---

[2] assuming 10^7 s as one year of data taking and $\mathcal{L} = 2 \times 10^{32}$ cm^{-2} s^{-1}as nominal average luminosity

[3] including the branching ratio of the Z^0 decay in $\mu^+\mu^-$

use of the relative luminosity knowledge, simply achievable by counting the total event multiplicity, the absolute luminosity value is needed to compute the cross sections.

In general, there are two possibilities to determine the luminosity – either (i) to measure a pair of cross sections which are connected quadratically with each other, or (ii) to measure a cross section whose value is well known or which may be calculated with good accuracy. The well-known example of the first possibility is the measurement of the total σ_{tot} and differential forward elastic cross sections which are related by the optical theorem. This method requires dedicated detectors placed as close as possible to the beam, and is used at LHC by the TOTEM experiment [4].

Several types of processes stand out as examples of the second possibility to measure the luminosity. One is the exclusive lepton-pair production via photon-photon fusion $pp \to pp\ l^+l^-$ illustrated in Figure 4.29 for the elastic process.

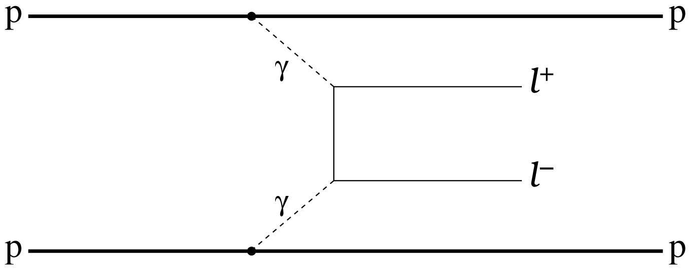

Figure 4.29: Two-photon elastic production of lepton pairs in pp collisions.

Luminometers for LHC based on such a process, measuring either $\mu^+\mu^-$ pairs [69] or e^+e^- pairs [70] have been proposed. Recently, a study focused on the two-photon production of $\mu^+\mu^-$ pairs at LHC as luminometer for the ATLAS experiment has been carried out [71]; this study also preliminarily examines the potentiality of the method for the LHCb experiment: although the low production cross section ($\sim$ 15 pb), since the theoretical uncertainties are very small, the luminosity could be measured with an error of 1-2 % in few months of data taking. This decay channel therefore can not be used as an online luminosity monitor but could be useful to calibrate alternative methods.

With the advent of precise microvertex detectors an alternative way of measuring directly the luminosity emerged. Recently, this alternative method and its possible use at the LHC experiments has been described [72]. The proposed method relies on beam-gas interactions for measuring the individual beam shapes and determining the beam overlap integral which enter the luminosity calculation.

The method proposed aims at measuring the time- and position-dependent density functions of the two counter-rotating beams from beam-gas collisions, assuming that the total number of protons in the bunches can be precisley measured by indipendent means. A dedicated running time of about one day should be sufficient to measure the luminosity with an accuracy of at least 1%.

Once fully known the LHC optics, a third method for the measurement of the absolute luminosity could be the transport of a luminosity measurement (e.g. TOTEM) to the LHCb interaction point. The feasibility of the method is currently under investigation.

Note that all the absolute luminosity measuring methods described above can be also be used to calibrate a relative luminosity measurement method.

4.7 Conclusions

In this chapter the analysis of the process $pp \to Z^0 \to \mu^+\mu^-$ has been reported. The aim of this analysis is to demonstrate the LHCb potentialities to study the parton distribution functions of the proton in a kinematic region not probed by the present experiments.

The theoretical cross section for this process has been recently calculated at NNLO; at the LHC energy of 14 TeV, the Z^0 production cross section is expected to be $\sigma_{\mathrm{Z}\to\mu\mu} \simeq$ 1.9 nb. The error associated with this prediction is however rather high ($>$10%), due to the large uncertainties on the knowledge of the parton distribution functions at this unexplored energy scale.

The forward geometry of LHCb is peculiar to select very high pseudorapidity Z^0 bosons, allowing to extract the proton structure functions $f(x, Q^2)$ at very low x ($\sim 10^{-4}$) and high Q^2 ($\sim 10^4$ GeV^2), therefore in a kinematic region not accessible to other experiments.

Thus, the effect of the LHCb geometrical acceptance on the cross section sensitivity to the PDF sets has been investigated by means of two event generators, PYTHIA, which simulates the process at the tree level, and MC@NLO, which instead also incorporates NLO matrix elements.

Both the simulations have shown that the cross section sensitivity to the PDF sets is not affected by the LHCb acceptance and therefore a precise measurements of the Z^0 production cross section will allow to clearly identify the best theoretical parametrization of the proton structure.

For this goal, a luminosity measurements with high accuracy is needed, and in the last paragraph three methods recently proposed as luminometers have been described.

Appendix A

NNLO corrections to the $\mathrm{q\bar{q}} \rightarrow \mathrm{Z}^0$ process

---

The first calculation of the second order α_s corrections was done for the qq process and it is shown in Figure A.1. Its result also hold for the $q\bar{q}$ scattering subprocess where a gluon is exchanged between the quark and the antiquark line.

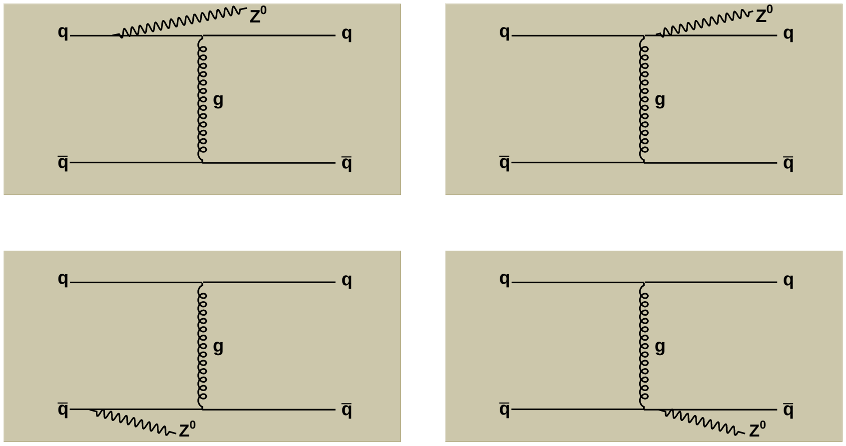

Figure A.1: Gluon exchange graphs contributing to the subprocess $q+\bar{q} \rightarrow \mathrm{Z}^0 + q+\bar{q}$ and $q(\bar{q})+q(\bar{q}) \rightarrow \mathrm{Z}^0 + q(\bar{q})+q(\bar{q})$ (not shown in the figure). It is needed also to add graphs contributing to the subprocess $q(\bar{q}) + q(\bar{q}) \rightarrow \mathrm{Z}^0 + q(\bar{q}) + q(\bar{q})$ with identical quarks in the initial and/or final state.

Thereafter the soft and virtual gluon contributions from the $q\bar{q}$ with two gluons or a quark pair in the final state were determined (Figure A.2).

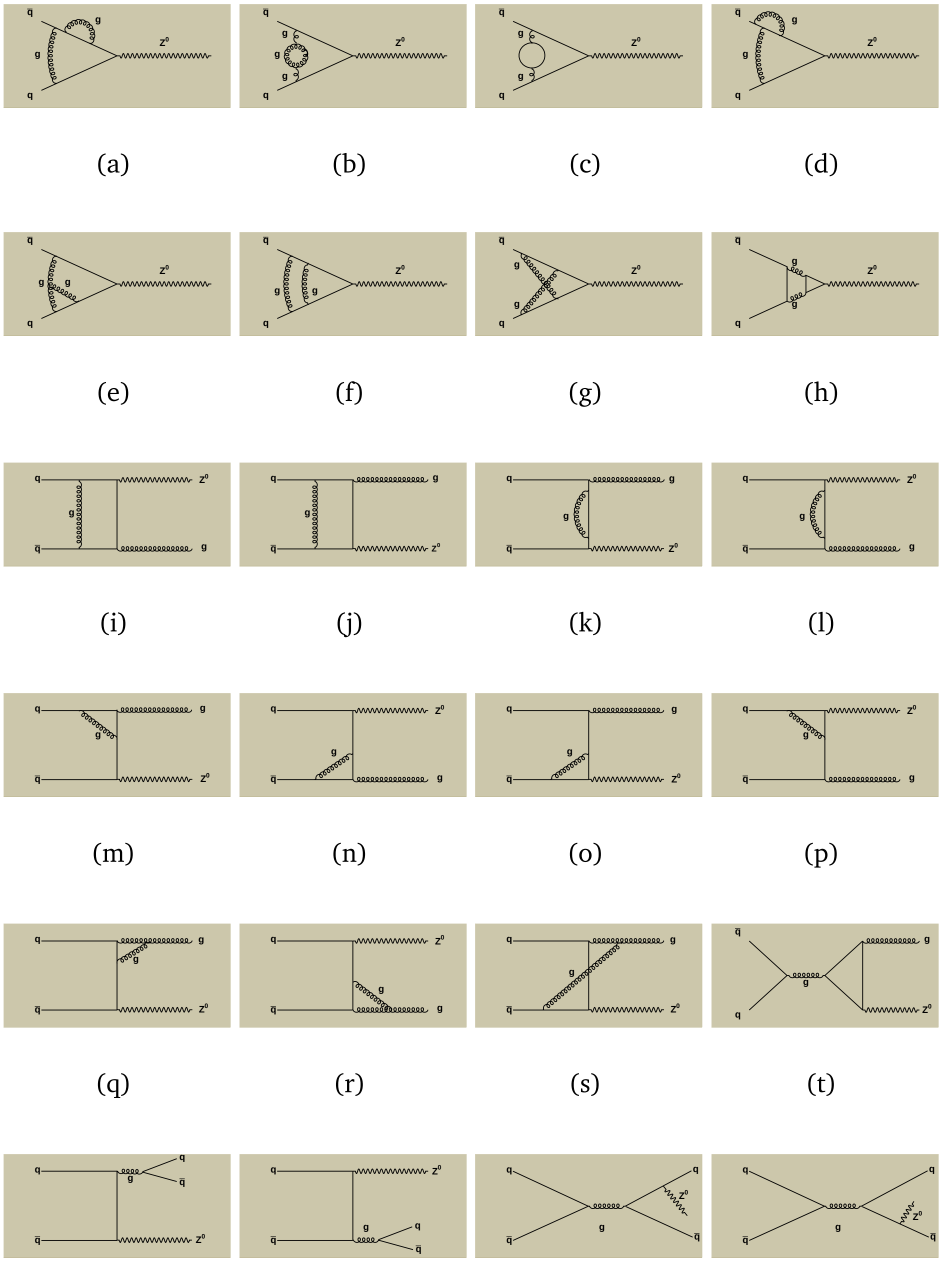

(a) (b) (c) (d)

(e) (f) (g) (h)

(i) (j) (k) (l)

(m) (n) (o) (p)

(q) (r) (s) (t)

(u) (v) (w) (x)

Figure A.2: Figures $a-h$: the two-loop correction to the process $q(\bar{q})+g \rightarrow$ Z^0 . Figures $i-t$: the one-loop correction to the process $q+\bar{q} \rightarrow$ Z^0 $+g$. The diagrams corresponding to the one-loop correction to the subprocess $q(\bar{q})+g \rightarrow$ Z^0 $+q(\bar{q})$ can be obtained via crossing. Figures $u-x$: annihilation graphs contributing to the subprocess $q+\bar{q} \rightarrow$ Z^0 $+q+\bar{q}$.

Finally, the most recent computations of the α_s^2 contributions to the $q + \bar{q} \rightarrow$ Z^0 concern the gg subprocess and the corresponding diagrams are shown in Figure A.3.

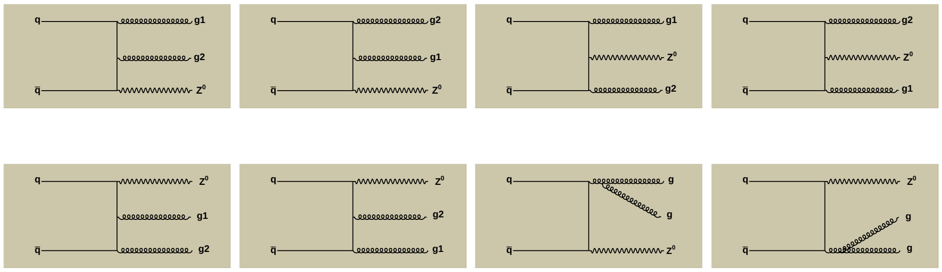

Figure A.3: Diagrams contributing to the subprocess $q + \bar{q} \rightarrow \mathrm{Z}^0 + g + g$. The graphs corresponding to the subprocess $q(\bar{q}) + g \rightarrow \mathrm{Z}^0 + q(\bar{q}) + g$ can be obtained from those presented in this figure via crossing. By crossing two pairs of lines one can obtained the diagrams corresponding to the subprocess $g + g \rightarrow \mathrm{Z}^0 + q + \bar{q}$.

Conclusions

The Muon System will play a fundamental role in the LHCb experiment. Muon triggering and offline muon identification are fundamental requirements of the LHCb experiment. Muons are present in the final states of many CP-sensitive B decays and also in some rare B decays which may reveal new physics beyond the Standard Model. Moreover, muons from semileptonic b decays provide a tag of the initial state flavour of accompanying neutral B mesons.
The construction of the Muon System, started in 2004, is expected to be complete at the beginning of 2007. The muon detector will be equipped with 1368 multiwire proportional chamber produced in six different sites; thus, a stringent procedure for the quality control test during and after the chambers construction has been adopted. In particular, the chambers performance uniformity is a crucial point in order to achieve a common working range. One of the most important goals of the LHCb experiment will be the asymmetries study and the detector geometry itself has been designed to this purpose. It is clear that the uniformity is therefore a binding characteristic of the whole detector and in particular of the Muon System because of the role it will must play.

The work of the first part of this thesis consists in the study of the multiwire proportional chambers with the cosmic rays test station we have designed and developed. First of all, the cosmic rays stand has been used to probe the tracking capability of the chambers with a dedicated study of the tracking with cosmics, carried out with two chamber types. The custom finding track algorithm, developed similarly to the experiment method, has proven to be reliable and in well agreement with what it is expected corrisponding to the tracking layers efficiency($\sim$80-90%). The tracks reconstruction has then been used to perform precise efficiency measurements, which have demonstrated that the MWPC produced for the Muon System will fulfil the trigger requirements($\epsilon >$99%).

The information collected with the cosmic rays station has also been used to measure the gas gain uniformity of the chambers. This method is alternative to the default test which instead is carried out by means of a radioactive source. The comparison of the two methods has proven that the method discussed here is reliable and does not require to comply with safety regulations (absence of radioactive source).

In the second part of the thesis the process $pp \to \mathrm{Z}^0 \to \mu^+\mu^-$ has been studied. The aim of this analysis is to demonstrate the LHCb potentialities to study the Parton Distribution Functions of the proton in a kinematic region not probed by the present experiments.

The theoretical cross section for this process has been recently calculated in perturbative QCD theory at the next-to-next leading order (NNLO); at the LHC energy of 14 TeV, the Z^0 production cross section is expected to be $\sigma_{\mathrm{Z}\to\mu\mu} \simeq 1.9$ nb, sufficiently high to detect a large number of Z^0 bosons also at LHCb, in spite of the limited angular acceptance and the optimization for the B-physics. The forward geometry of LHCb is peculiar to select very high rapidity Z^0 bosons, allowing to extract the parton structure functions $f(x, Q^2)$ at very low x ($\sim 10^{-4}$) and high Q^2 ($\sim 10^4$ GeV^2), in a kinematic region not accessible to other experiments.

In particular, the work has been focused on the effect of the LHCb geometrical acceptance on the cross section sensitivity to the various set of partons, simulating the process with two different event generator, PYTHIA, which simulates the process at the tree level, and MC@NLO (+HERWIG), which instead also incorporates NLO matrix elements. Both the simulations have shown that the cross section sensitivity to the PDF sets is not affected by the LHCb acceptance and therefore a precise measurements of the Z^0 production cross section will allow to clearly identify the best theoretical parametrization of the proton structure. For this goal, the absolute luminosity measurements with high accuracy are needed, and three different methods recently proposed as luminometers have been briefly discussed.

Bibliography

---

[1] P. Lefèvre and T. Pettersson, *The Large Hadron Collider: conceptual design*, CERN/AC/95/05/LHC, 1995.

[2] ATLAS Collaboration, W.W. Armstrong et al., *ATLAS : Technical Proposal for a General-Purpose pp Experiment at the Large Hadron Collider at CERN*, CERN/LHCC/94-43, 1994.

[3] CMS Collaboration, *Technical Proposal*, CERN/LHCC/94-38, 1994.

[4] TOTEM Collaboration, W. Kienzle et al., *Technical Proposal*, CERN/LHCC/99-7, 1999.

[5] ALICE Collaboration, N. Ahmad et al., *A Large Ion Collider Experiment - Technical Proposal*, CERN/LHCC/95-71, 1995.

[6] LHCb Collaboration, *Technical Proposal*, CERN-LHCC/98-4, 1998.

[7] P. Nason et al., *Bottom production. In Proceedings of the 1999 Workshop on Standard Model Physics at the LHC*, volume CERN 2000-004, 1999.

[8] T. Nakada and O. Schneider, LHCb Trigger. In *Proceedings of the 4th International Workshop on B Physics and CP Violation*, February 19-23, 001 Ise-Shima (Japan).

[9] LHCb Collaboration, *LHCb Reoptimized Detector Design and Performance - Technical Design Report*, CERN/LHCC/2003-030, 2003.

[10] LHCb Collaboration, *LHCb VELO Technical Design Report*, CERN/LHCC/2001-0011.

[11] LHCb Collaboration, *LHCb RICH Technical Design Report*, CERN/LHCC/2000-0037.

[12] LHCb Collaboration, *LHCb Magnet Technical Design Report*, CERN/LHCC/2000-007.

[13] LHCb Collaboration, *LHCb Inner Tracker Technical Design Report*, CERN/LHCC/2002-029.

[14] LHCb Collaboration, *LHCb Outer Tracker Technical Design Report*, CERN/LHCC/2001-026.

[15] LHCb Collaboration, *LHCb Calorimeters Technical Design Report*, CERN/LHCC/2000-036.

[16] LHCb Collaboration, *LHCb Muon System Technical Design Report*, CERN/LHCC/2001-010.

[17] LHCb Collaboration, *LHCb Trigger System Technical Design Report*, CERN/LHCC/2003-031.

[18] GAUDI Project, `http://proj-gaudi.web.cern.ch/proj-gaudi/welcome.html`

[19] LHCb Collaboration, *GAUSS - The LHCb Simulation Program*, `http://lhcb-comp.web.cern.ch/lhcb-comp/Simulation/default.htm`.

[20] S. Agostinelli et al., *GEANT4 - a simulation toolkit*, Nucl. Instr. and Meth. in Phys. Res. A506 (2003) 250.

[21] T. Sjöstrand, *High-energy physics event generation with PYTHIA 5.7 and JETSET 7.4*, Comput. Phys. Commun., 82:74-90, 1994

[22] *QQ – The CLEO Event Generator*, `http://www.lns.cornell.edu/public/CLEO/soft/QQ`.

[23] LHCb Collaboration, *BOOLE - The LHCb Digitization Program*, `http://lhcb-comp.web.cern.ch/lhcb-comp/Digitization`.

[24] LHCb Collaboration, *BRUNEL - The LHCb Reconstruction Program*, `http://lhcb-comp.web.cern.ch/lhcb-comp/Reconstruction`.

[25] LHCb Collaboration, *DAVINCI – The LHCb Analysys Program*, `http://lhcb-comp.web.cern.ch/lhcb-comp/Analysys`.

[26] Babar Collaboration, B. Aubert et al., *Measurement of the CP-violating asymmetry amplitude sin2β*, Phys. Rev. Lett. 89 (2002) 201802.

[27] Belle Collaboration, K. Abe et al., *Measurement of CP-violation parameter sin(2ϕ_1) with 152 million B anti-B pairs*, Phys. Rev. D66 (2002) 071102.

[28] M. Battaglia et al., *The CKM matrix and the Unitarity Triangle*, hep-ph/0304132.

[29] C. Zeitnitz and T.A. Gabriel, *The Geant-Calor interface User's Guide (1999)*, `http://www.staff.uni-mainz.de/zeitnitz/Gcalor/gcalor.html`

[30] I. Azhgirey, I. Kurochkin and V. Talanov, *Development of MARS Code Package for Radiation Problems Solution of Electro-Nuclear Installation Design*, in: Proceedings of XV Conference on Charged Particles Accelerators, Protvino, October 22-24 (1996).

[31] N. Saguidova et al., *GCALOR Studies of Backgrond in the LHCb Muon chambers*, LHCb 1998–059 Expt.

[32] A. Tsaregorodtsev, *Muon System parameterised background - algorithm and implementation*, LHCb Note 2000–011 Muon.

[33] P. Colrain, *Upgrade of the Muon System background parameterisation*, LHCb 2001–029 Muon.

[34] G. Martellotti et al., *Montecarlo samples and efficiency definitions for the muon system optimization*, LHCb 2001-007 Muon.

[35] F. Sauli, *GEM: A new concept for electron amplification in gas detectors*, Nucl. Instr. and Meth. in Phys. Res. A386 (1997) 531.

[36] LHCb Collaboration, *Second Addendum to the LHCb Muon System Technical Design Report*, CERN/LHCC/2005-012.

[37] A. Balla et al., *The muon chamber mapping for the IB system*, LHCb 2004-004 Muon.

[38] W. Riegler, *Detector Physics and Performance Simulations of the MWPCs for the LHCb Muon System*, LHCb 2000-060 Muon.

[39] B. Schmidt et al., *Results from a 2 mm pitch MWPC prototype for the LHCb Muon System*, LHCb 2003-002 Muon.

[40] M. Anelli et al., *Extensive aging test of two prototypes of four-gap MWPC for the LHCb Muon System*, LHCb 2004-029 Muon.

[41] J. Christiansen, *Requirements for the L0 front-end electronics*, LHCb 1999-029 Trigger.

[42] D. Moraes et al., *The CARIOCA Front End Chip for the LHCb muon chambers*, LHCb 2003-009 Muon.

[43] CARDIAC technical documentation:
`http://lhcb-muon.web.cern.ch/lhcb-muon/electronics/cardiac.html`

[44] G. Chiodi et al., *ASDQ++ Front-end board for the MWPC readout of the LHCb Muon System*, LHCb 2002-014 Muon.

[45] ELMB technical documentation:
`http://atlas.web.cern.ch/Atlas/GROUPS/DAQTRIG/DCS/ELMB/ELMBhome.html`

[46] R. Brun et al., *ROOT - An Object-Oriented Data Analysis Framework*,
`http://root.cern.ch`

[47] Rubbia C. et al., *Proceedings of the International neutrino conference*, Aachen, 1976, Vieweg p. 683.

[48] D. Domenici, *Detection of muons in the LHCb experiment: the aging of RPC detectors and the study of* $Z^0 \to \mu^+\mu^-$, University of Rome “Tor Vergata”, PhD thesis, 2003.

[49] S.D. Drell and T.M. Yan, *Massive lepton pair production in hadron-hadron collisions at high-energies*, Phys. Rev. Lett. 25 (1970) 316.

[50] J.H. Christenson et al., *Observation of massive muon pairs in hadron collisions*, Phys. Rev. Lett. 25 (1970) 1523.

[51] P.D.B. Collins & A.D. Martin, *Hadron Interactions*, ADAM HILGER LTD, BRISTOL.

[52] H. Plothow-Besch, *PDFLIB: Proton, Pion and Photon Parton Density Functions, Parton Density Functions of the Nucleus and α_s Calculations*, User’s Manual - Version 8.04, W5051 PDFLIB, 2000.04.17, CERN_PPE.

[53] P.N. Harriman et al., *Parton distributions extracted from data on deep-inelastic lepton scattering, prompt photon production, and the Drell-Yan process*, Phys. Rev. D42 (1990) 798.

[54] A.D. Martin et al., *Parton distributions of the proton*, Phys. Rev. D50 (1994) 6734.

[55] H.L. Lai et al., *Global QCD Analysis of Parton Structure of the Nucleon: CTEQ5 Parton Distributions*, Eur. Phys. J. C12 (2000) 375.

[56] R. Hamberg et al., *A complete calculation of the order α_s^2 correction to the Drell-Yan K-factor*, Nuclear Physics B359 (1991) 343.

[57] U. Baur et al., *QED Radiative Corrections to Z Boson Production and the Forward Backward Asymmetry at Hadron Colliders*, Phys. Rev. D57 (1998) 199.

[58] D. Acosta et al., *First Measurements of Inclusive W and Z Cross Sections from Run II of the Fermilab Tevatron Collider*, Phys. Rev. Lett. 94 (2005) 091803.

[59] R. Rijken and W. van Neerven, *Order α_s^2 contributions to the Drell-Yan cross section at fixed target energies*, Phys. Rev. D51 (1995) 44.

[60] W. van Neerven and E. Zijstra, *The $\mathcal{O}\left(\alpha_s^2\right)$ corrected Drell-Yan K-factor in the DIS and $\overline{MS}$ schemes*, Nuclear Physics B382 (1992) 11.

[61] S. Eidelman et al., *Review of Particle Physics*, Phys. Lett. B 592 (2004) 1. `http://pdg.lbl.gov`

[62] V.A. Khoze et al., *Luminosity measurements processes at the LHC*, Eur. Phys. J. C19 (2001) 313.

[63] A.D. Martin et al., *Estimating the effect of NNLO contributions on global parton analyses*, Eur. Phys. J. C18 (2000) 117.

[64] A.D. Martin et al., *Parton distributions and the LHC: W and Z production*, Eur. Phys. J. C14 (2000) 133.

[65] The Aleph Collaboration, *Measurement of the Z Resonance Parameters at LEP*, Eur. Phys. J. C14 (2000) 1.

[66] T. Sjöstrand et al., Computer Physics Commun. 135 (2001) 238.

[67] S. Frixione and B.R. Webber, *Matching NLO QCD computations and parton shower simulations*, JHEP 0206 (2002) 029;
S. Frixione, P. Nason and B.R. Webber, *Matching NLO QCD and parton showers in heavy flavour production*, JHEP 0308 (2003) 007.

[68] G. Corcella et al., *HERWIG 6: an event geneator for Hadron Emission Reactions with Interfering Gluons*, JHEP 0101 (2001) 010.

[69] A. Maslennikov, *Photon Physics in Novosibirsk*, Workshop on Photon Interactions and Photon Structure, Lund (1998) 347.

[70] K. Piotrzkowski, ATLAS Physics Note ATL-PHYS-96-077 (1996).

[71] A. G. Shamov and V. I. Telnov, *Precision luminosity measurement at LHC using two-photon production of $\mu^+\mu^-$ pairs*, Nucl. Instr. and Meth. in Phys. Res. A494 (2002) 51.

[72] M. Ferro-Luzzi *Proposal for an absolute luminosity determination in colliding beam experiments using vertex detection of beam-gas interactions*, Nucl. Instr. and Meth. in Phys. Res. A553 (2005) 388.